Optical tweezers combined with interference reflection microscopy for quantitative trapping and 3D imaging

Dissertation
der Mathematisch-Naturwissenschaftlichen Fakultät
der Eberhard Karls Universität Tübingen
zur Erlangung des Grades eines
Doktors der Naturwissenschaften
(Dr. rer. nat.)

vorgelegt von
Steve Simmert
aus Erfurt

Tübingen
2018

Gedruckt mit Genehmigung der Mathematisch-Naturwissenschaftlichen Fakultät der Eberhard Karls Universität Tübingen.

Tag der mündlichen Prüfung	11.07.2018
Dekan	Prof. Dr. Wolfgang Rosenstiel
1. Berichterstatter:	Prof. Dr. Erik Schäffer
2. Berichterstatter:	Prof. Dr. Tilman Schäffer

Für Miriam, Freya und Tammo.

Abstract

Optical tweezers are an indispensable tool in biophysical single-molecule studies. They provide the ability to mechanically probe the characteristics of biological processes, such as active transport of cargo by molecular motors. To this end, functionalized (sub)micron-sized dielectric particles are held in a tightly focused laser trap while external forces lead to displacements of the particle from the trap center. The measurement and calibration of these displacements yield insights into the mechanical properties of the molecule of interest.

The study of molecular motors, such as kinesins, is carried out in *in vitro* surface-based experimental assays. The experimental needs for such assays are challenging. The instrument must be stabilized, *i.e.* decoupled form external noise, and drift must be minimized, and it needs to be combined with state of the art microscopy techniques to visualize the sample. These are, on the one hand, single-molecule fluorescence detection and, on the other hand, robust label-free imaging of diffraction limited specimen. The latter is commonly realized by differential interference contrast (DIC) microscopy, which is an expensive and rather complicated technique that also restricts the design of the optical tweezers and, therefore, reduces the experimental possibilities.

Optical tweezers experiments, moreover, rely on precise and reliable calibration. Despite its importance, calibration is, at times, carried out with obsolete methods or based on vague assumptions. Especially, in the vicinity of the sample surface, where hydrodynamic effects can have a significant influence, such assumptions fail largely. Here, height-dependent active power spectral density analysis of the Brownian motion of the trapped particle can ameliorate these inaccuracies, but—compared to other methods—is rather cumbersome, time-consuming and easy-to-use solutions are lacking.

In this work I designed and assembled an optical tweezers setup combined with total internal reflection fluorescence (TIRF) microscopy. Furthermore, I succeeded to reduce design restrictions of the optical tweezers by combining it with interference reflection microscopy, which is a simple, cost-efficient and robust contrast technique that can visualize diffraction limited specimen in three dimensions, such as microtubules. Moreover, I was able to use this technique to determine the three-dimensional profile of an upward bent microtubule which I used to simultaneously calibrate the evanescent field depth of the TIRF microscope. In addition, I programmed a free and open-source optical tweezers calibration software, PyOTC, that provides the means for height-dependent active power spectral density analysis.

My work will possibly influence the design of optical tweezers instruments for surface-based experiments. LED-based IRM could further improve or complement label-free detection techniques such as interferometric scattering microscopy. The free and open-source calibration software package could help to precisely calibrate optical tweezers data. Moreover, because the source is available to anybody, calibration and therefore the analysis of optical tweezers data will be more transparent to the scientific community.

Zusammenfassung

Optische Pinzetten sind ein unverzichtbares Werkzeug in biophysikalischen Einzelmolekülstudien. Sie bieten die Möglichkeit die Eigenschaften biologischer Prozesse, wie zum Beispiel den aktiven Transport biologischer Lasten durch molekulare Motoren, mechanisch zu untersuchen. Zu diesem Zweck werden funktionalisierte (sub-)mikrometer große, dielektrische Kugeln in einem stark fokussierten Laser gehalten während externe Kräfte zu Verschiebungen der Kugel relativ zum Laserfokus führen. Die Messung und Kalibrierung dieser Verschiebungen liefert Einblicke in die mechanischen Eigenschaften des untersuchten Moleküls.

Die Untersuchung von molekularen Motoren, wie zum Beispiel Kinesinen, wird in *in vitro* oberflächenbasierten Experimenten durchgeführt. Experimentell sind solche Untersuchungen eine große Herausforderung. Das Gerät muss stabilisiert sein, d.h. es muss von externem Rauschen entkoppelt sein und Drift muss minimiert sein. Um die Probe zu visualisieren muss das Gerät außerdem mit modernen Methoden der Mikroskopie kombiniert sein um, zum einen, die Detektion der Fluoreszenz einzelner Moleküle und, zum anderen, die fluoreszenzfreie Abbildung diffraktionslimitierter Proben zu ermöglichen. Letzteres wird üblicherweise durch differentielle Interferenzkontrastmikroskopie (DIC) realisiert. DIC ist jedoch eine teure und eher komplizierte Technik ist die das Design der optischen Pinzette einschränkt und daher die experimentellen Möglichkeiten begrenzt.

Experimente mit optischen Pinzetten beruhen außerdem auf einer präzisen und zuverlässigen Kalibrierung. Trotz ihrer Bedeutung wird die Kalibrierung manchmal mit veralteten Methoden oder auf vagen Annahmen durchgeführt. Insbesondere in der Nähe der Probenkammeroberfläche, bei der hydrodynamische Effekte einen signifikanten Einfluss auf die Messergebnisse haben können, versagen solche Annahmen weitgehend. Diese Ungenauigkeiten können durch eine höhenabhängige Analyse der aktiv angetriebenen spektralen Leistungsdichte eingefangener Kugeln verringert werden. Verglichen mit anderen Verfahren ist die Umsetzung dieser Methode jedoch eher mühsam und zeitintensiv und es fehlt an einfach zu bedienenden Software-Lösungen.

In dieser Arbeit entwarf und montierte ich eine optische Pinzette die ich mit Totalreflexions-Fluoreszenzmikroskopie (TIRF) kombinierte. Darüber hinaus gelang es mir, die Designrestriktionen der optischen Pinzette zu reduzieren, indem ich die optische Pinzette mit LED-basierter Interferenzreflektionsmikroskopie (IRM) kombinierte. IRM ist eine kostengünstige und robuste Kontrastmethode, die auflösungsbegrenzte Proben, wie zum Beispiel Mikrotubuli, dreidimensional visualisieren kann. Weiterhin konnte ich mit dieser Technik das dreidimensionale Profil eines nach oben gebogenen Mikrotubulus bestimmen. Mit diesem Profil konnte ich gleichzeitig die Tiefe des evaneszenten Feldes des TIRF-Mikroskops kalibrieren. Darüber hinaus programmierte ich eine freie und quelloffene-Software für optische Pinzetten, PyOTC, welche Methoden für die höhenabhängige Analyse der aktiv angetriebenen spektralen Leistungsdichte eingefangener Kugeln bereitstellt.

Meine Arbeit wird möglicherweise das Design optischer Pinzetten für oberflächenbasierte Experimente beeinflussen. LED-basiertes IRM könnte fluoreszenz-freie Detektionstechniken

wie die interferometrische Streumikroskopie (iScat) weiter verbessern oder ergänzen. Die freie und quelloffene-Software kann helfen, die Daten optischer Pinzetten präzise zu kalibrieren. Da die Software für jeden verfügbar ist, wird die Kalibrierung und damit die Analyse von optischen Pinzettendaten für die wissenschaftliche Gemeinschaft transparenter.

Contents

Overview

This thesis consists of five major parts. After this overview, in Part I, the history of optical trapping is briefly outlined (Chapter 1) and the physics of this phenomenon is described (Chapter 2). Part II focuses on the design and control of the instrument. The location and the choice of the environment for the optical tweezers setup is reasoned in Chapter 3. Chapter 4 describes the optical design of the combined setup and in Chapter 5 the control of the hardware and temperature is presented. In Part III the characterization of the performance of optical tweezers is discussed. In the introductory Chapter 6, the sources of noise that might compromise optical tweezers measurements are described and the mathematical tools needed to identify this noise and characterize the achievable performance of such instruments are given. In Chapter 7, the performance, such as the long-term stability and achievable resolution, of the optical tweezers setup is presented. Part IV focuses on the calibration of optical tweezers. In Chapter 8, after a summary of different optical tweezers calibration methods is given, the theory of height-dependent active power spectral density analysis is described. This theory is the base for the Python Optical Tweezers Calibration (PyOTC) package. Its features and usage is described in Chapter 9. Part V focuses on LED-based interference reflection microscopy. After the introductory Chapter 11 that puts the technique into perspective and a materials and methods chapter (Chapter 12), results are presented that show how the contrast of IRM could be optimized (Section 13.2) and how the interference pattern could be used quantitatively to calibrate the evanescent field of the TIRF microscope (Section 13.3). In Chapter 15 this thesis is summarized and an outlook is given.

Part I.

Introduction to optical tweezers

1. History of optical trapping

Light carries momentum and, thus, can exert a force when interacting with matter. This fact is a logical consequence of what was once proposed by Johannes Kepler [1]. Kepler proposed that comet tails point away from the sun because of the sun's radiation pressure. J. C. Maxwell and A. Bartoli showed, theoretically, that radiation pressure can be explained by the electromagnetic theory of light [2, 3]. The experimental proof of radiation pressure was first done by Pyotr N. Lebedev utilizing an experimental set-up similar to Crook's light mill, but accounting for convective and other disturbances. About the magnitude of the force he wrote:

> "[...] Diese Druckkräfte sind sehr klein. Sowohl Maxwell als auch Bartoli haben berechnet, dass die Sonnenstrahlung, wenn sie normal auf 1 qm fällt, einen Druck ausübt, welcher für eine absolut schwarze Oberfläche 0,4 mg und für einen ebenen Spiegel 0,8 mg beträgt."[1] — P. N. Lebedev, Annalen der Physik 1901 [4]

Lebedev used the focused light of an arc lamp shone on platinum foil to measure the radiation pressure. He was able to rule out the disturbing effects, caused by heating through the light itself, namely the radiometric forces, which can be orders of magnitude higher than the radiative force. After the invention of lasers in the second half of the 20$^{\text{th}}$ century, the study of radiation pressure became easier through the enormous accessible irradiative power of these devices. Arthur Ashkin, first, observed the acceleration of micron-sized particles by radiation pressure of visible laser light [6]. Ashkin and his colleagues were later able to also demonstrate that the very particles, with sizes between 25 nm and 10 µm, could also be trapped stably in a so-called single-beam gradient force radiation pressure particle trap [7], which is nowadays known as optical tweezers. The principle has since found various applications, ranging from particle sorting [8] over microfabrication [9, 10] and manipulation of biological samples [11, 12].

Apart from being able to non-invasively manipulate samples, it became also feasible to measure the change of light momentum and infer the acting force or measure the displacement of a trapped particle [13]. The so-called analytical optical tweezers had a tremendous impact in studying molecules. Moffitt *et al.* described it as:

[1] The radiation pressure, *i.e.* the force, F, acting on an area, A, is given by [5]

$$p_{\text{rad}} = \frac{F}{A} = \frac{I_0 \sigma}{Ac},$$

where c is the speed of light, I_0 is the irradiance and σ is the extinction cross section, which, for a black body (*i.e.* fully absorbing), as well as for a fully reflecting surface, is equal to the irradiated area. The irradiance on earth by sunlight is given by the solar constant. Thus, $I_0 = E_\odot = 1367\,\text{Wm}^{-2}$. A reflecting surface experiences twice the amount of pressure, because the momentum changes to the opposite direction, *i.e.* $\Delta p_{\text{mirror}} = (-p) - p = -2p$, instead of vanishing on a black surface, where: $\Delta p_{\text{black}} = 0 - p = -p$.

> "[...] analytical optical tweezers have developed into a powerful tool in molecular biology, biochemistry, and biophysics, where they are used to manipulate and interrogate individual molecules. From these studies, scientists are gaining essential new insights into the mechanical properties of biological macromolecules and the dynamics and mechanisms of molecular motors [...] it has become increasingly evident that force is involved in many facets of cellular life, ranging from the obvious—the transport of cellular cargo by motors, such as myosin, kinesin, and dynein—to the more subtle and speculative, such as the strain induced on an enzyme and its substrate during catalysis [...]" — J. R. Moffitt *et al.*, Annual Review of Biochemistry 77, 2008 [14]

This impact is possible, because the range of available (and measurable forces) of optical tweezers lie in the range of forces that are acting on the single molecule level: sub- to hundreds of piconewtons. Here, optical tweezers complement the set of force transducers, such as atomic force microscopes and magnetic tweezers.

2. Physics of optical trapping

A tightly focused beam of laser light forms a potential well where dielectric particles, such as micron-sized polystyrene spheres, can be stably trapped. The formed electromagnetic (EM) field in the focus of the laser polarizes the particle. It is the (complex) dynamic interaction of the time-varying electric field and the polarization[2] of the dielectric that eventually leads to the creation of a potential well. This picture of formation of a potential well is necessary to understand how optical traps work, in detail. Effort has been made to predict, theoretically, what forces act on a particle of radius r from a focused beam of power P and wavelength λ. Different models explain the phenomenon and calculate the expectable forces depending on the relation between the size of the trapped particle and the used wavelength.

2.1. Geometrical optics regime

Probably the most accessible picture to understand optical trapping is given by considering large particles, *i.e.* $R \gg \lambda$. In this regime, the Mie regime, simple ray optics can be used to describe the phenomenon of optical trapping [13, 16]. In this model two forces appear naturally. The first is the scattering force, which is the microscopic picture of what was referred to as radiation pressure. The second is the gradient force, which is caused by a non-uniform incident intensity distribution (Fig. 2.1).

The scattering force is caused by the rays being reflected at the surfaces. The incoming ray experiences Fresnel reflection at the particle's surface, *i.e.* a fraction R of the ray is being reflected. Thus, the momentum of this very part of incident light is changed. Also, the transmitted fraction, T, of the ray will be reflected inside the particle, which will also contribute to the integral of all momentum changes. The rate of momentum change of the light is equal to the force that is acting on the sphere:

$$F_{\text{scat}} = Q\frac{n_{\text{m}}P}{c}, \tag{2.1.1}$$

where n_{m} is the refractive index of the medium and c is the speed of light. The constant of proportionality is given by the dimensionless efficiency factor $Q = \sigma/G$. In general, it relates the interacting cross section[3], σ, to the geometrical cross section, which, for a sphere, is given by $G = \pi r^2$ [5]. In the geometrical model of optical trapping, Q depends on the Fresnel reflectivities and transmittivities.

Each ray of power P experiences a momentum change. The power is given by $P = I_0(\vec{r})A$, where A the area and I_0 is the irradiance, which depends on the position $\vec{r}$. The integral

[2] The electric field, $\vec{E}$, oscillates in time with the angular frequency $\omega = 2\pi c/\lambda$, c being the speed of light (in the medium) and λ is the wavelength. The polarizability of a material is proportional to its susceptibility, which is in general a function of frequency ω that determines the time-response of the dielectric to the field. It might further depend on the particles orientation, the amplitudes of the E-field, and more.

[3] The interacting cross section is the so-called extinction cross section. It is defined by the sum of the

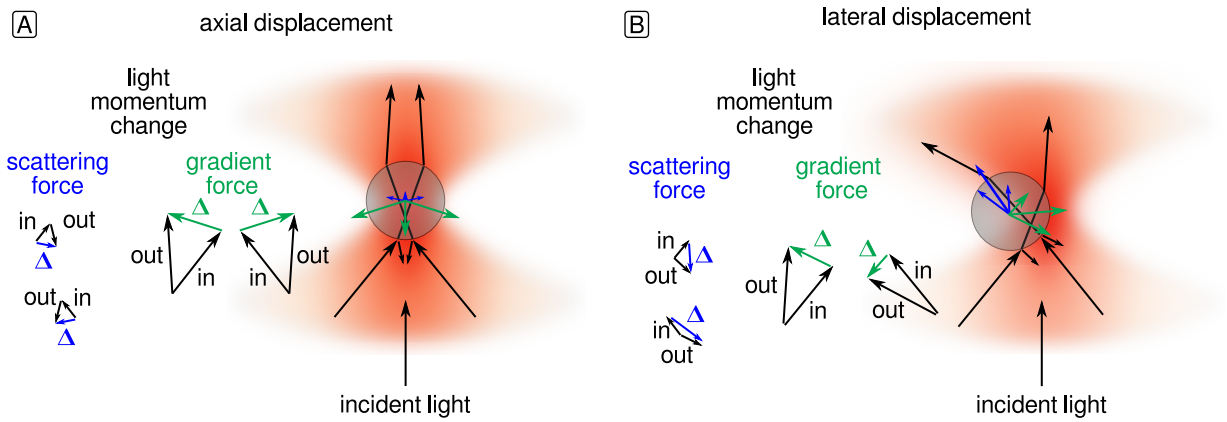

Fig. 2.1 | Principle of optical trapping. The schematics explain the momentum change of the incident light by the use of geometrical optics. In this picture, two forces arise: the gradient and the scattering forces that are caused by refraction and reflection of the incident light, respectively. The schematic shows the arising momentum changes when a particle is displaced axially **(A)** and when a particle is displaced laterally **(B)** from the trap center. The schematic was adapted from Ref. [15].

over all momentum changes of the reflected (and absorbed) rays is the scattering force. For a particle located in the focus, the forces of the rays off the optical axis, the lateral components of the forces cancel out, leaving the axial components. Hence, the scattering force points in the direction of the propagation of the incident rays and displaces the trapped particle from the trap center along the propagation of the incident light.

The gradient force appears because of the non-uniform irradiance, I_0. The transmitted fraction of an incident ray experiences refraction according to Snell's law

$$n_\mathrm{m} \sin\theta = n_\mathrm{p} \sin\theta', \tag{2.1.2}$$

where n_p is the refractive index of the particle and θ and θ' is the angle of incidence and angle of refraction, respectively. Again, the momentum of the ray changes—once when entering the particle and another time when exiting. The momentum change is proportional to the intensity of a ray, which is proportional to the number of photons belonging to it. Hence, the rate of light momentum change is higher for more intense rays, leading to a higher force on the particle. For particles with a refractive index larger than the surrounding medium, *i.e.* the relative refractive index is $m = n_\mathrm{p}/n_\mathrm{m} > 1$, the integral of all forces points toward the intensity gradient, which is toward the center of the focus. Complete forms of both forces, depending on T and R are given by Ashkin [13].

absorption and the scattering cross section [5]:

$$\sigma_\mathrm{ext} = \sigma_\mathrm{abs} + \sigma_\mathrm{scat}.$$

Nonetheless, most of the models describing optical trapping focus on the description of the scattering cross section.

2.2. Rayleigh regime

For particles that are very small compared to the wavelength, *i.e.* $r \ll \lambda$, Rayleigh scattering theory can be applied to explain optical trapping. The particle is modeled as a point dipole. The scattering force arises due to absorption and re-emission of the incoming E-field. For the scattering force the efficiency factor for a spherical particle becomes [16]

$$Q_{\text{scat}} = \frac{\sigma_{\text{scat}}}{\pi r^2} = \frac{128\pi^4 r^4}{3\lambda^4}\left(\frac{m^2-1}{m^2+2}\right)^2 \tag{2.2.1}$$

The equation shows the remarkable dependence of the scattering force on the particle size as it is proportional to r^4. The gradient force for a point dipole is given by

$$F_{\text{grad}} = \frac{2\pi\alpha}{cn_{\text{m}}^2}\nabla I_0, \tag{2.2.2}$$

where ∇I_0 is the gradient of the incident irradiance. The polarizability, α, of a sphere is given by

$$\alpha = n_{\text{m}}^2 r^3 \left(\frac{m^2-1}{m^2+2}\right). \tag{2.2.3}$$

The direction of the gradient force only points along the intensity gradient, if the refractive index of the sphere is larger than the one of the medium. In the sense of an efficiency factor, Q would be an operator, given by $Q_{\text{grad}} = \frac{2r}{n_{\text{m}}}\nabla$. Because the physics is the same for both forces, effort has been made to also develop a unified formulation where only one averaged force term explains the phenomenon [17].

2.3. Intermediate Mie regime

When the dimensions of the particle and the wavelength are comparable, (*i.e.* $r \sim \lambda$) none of the above concepts apply. Neuman and Block name it:

> "Unfortunately, the majority of objects that are useful or interesting to trap, in practice, tend to fall into this intermediate size range [...]" —Neuman and Block, Rev. Sci. Instrum. 2004 [16]

In this range, the generalized Lorentz-Mie theory can be applied, using the Maxwell stress tensor to determine the interaction between the electromagnetic field and the momentum of the particle. Numerical calculations can be performed to predict the arising forces. The Optical Tweezers Toolbox uses the T-matrix approach to describe the interaction between the incident and the scattered field [18, 19]. However, although theories and methods exist that predict the trapping behavior of particles, calibration of a trapped particle is still necessary, in practice.

Part II.

Instrument design

3. Environment of the instrument

The experimental setup is a home-built optical setup that combines optical tweezers with total-internal-reflection fluorescence (TIRF) and interference reflection microscopy (IRM). While the included microscopes have moderate needs to the stability of the system, optical tweezers, in particular, have a high demand on the stability to achieve high precision measurements.

To stabilize an instrument one needs to minimize drift and isolate the instrument from sources of noise. To achieve this isolation, the instrument is located in a laboratory in the basement to reduce the effect of building vibration and temperature changes due to daily variations. Further, the instrument is setup in a room separate from the laboratory space. This separation isolates the instrument from acoustic noise and temperature changes (see also Section 6.1). To isolate the instrument from vibrations transmitted through the building, the

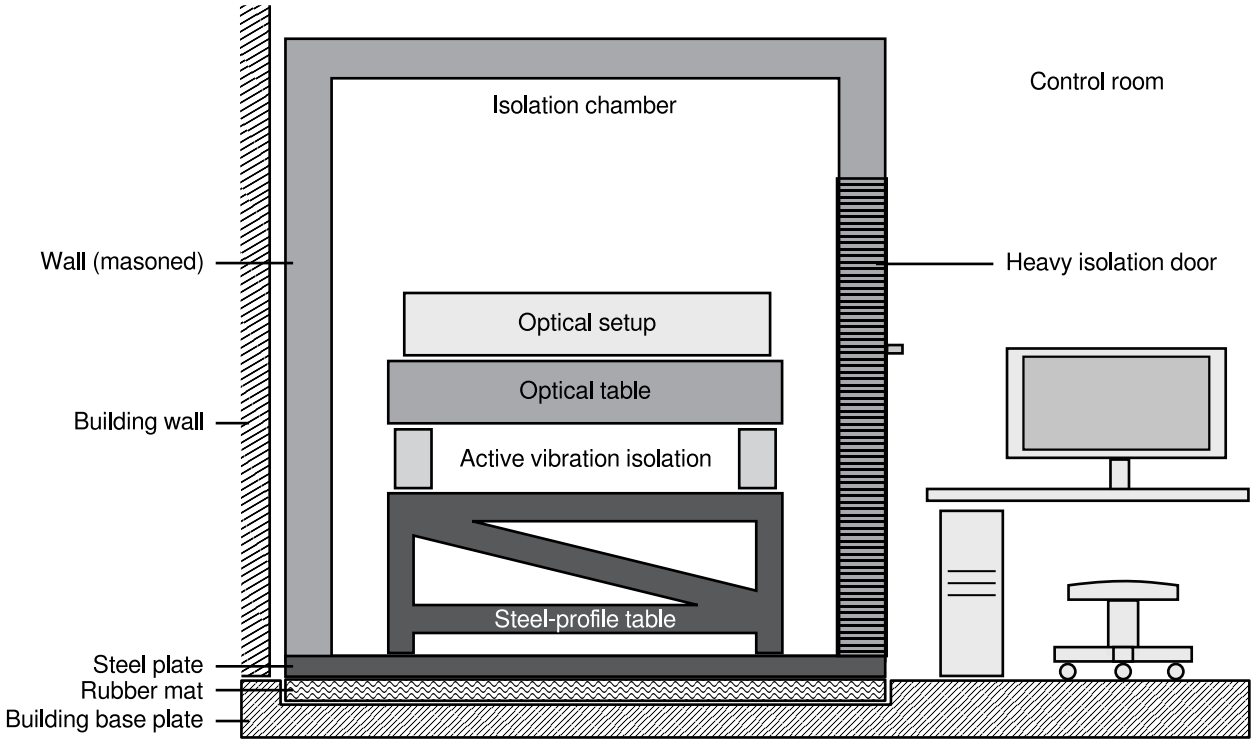

Fig. 3.1 | Isolation chamber. The instrument is located in the basement of the building inside an isolation chamber, separate from the laboratory space from which the it is controlled.

instrument is build on top of an optical table made for high precision instruments (1HT10-12-20, Standa, Lithuania). The table is mounted on an active vibration isolation system (see Section 7.1), which is mounted on a heavy custom-made steel-profile frame.

The optical components are, further, enclosed in a custom-made case. This protects the optics (to an extent) from accumulation dust and isolates the instrument from acoustic noise, air convection within the room, *e.g.* when changing a sample and temperature changes.

4. Optical design of the instrument

4.1. Design objectives

The optical setup is based on the design principle of another home-built optical tweezers setup [20]. A schematic of the optical design is shown in Fig. 4.1. The design aimed to combine precise near-surface measurements of forces and displacements with single-molecule fluorescence microscopy.

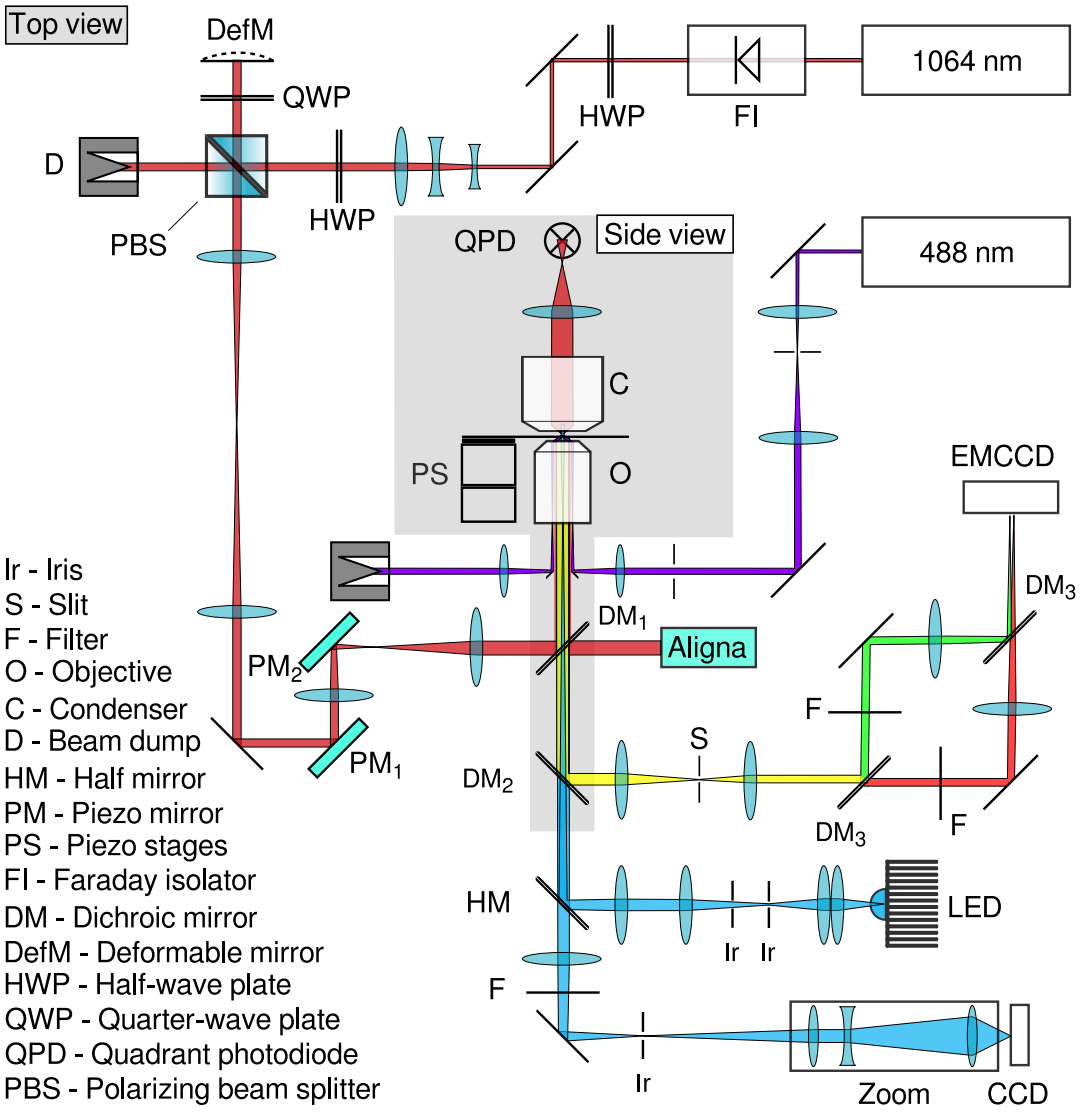

Fig. 4.1 | Schematic of the optical tweezers setup.

The design of the optical trap, as well as the design of the (opto-) mechanical parts of the instrument, were completely revised to improve shortcomings of its predecessor and enhance stability. To this end a three-dimensional steering of the trap position was realized by a combination of a deformable and two piezo-driven mirrors. The former is used to displace the trap rapidly and robustly in the axial direction. The latter are part of a laser stabilization system, which can displace the trap laterally and reduce position and orientation fluctuations of the laser. The latter required to include a four-dimensional laser position detector unit.

Furthermore, the microscope was extended for fluorescence detection of two separate fluorophores. Fluorescence excitation was realized via total internal reflection. During the development, the differential interference contrast (DIC) microscope was replaced by the simpler interference reflection contrast microscope, which is described in detail in Chapter 13.

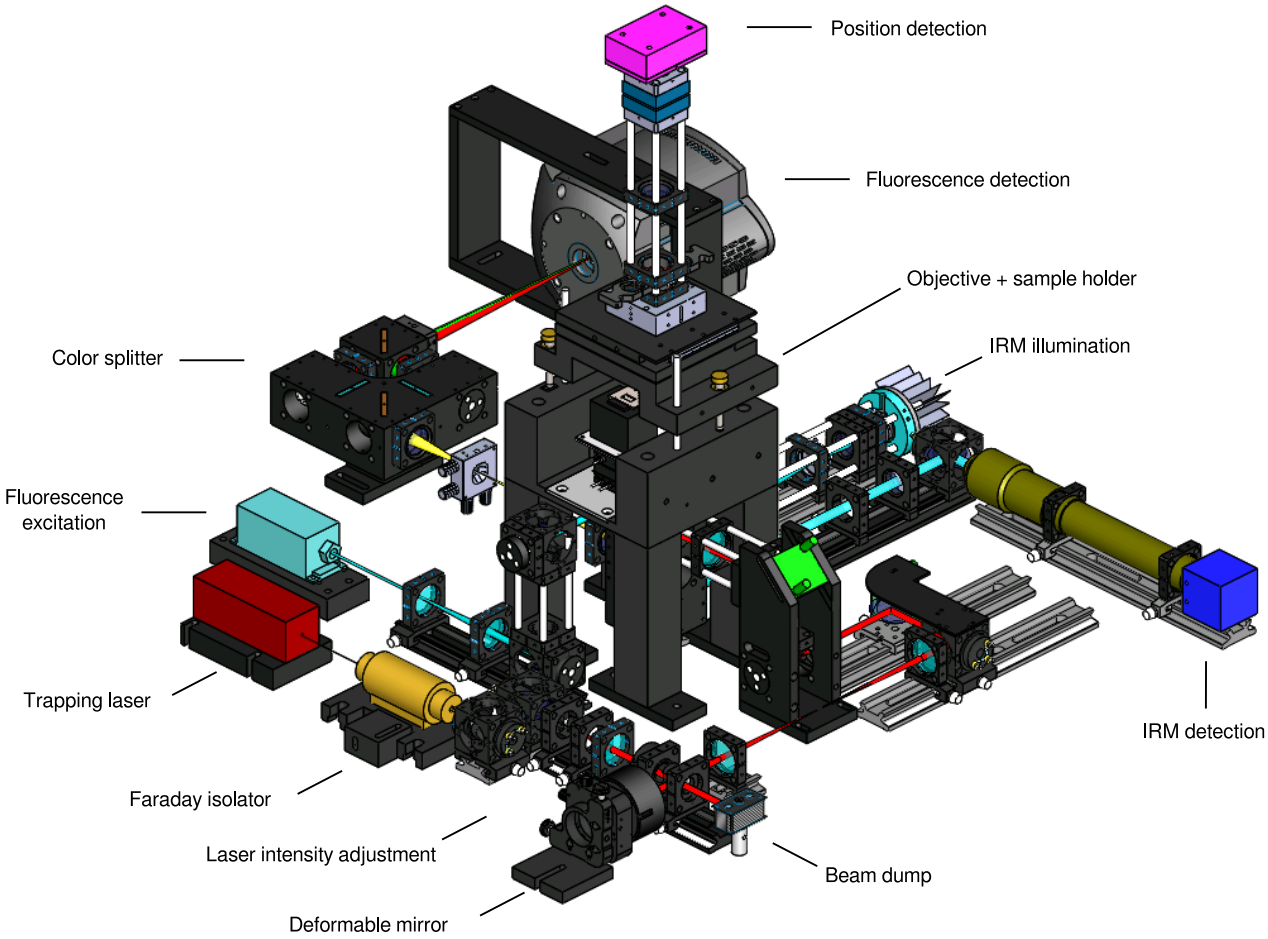

Fig. 4.2 | 3D construction model of the optical tweezers setup.

The instrument was designed via the help of computer aided design software (SolidWorks, Dassault Systémes, France, see Fig. 4.2). The following sections elaborate on the optical design of the instrument. The setup consists of commercially available optical and optomechanical parts. If not otherwise stated, all lenses, lens mounts and rails were acquired from Qioptic Photonics (Göttingen, Germany). Dichroic and half-mirrors and fluorescence emis-

sion filters were acquired from AHF Analysetechnik (Tübingen, Germany).

4.2. Design of the optical tweezers

4.2.1. Preparation of the trapping laser path

The optical tweezers is based on a 3 W diode-pumped solid state YVO_4-laser (Smart Laser Systems, Germany). The laser continuously emits light with a wavelength of 1064 nm. It is superior in terms of pointing and power stability (see Section 7.2). The laser light is linearly polarized perpendicular to the optical table.

The laser passes a Faraday isolator to avoid etalon fringes. Fringes occur because of standing waves formed by small amounts of the laser that get reflected on optical surfaces, such as lenses or plane optics in particluar. The reflected light could eventually interfere with the beam and produce interference patterns, namely etalon fringes [21]. These fringes could, further, lead to multiple traps within the sample.

The isolator rotates the direction of linear polarization by 45°. A half-wave plate (HWP) is used to restore the polarization direction before the laser is precisely aligned to the optical axis via the following two mirrors. This alignment is necessary, because reflectivities are in general different for p- and s-polarized light, which can be seen from the Fresnel-equations [22]. The difference in the reflectivities leads to elliptically polarized light, if the linear polarization direction is not purely p- or s-polarized.

4.2.2. Magnification of the trapping laser

The subsequent telescope is used to magnify the laser beam diameter. A 3-lens Galilean telescope is constructed by two plan-concave lenses and one plan convex lens with focal lengths of −30 mm and 60 mm, respectively. A geometrical ray tracing of the Galilean expansion is shown in Fig. 4.3A. Using a beam profiler (Cinogy Technologies, Germany), the telescope was adjusted to magnify the beam diameter to (5.00 ± 0.01) mm. The usage of a 3-lens Galilean telescope over a commercial beam magnifier is the flexibility to adjust the magnification of the laser beam—although with some labor—within a certain range and being cost efficient. Using a Galilean over a Keplerian telescope avoids to focus the laser beam, which would heat up the air and could lead to convection and, thus, disturbance of the laser beam.

4.2.3. Laser intensity adjustment

The following unit is used to adjust the trapping laser intensity. It is realized by a combination of a HWP and a polarizing beam splitter (PBS, Edmund Optics). A HWP is mounted on an axial ball bearing. The orientation of its fast optical axis is remotely controlled via a servomotor to rotate the polarization direction of the laser. The orientation of the HWP defines the fraction of p- vs. s-polarized light with respect to the PBS. The PBS transmits the p-polarized and reflects the s-polarized fraction of the laser. Transmitted light hits a beam dump. In order to avoid convection of air due to heat being generated inside the enclosure, the beam dump is located outside the beam path enclosure.

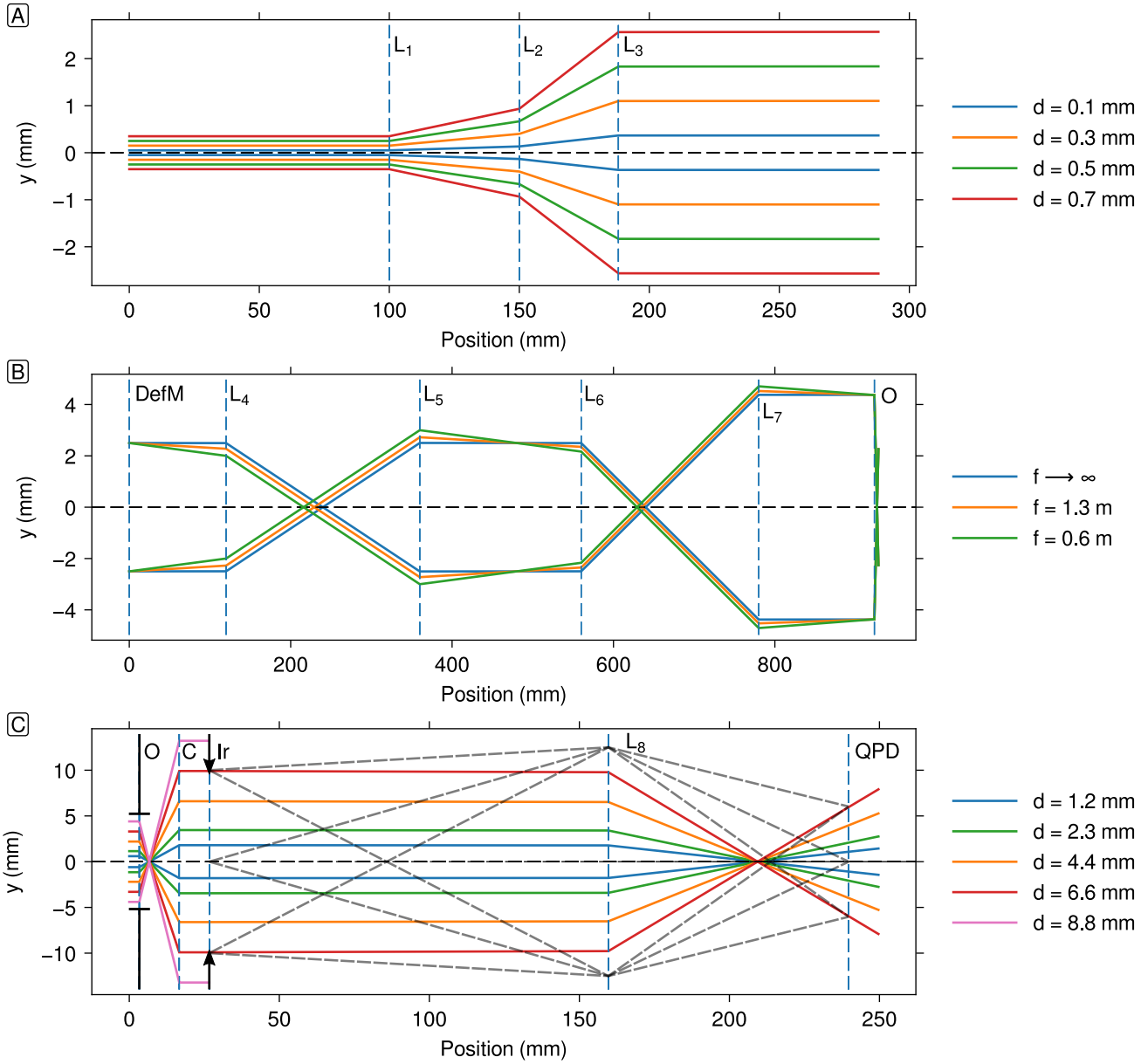

Fig. 4.3 | Ray tracing of the trapping laser. **(A)** 3-lens Galilean telescope to magnify the beam diameter 7× to (5.00 ± 0.01) mm. **(B)** Optical path starting at the deformable mirror (DefM) passing both Keplerian telescopes and the objective (O) reaching the sample plane. The sample plane is conjugate to the focal plane between lenses L_5 and L_6. The different traces show the influence of deformation of the mirror corresponding to a plane mirror ($f \to \infty$) down to $f = 0.6$ m. The axial range at which the focal point can be moved corresponds to 5.4 µm. **(C)** Back-focal plane detection traces. The condenser iris (Ir) confines the imaging NA to 1.0, which corresponds to a conjugate image size of 21 mm in the BFP of the condenser (C). This image is de-magnified by the relay lens L_8 and projected on the QPD, which is indicated by the axial, chief and marginal rays (dashed gray lines).

4.2.4. Axial trap position control unit

The next unit in line, controls the axial position of the trap. It consists of a quarter-wave plate (QWP) and a deformable mirror (DefM, MMDM10-1-focus, OKO Technologies, The Netherlands) [23]. After the s-polarized fraction of the laser is reflected by the PBS, the light passes a QWP, which adds a phase shift of $\pi/2$ between the superposed orthogonal EM-waves. Hence, the laser light gets circularly polarized and hits the DefM.

Because, at normal incidence, p-polarized light undergoes a phase shift of π, whereas the s-polarized light does not [22], the chirality of the circularly polarized light changes upon reflection off the DefM. The light passes the QWP a second time, which converts the polarization state back to linear ($\Delta\phi = \pi/2 \pm \pi - \pi/2 = \pm\pi$). Because of the net phase shift of π the linear polarization orientation has changed by 90°. Hence, the light is now p-polarized with respect to the PBS and passes it. The axial position control is discussed in more detail below.

4.2.5. Afocal lens system to propagate image- and conjugate planes

The following two Keplerian telescopes form an afocal system[4] that relay the optical plane of the DefM into the back focal plane (BFP) of the objective. After the first telescope, the laser passes two mirrors that can be tilted by piezo-actors. The tiltable mirrors are part of the laser stabilization system Aligna® (see below).

The first telescope is made by two lenses L_4 and L_5 with equal focal length $f_4 = f_5 = 120\,\mathrm{mm}$. The second telescope magnifies the beam by $M_3 = f_7/f_6 = 140\,\mathrm{mm}/80\,\mathrm{mm} = 1.75\times$. After the laser has passed both telescopes, the beam has a diameter of $2\omega_0 = 8.8\,\mathrm{mm}$, where ω_0 is the laser beam radius where the intensity has dropped by a factor of e^2 with respect to the central value. A dichroic mirror (F33-725, AHF Analysentechnik, Germany) reflects the laser beam into the objective lens, which tightly focuses the laser and eventually forms an optical trap in the sample chamber.

4.2.6. Formation of the optical trap

The objective lens (CFI Apo TIRF 60× oil, NA 1.49, Nikon Instruments) is a high numerical aperture objective, suitable for TIRF microscopy. It has a focal length of

$$f_{\mathrm{obj}} = \frac{f_{\mathrm{tube}}}{M_{\mathrm{obj}}} = 3.33\,\mathrm{mm},$$

where $f_{\mathrm{tube}} = 200\,\mathrm{mm}$ is the mechanical tube length specified by the manufacturer [25] and $M_{\mathrm{obj}} = 60\times$ is the specified lateral objective magnification. Using aqueous samples, the usable NA of the objective reduces to the refractive index of water. Thus, the usable exit-pupil diameter of the objective reduces to

$$d_{\mathrm{ep}} = 2\,NA\,f_{\mathrm{obj}} = 8.8\,\mathrm{mm}.$$

The sample is mounted on a long-range open-loop (MX-35, Mechonics, Germany) and a short-range, high-precision, closed-loop piezo-driven stage (PI Hera 620 XYZ, Physik Instrumente, Germany).

[4] From the glossary of Ref. [24] "afocal system: An optical system which forms an image of infinitely distant object at infinity, *i.e.* a system where both input and output beams are collimated. [...]"

4.2.7. Detection of the trapping laser

Back focal plane interferometry is used to track displacements of trapped particles [26, 27]. The transmitted laser light is collected by a condenser lens (D-CUO Achr.-Apl. NA 1.4, Nikon Instruments). A single lens ($f = 50\,\mathrm{mm}$) relays the image of the BFP of the condenser onto a quadrant photo diode (QP154-Q-HVSD, First Sensor AG, Germany). The image of the BFP of the condenser lens is de-magnified 0.6×, to fit the size of the QPD (gray dashed lines in Fig. 4.3C). The QPD is chosen for its specified enhanced bandwidth for infrared wavelengths ($\approx 120\,\mathrm{kHz}$ at $1064\,\mathrm{nm}$) .

4.3. Design of the TIRF microscope

4.3.1. TIR excitation

The total internal reflection fluorescence microscope uses a diode-laser with a wavelength $\lambda = 488\,\mathrm{nm}$ for the excitation of fluorescent dyes, such as GFP. It has a maximum output power of 80 mW (PhoxX 488-80, Omicron-Laserage, Germany). The laser is guided into the objective via a mirror (Fig. 4.4A) ($\varnothing = 2\,\mathrm{mm}$) that is mounted at 45° on a piezo-driven stage (M3-L, NewScale Technologies, USA). The stage enables to position the laser beam at a desired distance from the optical axis. This allows to adjust the angle at which the laser exits the objective.

To illuminate the sample uniformly by an evanescent field, the excitation laser has to be focused into the BFP of the objective. The depth of the evanescent field depends on the angle of incidence. Therefore, a collimated beam needs to exit the objective. If this was not the case, different angles of incidence would lead to gradually changing depth of the evanescent field. Collimation of the excitation laser is achieved by a lens that focuses the beam into the objective's BFP (Fig. 4.4B). To keep the design compact the focusing lens was mounted before the mirror. If the focusing lens was stationary, a translation of the small-mirror-stage would change the optical path length. Therefore, the lens was mounted on the stage as well. This implementation kept the location of the focal plane constant with respect to the objective and provided a collimated laser exiting the objective.

To avoid unnecessary photo-bleaching of fluorophores in the sample, the illuminated spot was confined to the field of view of the fluorescence microscope (see below). The beam diameter, d_{beam} and the telescope, which is formed by the focusing lens and the objective, defines the illuminated spot size in the sample:

$$d_{\mathrm{i}} = d_{\mathrm{beam}} \frac{f_{\mathrm{obj}}}{f_{\mathrm{T3}}}, \tag{4.3.1}$$

where $d_{\mathrm{beam}} = 1\,\mathrm{mm}$ and $f_{\mathrm{T3}} = 60\,\mathrm{mm}$, hence $d_{\mathrm{i}} = 55\,\mu\mathrm{m}$.

Furthermore, to avoid non-uniform illumination of the sample the laser beam was magnified and the Gaussian beam profile was cropped. A Gaussian beam profile inherently illuminates the sample inhomogeneously[5]. If a fluorescent sample was excited by a Gaussian beam profile, the illumination intensity between the center and the edge of a field of view (with a size of $2\omega_0$), would drop by a factor e^{-2}. To approximate a homogeneous illumination, the beam was magnified and cropped so the difference would be about 10%. To keep

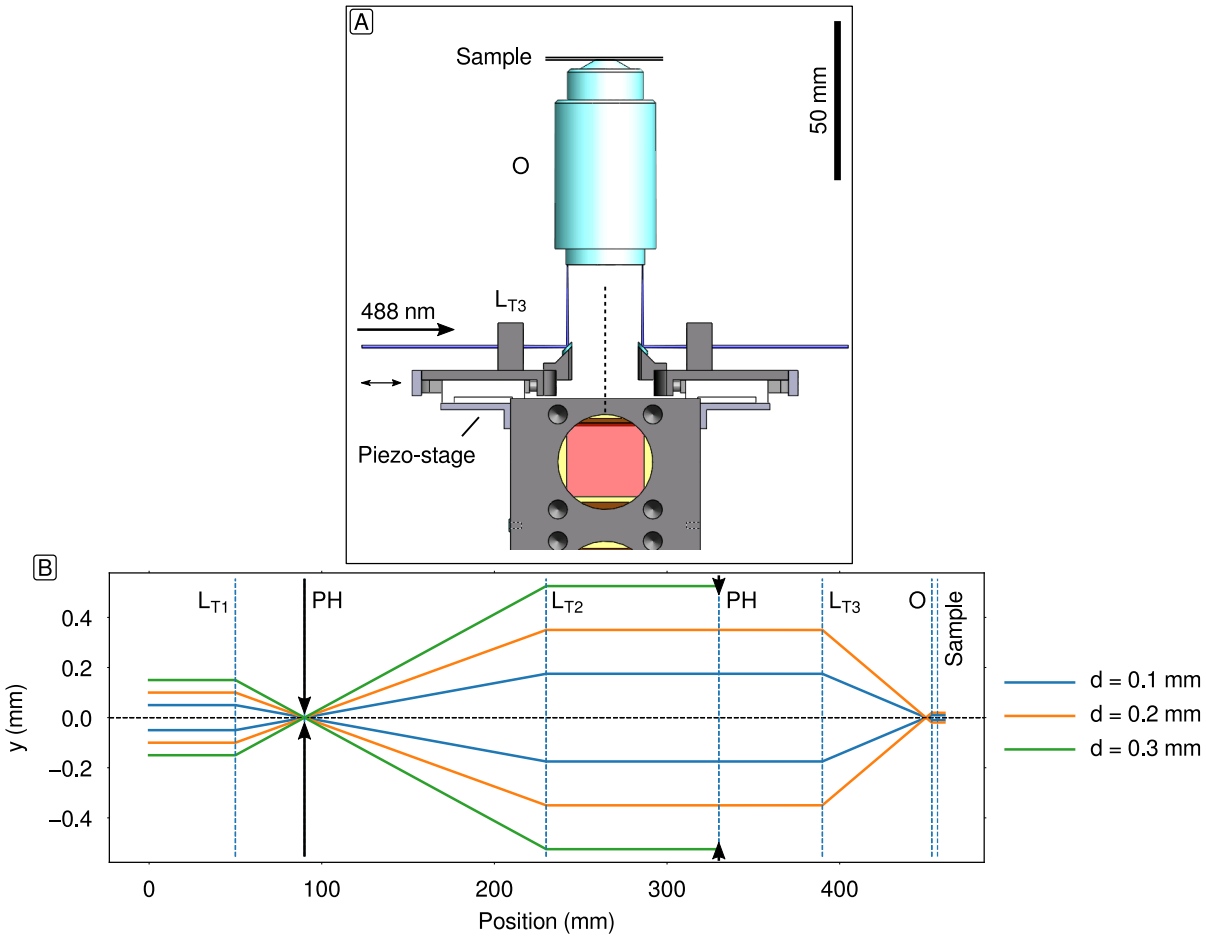

Fig. 4.4 | Fluorescence excitation by total internal reflection. (A) TIRF excitation design. A laser is focused into the BFP of the objective. The distance of the vertical beam to the optical axis defines the angle of incidence. **(B)** Geometrical ray tracing of the (epi-) fluorescence excitation path. To confine the beam diameter in the sample plane a pinhole (PH) between lenses L_{T2} and L_{T3} is used.

the illumination area the same, a pinhole with a diameter of $d_p = 1\,\text{mm}$ is put into the FFP of the focusing lens. The required beam diameter can be calculated to be [28]

$$d = \sqrt{\frac{2\,d_p}{\ln\left(\frac{10}{9}\right)}} = 4.4\,\text{mm}. \tag{4.3.2}$$

Thus, using a Keplerian telescope consisting of a 40 mm and a 140 mm lens, the laser was magnified 3.5×.

The telescope was further used to clean up the laser profile by the use of a Fourier filter. To produce a beam profile that only contains the fundamental (Gaussian) mode, a pinhole

[5] A Gaussian beam intensity profile in the focal plane is given by

$$I(r) = I_0 \exp\left(-2\frac{r^2}{\omega_0^2}\right),$$

where I_0 is the intensity at the center, ω_0 is the beam radius and r is the distance from the beam center.

was put into the focus of the telescope. The diameter of the pinhole was chosen to be smaller than the size of the theoretical Airy pattern (2× the distance from the center to the first minimum) [29]:

$$d_{\mathrm{f}} \leq d_{\mathrm{Airy}} = \frac{1.22\lambda}{NA} = \frac{2.44\lambda f}{D} \approx 40\,\mu\mathrm{m}, \tag{4.3.3}$$

where $NA = D/(2f)$ is the numerical aperture of the focused laser, with a beam diameter, $D = 1.2\,\mathrm{mm}$ and a focal length, $f = 40\,\mathrm{mm}$, of the focusing lens.

4.3.2. Fluorescence detection

Fluorescent light is collected by the objective with the objective's full NA of 1.49. Light with a wavelength $> 510\,\mathrm{nm}$ is reflected by a dichroic mirror (F73-510, AHF Analysentechnik,

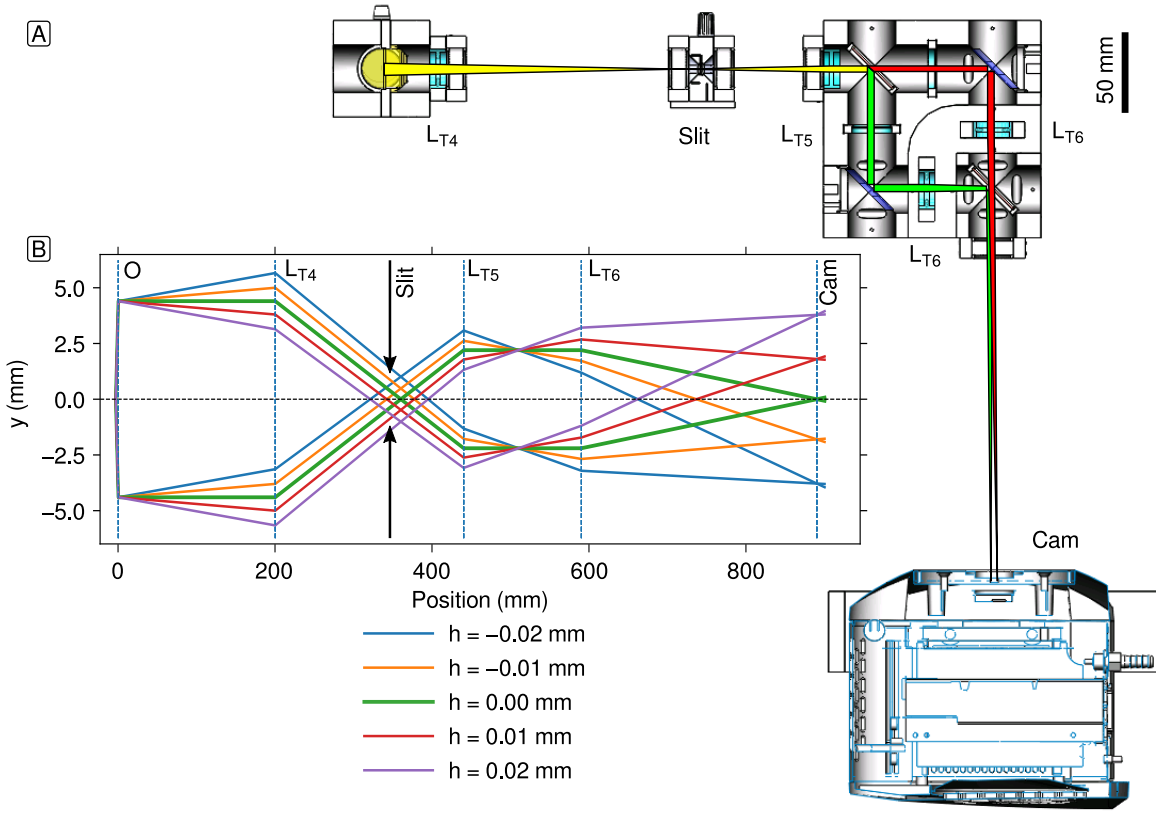

Fig. 4.5 | Design of the fluorescence detection. (A) CAD design of the fluorescence detection path. Starting from left, the fluorescent light (yellow beam) is collected by the objective passing an adjustable slit, which confines the field of view, and entering the color splitter. The color splitter splits the light into two beams at a wavelength $\lambda = 560\,\mathrm{nm}$ and independently focuses the beam on the EMCCD camera. **(B)** Fluorescence detection ray tracing showing the confinement of the field of view by the adjustable slit and the magnification of the image by the telescope formed by the lenses $\mathrm{L_{T5}}$ and $\mathrm{L_{T6}}$.

Germany) toward the fluorescence detection path (Fig. 4.5). A 160 mm tube-lens forms an image of the sample and an adjustable slit (Spalte SP 40, Owis, Germany) confines the field of view. A 80 mm lens is used to collimate the light again. The following unit is used to split the green and red emission. The unit was independently developed and investigated simultaneously by Jiang *et al.* [30]. This implementation splits the fluorescent light into a "green" and "red" path by the usage of dichroic mirrors (F38-560, AHF Analysentechnik, Germany) and focuses both colors independently onto an electron multiplying CCD camera (iXon3, Andor Technology, UK). In both paths, emission filters (F37-520 in the green and F47-605 in the red path , respectively) are used to block light of other wavelengths and reduce crosstalk (bleed-through) between the channels. The mirrors in the corners of the color splitter are used to laterally adjust the images on the camera.

4.4. Design of the LED-based IRM

The LED-based interference reflection microscope consists of a few simple optical components (Fig. 4.6). For illumination, a blue LED (Royal-Blue LUXEON Rebel LED, Lumileds, Germany) was used, which emits light at $\lambda = (450 \pm 20)$ nm with 525 mW at 700 mA. To provide thermal stability—especially at high currents—the LED was mounted on a large aluminum heat sink (Fisher Elektronik, Germany). The driving current is provided by a DC power supply (Agilent E3648A, Keysight, Böblingen, Germany). An image of the LED is magnified by two telescopes and projected into the BFP of the objective lens to Köhler-illuminate the sample. An aperture iris is placed at the first image plane of the LED, which is conjugate to the BFP. This iris truncates the LED image and, thus, avoids total internal reflection. With the aperture iris, the illumination numerical aperture (INA) can also be adjusted. A field iris limits the illumination area in the sample-plane, *i.e.* the front-focal plane of the objective. The detection and illumination light path are separated by a 50/50 beam splitter plate (BS) (F21-000, AHF Analysentechnik, Germany). Half the reflected light from the sample passes the beam splitter. A 200 mm tube lens and an adjustable zoom (S5LPJ7073, Sill Optics, Germany) magnify the sample image about 165× and project it onto a CCD camera (LU135-M, Lumenera, Canada). Note that the use of an Antiflex objective and linearly polarized light did not improve the image contrast significantly.

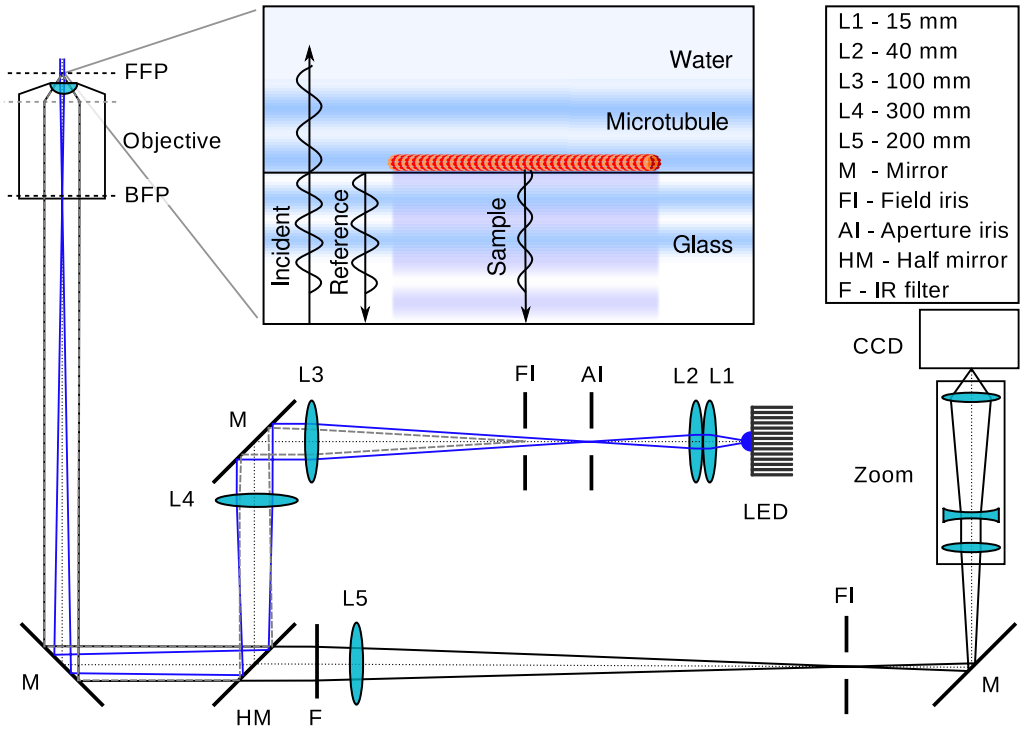

Fig. 4.6 | Schematic of the IRM design and principle. The optical path is drawn to scale and shows the marginal rays of the LED (blue lines), the sample (black lines), and the field iris (dashed gray lines). The incident light of the Köhler-illuminated sample is reflected from the glass-water interface (reference) and the specimen (sample), here a microtubule, which interfere to form the final signal. Note that the light fields are illustrated at normal incidence, which would correspond to an illumination numerical aperture (INA) of zero. A higher INA leads to tilted wavefronts, which are omitted for clarity.

5. Instrument control and electronic design

5.1. Control overview

5.1.1. General instrument control

The instrument is a combination of many separate devices that need to interact and be controlled. Control is realized via a PC using proprietary control software shipped with a device or self-written LabVIEWprograms, so-called virtual instruments (VIs). Communication is done either via serial connections, such as RS232 and USB, parallel communication through PCIexpress and by analog control signals. VIs manage the communication between the PC, the sample-clocks provided by the data acquisition cards and the devices. VIs also manage the acquisition of data signals, such as the ones of the QPD, the stage position or the temperature sensors. An overview of the control and information flow is given in Fig. 5.1. Each of the four major functions of the instrument, the optical trap, the sample positioning and the two microscopy techniques, have sub-devices or properties that are controlled through a variety of other devices.

5.1.2. Optical trap

The trapping laser intensity is controlled trough a servo motor. Its position is set via a control VI converting the input relative laser intensity to a servo motor position. The VI also controls the supply voltage of the servo. To increase the lifetime of the servo, the supply voltage is only switched on for changes of the servo position. Similar to the laser intensity, a servo motor is also used to operate the laser shutter.

The displacement of trapped particles is measured with the QPD. Its position can be changed relative to the optical axis of the transmitted trapping laser by controlling either the MechOnics MS38 piezo-stage (MechOnics, Germany) or by changing the position of the condenser via the smarAct piezo stages (SLC-1780, SmarAct, Germany). The QPD signals are acquired through the analog input data acquisition card (NI PXI-4472B). The card uses delta-sigma analog to digital conversion to suppress aliasing [31]. The QPD is powered by $\pm 15\,\mathrm{V}$ provided by Power Supply 4. To enhance the QPD's bandwidth a bias voltage is additionally provided via five 9 V block batteries connected in series.

The trap position in the sample can be controlled laterally via the Aligna laser stabilization system and axially via the deformable mirror (see Section 5.2). Both are controlled via analog voltages provided by an NI PXI-6733 card.

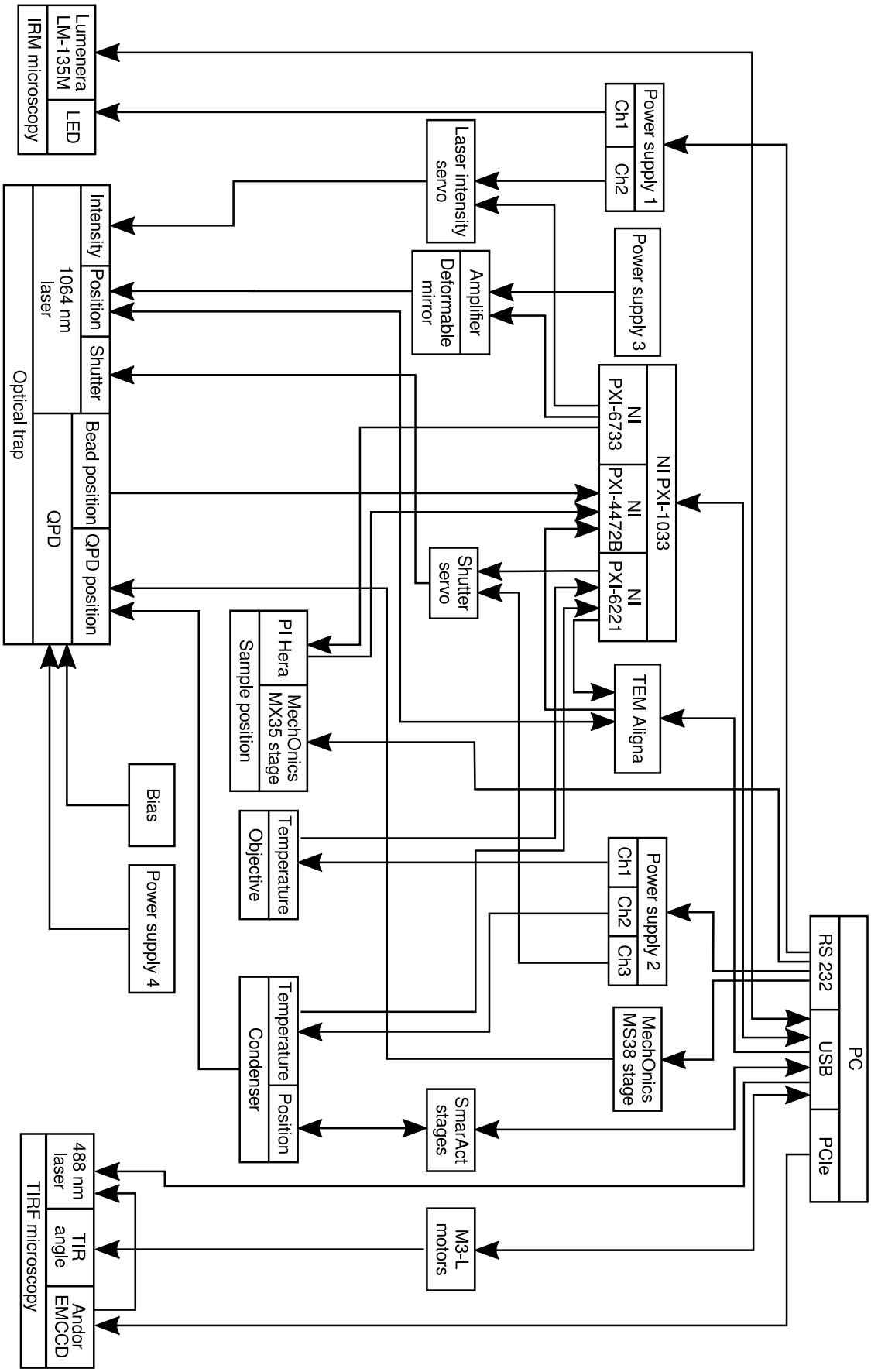

Fig. 5.1 | Control graph of the combined optical tweezers setup.

5.1.3. Sample position

The sample can be positioned by a long-distance travel MechOnics MX35 (MechOnics, Germany) open-loop piezo-stage with a range of 10 mm in all three axes. The stage is controlled via the same controller as the QPD piezo stage, using the same VI. A home-built switch, which is based on an Arduino micro-controller, is used to switch between the two stages via a digital control signal.

Precise positioning is done via a PI Hera piezo-stage with a travel range of 50 µm in all three dimensions. The position is controlled in closed-loop via a PI E509.C3A servo controller. The setpoint is adjusted via analog voltages supplied by a NI PXI-6733 card. The position sensor signals of the stage are acquired with the NI PXI-4472B card.

5.1.4. IRM microscope

The IRM microscope uses a standard USB camera that is operated through a LabVIEW VI. The VI manages live imaging with dynamic contrast adaption and recording with defined exposure times. Another VI controls a constant current output from Power Supply 1 to set the LED intensity.

5.1.5. TIRF microscope

Fluorophores are excited by the Omicron 488 nm laser. Its power is controlled via a proprietary control software. The laser is triggered by the Andor EMCCD camera. The camera can be controlled either by Andor's Solis software or by the free and open source microscopy software Micro-Manager[6] [32]. To change the angle of incidence of the TIRF excitation laser, the position of the M3-L piezo motors is adjusted via proprietary control software.

5.2. Three-dimensional control of the trap position

5.2.1. Axial steering of the trap

Axial steering of the trap is realized by a deformable membrane mirror (DefM) (MMDM10-1-focus, OKO Technologies, The Netherlands). The DefM consists of a thin membrane mirror that can be deformed by applying a voltage between the membrane and an electrode behind it. The optical power can be adjusted between 0 (plane mirror) and 1.5 m^{-1} (parabolic mirror), which corresponds to a focal length between infinity and 0.66 m. Figure 4.3B shows the geometrical tracing of the rays for different focal lengths. Because the lenses L_4–L_7 and the objective form an afocal system, the changed focal lengths of the DefM do not change the beam diameter in the BFP of the objective. Therefore, the beam is not cut off by the objective's exit pupil aperture and the laser intensity stays constant while changing the axial position of the trap.

The trap position change is proportional to the square of the control voltage. To control the position of the optical trap in the sample, the actual trap position at a given control voltage was measured to determine its functional dependency. The position of the trap

[6] HTTP://micro-manager.org/

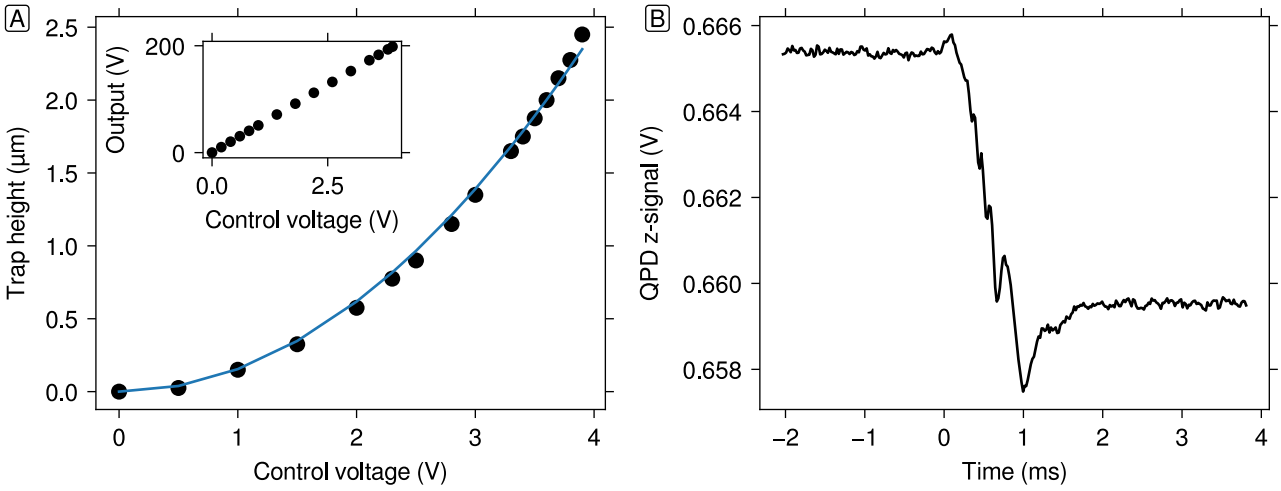

Fig. 5.2 | Calibration and response of the deformable mirror. (A) Trap height vs. control voltage (circles). The trap height is proportional to the square of the control voltage (line). The control voltage determines the output of a high-voltage amplifier (inset). **(B)** Response of the DefM to a control voltage step. The response time of the mirror is $\approx 1.7\,\mathrm{ms}$.

was deduced from the distance of a trapped microsphere to the glass surface. The position of the surface was varied using the piezo translation stage. After a change in the DefM, the calibrated stage was moved until the trapped microsphere touched the surface. The touching point was quantified by a certain noise level. All trap height measurements were relative to each other. The trap height was fitted to a parabola $h_\mathrm{t} = a \cdot U_\mathrm{ctrl}^2$, with $a = (0.154 \pm 0.001)\,\mu\mathrm{m\,V^{-2}}$ (Fig. 5.2A). Taking a linear and constant term into account was unnecessary and corresponded well to the manual.

The accessible range of the trap height was found to be 57% smaller than theoretically expected. Considering the magnifications of the two telescopes the accessible axial range can be calculated from [23]:

$$\Delta z_\mathrm{th} = \left(\frac{f_\mathrm{Obj}}{M_2 M_3}\right)^2 \times \frac{1}{f_\mathrm{DefM}}. \tag{5.2.1}$$

The magnifications are $M_2 = 1$ and $M_3 = 1.75$ (see Section 4.2). Hence, the expected range is $\Delta z_\mathrm{th} = 5.4\,\mu\mathrm{m}$. However, the actual range was found to be $\Delta z = 2.3\,\mu\mathrm{m}$. Since the deformation of the membrane mirror depends on the applied voltage, it is possible, that the range of the used amplifier is insufficient to achieve the specified optical power.

The deformable mirror has millisecond response time. To determine the response time of the mirror, the response of a 0.1 µm step of the axial trap position was measured by a change of the QPD sum-signal (Fig. 5.2B). The measured response time was about 1.7 ms, which corresponds to a bandwidth of about 580 Hz.

5.2.2. Laser stabilization and lateral steering of the trap

5.2.2.1. 4D steering of the laser orientation

To reduce fluctuations of the laser orientation, a laser stabilization system was included into the optical design of the trapping laser path. The system measures the 4-dimensional orientation (tilt and translation in x and y) of the laser and, by the use of two tiltable mirrors, compensates for any change. Additionally, by adjusting the setpoint, the system enables to dynamically set the resting position of the trap in the sample.

Two tiltable mirrors enable to orient a laser in four dimensions: translation in x and y, orthogonal to the optical axis, and inclination of the laser in the $x-z$- and $y-z$-plane. If a mirror is tilted by some angle φ, a reflected beam is tilted by the same angle. The Keplerian telescope formed by the lenses L_6 and L_7 relay the optical plane of the first mirror (PM_1 in Fig. 4.1) into the BFP of the objective lens. An inclination of the trapping laser in the BFP results in a displacement of the trap inside the sample of $\Delta x = \varphi_x f_{\mathrm{obj}}$, with f_{obj} being the focal length of the objective. The telescope de-magnifies the angle, φ_x, by a factor of $1/M_3$, resulting in

$$\Delta x = \frac{f_{\mathrm{obj}}}{M_3}\varphi_x. \tag{5.2.2}$$

To stabilize the laser, the Aligna® system measures the orientation of the laser beam and uses both mirrors to account for changes. To measure the orientation of the beam, two position- sensitive diodes are utilized to independently measure translation, Δx and Δy, and inclination, φ_x and φ_y, of the beam. The laser beam is split up by a 50/50 beam splitter. The first half of the beam directly hits the first diode, whereas the second half is focused on the second diode. If the beam orientation in the BFP of the objective is given by $(\Delta x, \varphi_x)$ then the first diode measures a signal corresponding to a displacement of

$$s_1 = \frac{\Delta x + d\varphi_x}{C_{1,x}}, \tag{5.2.3}$$

where d is the distance from the BFP to the diode and $C_{1,x}$ is the volt-to-meter conversion factor of the diode. The second diode measures a signal corresponding to

$$s_2 = \frac{\Delta x(1 - d_2/f) + \varphi_x\left[d(1 - d_2/f) + d_2\right]}{C_{2,x}}, \tag{5.2.4}$$

where d_2 is the distance between the lens. If $d_2 = f$, Eq. (5.2.4) reduces to $s_2 = \varphi f / C_{2,x}$. Therefore, translation and inclination are measured by

$$\Delta x = C_{1,x}s_1 - C_{2,x}s_2\frac{d}{f} \tag{5.2.5}$$

$$\varphi_x = C_{2,x}\frac{s_2}{f} \tag{5.2.6}$$

The distance d could also be reduced to zero if the BFP was relayed into the plane of the first diode.

Because the tilt axes of both mirrors and the two independent axes of both diodes must not necessarily match each other, there is correlation (crosstalk) between all channels. These

correlations form a system of linear equations. A movement of one mirror in one axis, in general, produces signals in both axes on both diodes. The proprietary software "Kangoo", which is shipped with the Aligna® system, provides a routine to measure the correlation between all axes. The correlations are expressed by a matrix $\mathbf{M}$. Once $\mathbf{M}$ is known the inverse is needed to control the laser position. The software supposedly uses singular-value decomposition (SVD) to calculate its pseudo-inverse $\mathbf{M^{-1}}$ [33]. The manufacturer calles this matrix "output-crosslink-matrix" (OCLM). It is used to calculate the 4-dimensional orientation of the laser beam:

$$(\Delta x, \Delta y, \varphi_x, \varphi_y)^T = M^{-1}(s_{1x}, s_{1y}, s_{2x}, s_{2y})^T. \tag{5.2.7}$$

Further, it is used to orthogonalize the system, to independently steer the laser beam in all four dimensions.

5.2.2.2. Intended stabilization and lateral steering range remains unachieved

The piezo-driven mirrors of the Aligna® system have a specified inclination range of $\Delta\theta = 4.8\,\mathrm{mrad}$. According to Eq. (5.2.2), this range corresponds to a lateral steering range of $\Delta x = 9.1\,\mu\mathrm{m}$. However, only a range of $1.0\,\mu\mathrm{m}$ could be reached so far (Fig. 5.3A and B). The reason for this discrepancy could be an incorrect control of both mirrors. This could be due to a faulty orthogonalization of the control matrix (Eq. (5.2.7)).

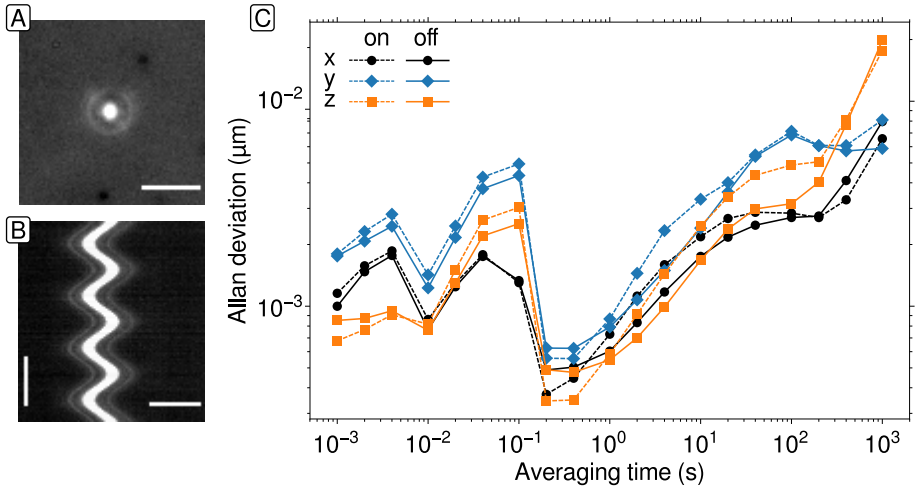

Fig. 5.3 | Laser stabilization system. (A) Trapped polystyrene microsphere with a diameter of $d = 590\,\mathrm{nm}$. **(B)** Kymograph of trapped microsphere in IRM, moved sinusoidally via setpoint control of the Aligna® system. Scale bars: $2\,\mu\mathrm{m}$ (horizontal) and 1 s (vertical). **(C)** Allan deviation plots of a microsphere fixed to the sample surface when the laser stabilization was on and off. No improvement could be seen.

Orthogonalization through the software failed most of the time, which means, that the system was not able to independently translate or tilt the mirror. One possible explanation could be that the two mirrors do not independently steer the beam orientation. The second mirror was built inside the second Keplerian telescope. This might be a conceptual mistake: if the first mirror should steer pure inclination of the beam, the second mirror should steer pure translation. This is not possible in the current design. One solution could be, to move

the second mirror out of the telescope. Because the focus of the laser inside the telescope could harm the mirror, the mirror cannot be positioned at the focal plane of lens L_6.

A laser stabilization could not be detected. To see if there is any improvement in laser stability, a microsphere was fixed on the sample chamber glass-surface and centered with respect to the trap. An improvement of laser pointing stability was expected for signal averaging times much larger than the response-time of the mirrors ($\approx 3\,\mathrm{ms}$). However, no improvement was detected, which can be seen from the Allan deviation-plots in Fig. 5.3C (comp. Section 6.2.3). One reason for this could be the possible design fault, mentioned above. An alternative explanation is that the laser is more stable than the stabilization precision of the system or the fluctuations of the microsphere were larger than the fluctuations of the laser.

To further investigate, if the system could be utilized to improve long-term stability of the optical trap, one could test whether orthogonalization is more robust, if the second piezo-driven mirror was moved outside the telescope. One reason to limit the stabilization precision, is the limited precision of the orientation measurement by the position-sensitive diodes. This could be improved by magnifying the fluctuations of the laser orientation optically, by installing another (magnifying) telescope between the objective's BFP and the Aligna® detector. Also, long-term laser stability might be also measurable by Allan deviation-plots of the position signals of a trapped microsphere. High laser powers would decrease the Brownian movement (white noise regime) and make drift and pink noise more visible (comp. Section 6.2.3).

5.3. Temperature control

5.3.1. Motivation

Optical tweezers operate on a nanometer length scale with sub-nanometer precision. This precision is reached by averaging over time scales on the order of seconds (see Section 7.3). As discussed in Section 6.1, temperature stability plays an important role when pushing the precision capabilities of the instrument.

Heating of the objective and condenser lens causes drift that disturbs high-precision measurements. Because the objective and condenser lens are designed for visible light, the transmission of light outside this spectrum, such as the infrared light of the trapping laser, is rather poor. The objective lens has a transmission at 1064 nm of about 40% [16]. The rest is reflected and absorbed inside, which leads to heating. Heating of the objective leads to thermal expansion and, thus, small displacements between the optical groups inside. Hence, the optical path changes and the focal plane of the objective drifts. Depending on the used laser power, the objective and the condenser may experience a considerable change in the focal plane. Moreover, depending on the heat capacities of the parts and the thermal conductivities between them, the expansion and shrinkage typically depends in an exponential manner on time over timescales of minutes to hours. Thus, equilibration times of the system cause delays in experiments. Such delays can make experiments extremely difficult or even impossible.

Reduction of equilibration times is achieved by heating. This can be understood by considering the following. After the trapping laser shutter is opened, the objective and the

condenser experience thermal expansion caused by heating. An intentionally applied heating to both optics will offset the location of the focal plane. Once the shutter is opened the amount of heating can be decreased such that the position of the focal plane stays the same.

There are different ways to control the amount of heating. One way is to use a feedback system, where the amount of heating is controlled by a loop that measures the temperature of the lens and—depending on the preset feedback parameters—the amount of heating is adjusted. Another way could be a feed-forward solution where one would need to know the thermal characteristics of the system, such as the thermal expansion and shrinkage transients for a certain laser power. This information could then be used to define the amount of heating as a function of time. Here, feedback is used. It has the advantage to also control and measure the temperature of the sample, which is particularly important for the calibration of the optical trap (see Section 8.4.4.2).

5.3.2. Laser heating and its effect

Opening the laser shutter heats up the objective lens. This was tested by successive opening and closing of the laser shutter and changing of the laser power. Figure 5.4A shows the temperature measured at the top of the objective. The transients showed fast initial and slow final exponential heating/cooling with time scales of about 30 s and 2000 s, respectively. The final temperatures in thermal equilibrium were extrapolated and showed a linear dependence to the applied laser power, with a temperature increase of 87 mK per percent laser power (Fig. 5.4A, inset).

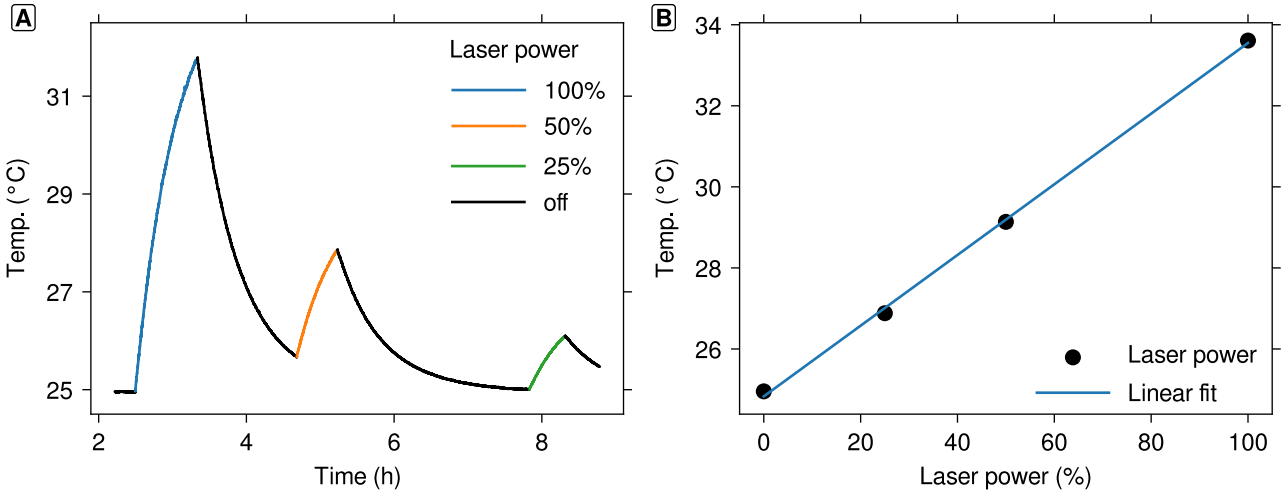

Fig. 5.4 | Laser heating effects. (A) Temperature transients measured at the top of the objective. The laser power was adjusted and the shutter opened and closed. The objective temperature followed a double-exponential transient. **(B)** Equilibrium temperature vs. laser power.

5.3.3. Implementation of a temperature feedback system

To stabilize the location of the focal plane, a temperature feedback system was implemented, similar to the one presented in Mahamdeh *et al.*, 2009 [34]. The system consists of heating

elements attached to the objective and the condenser and temperature sensors that measure the temperature of both optics.

5.3.3.1. Heating

To heat the objective and condenser lens, heating-foils were installed. The heating-foil at the objective is a $(2.5 \times 10.1)\,\mathrm{cm}^2$ self-adhesive foil with a resistance of $R_{\mathrm{obj}} = 22.3\,\Omega$ (Telemeter, Germany). The condenser holds two foils with the dimensions $(1.1 \times 9.9)\,\mathrm{cm}^2$ with a resistance of $R_{\mathrm{cond}} = 13.6\,\Omega$ (Minco, France), which are connected in series. The foils of the condenser and the one of the objective were connected to independent channels ($U_{\max} = 25\,\mathrm{V}$, $I_{\max} = 1\,\mathrm{A}$) of a power supply (E3631A, Agilent, Germany). Thus, the maximum heating powers are

$$P_{\mathrm{obj}}^{\max} = R_{\mathrm{obj}} I_{\max}^2 = 22.6\,\mathrm{W}$$

and

$$P_{\mathrm{cond}}^{\max} = U_{\max}^2 / R_{\mathrm{cond}} = 23.0\,\mathrm{W},$$

for the objective and condenser, respectively. To increase the efficiency of heating, the foils were additionally wrapped with silicone rubber tape, which reduces power loss through the air.

5.3.3.2. Temperature sensor installation

To control the amount of heating, the temperature of the objective and the condenser is measured. Temperature sensing is realized by PT-100 temperature sensors (1/3 DIN Class B, Omron, Germany). The sensors were connected to analog resistance-to-voltage converters (PXT-10, 24V DC, Brodersen Controls, Denmark). To avoid systematic errors, the sensors were connected via a 3-wire connection (Fig. 5.5). Because the temperature read out solely depends on a measured resistance, this connection scheme accounts for the internal resistance of the wires.

The converters are supplied with a constant 24 V DC voltage, which is provided by one output channel of the trapping laser power supply (Mean Well MN SP-500-24). The converters were installed inside the isolated room. This is necessary to avoid temperature fluctuations in the surrounding area influencing the voltage output of the converters.

The converter output voltage is read differentially through two analog input channels (*e.g.* AI0 and AI1 in Fig. 5.1). Differential measurement of the voltage provided by the converter is done to cancel out noise that was induced in the wire, *e.g.* by EM-radiation. Because these fluctuations occur in both wires, false signals cancel out when subtracting U_{AI1} from U_{AI0}. Both converter output channels (+V and −V) are floating, *i.e.* not referenced to ground. Without a reference, the provided voltage might drift and eventually reach the saturation voltage of the analog input channel. Therefore, a reference is given by connecting both channels with a 470 kΩ resistor to the analog input card ground. This resistance is about 100 times the internal resistance of the converter output [35].

5.3.3.3. Voltage to temperature conversion

The output voltage of the PXT-10 modules was measured by an analog input card (NI PXI-6221). The converters were operated to linearly convert a resistance of a PT100 element.

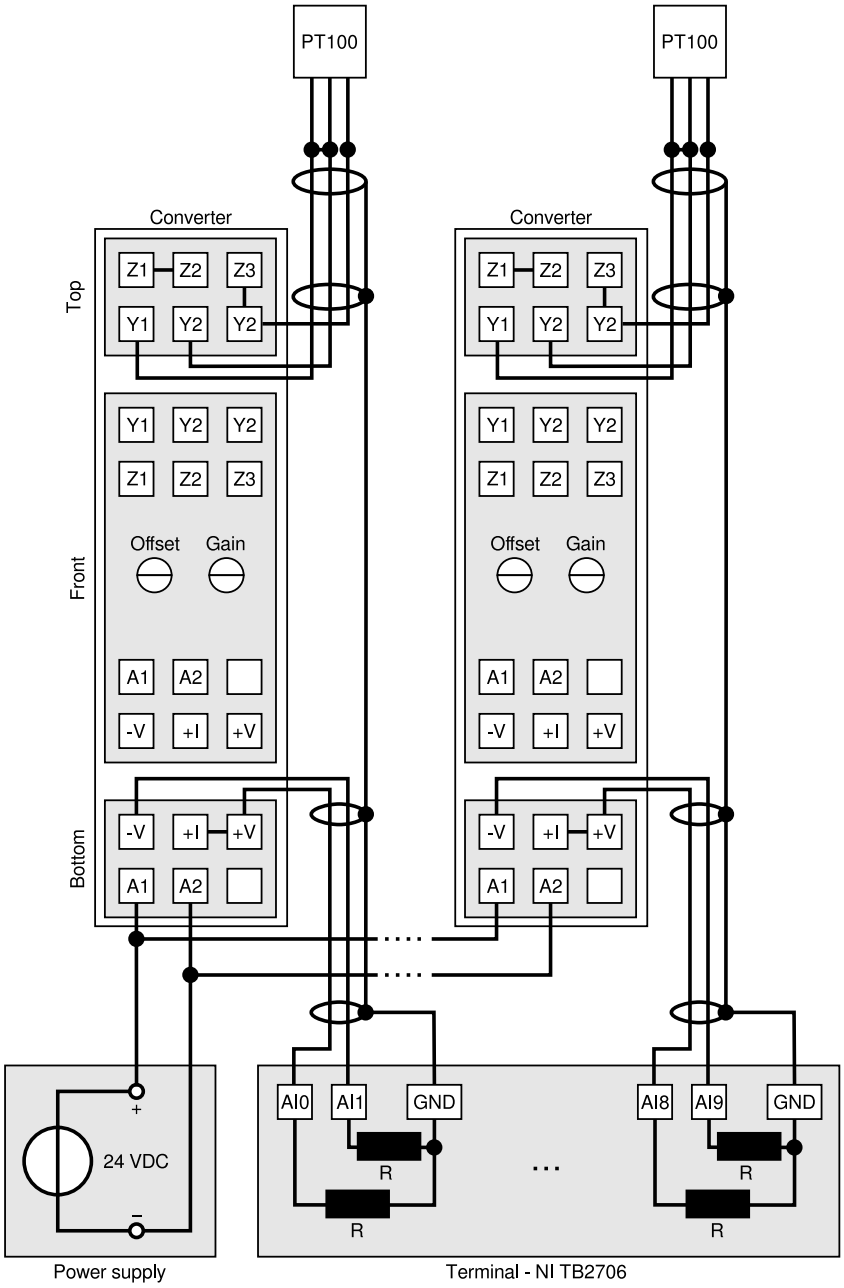

Fig. 5.5 | Temperature sensor wiring. The PT-100 temperature sensors are connected to the analog resistance-to-voltage converters through a three-wire configuration. The converters are powered by a DC power supply with 24 V. The analog output of each converter is differentially read through the National Instruments Terminal, which is connected to the NI PXI-6221 analog input card. This wiring scheme minimizes ground loops and false signal read-in.

Temperatures between −50 °C and 100 °C corresponded to a voltage between 0 V and 10 V:

$$U_{\text{out}} = I_{\text{out}} \left(R(T) - R_{-50} \right), \tag{5.3.1}$$

where R_{-50} is the PT100 resistance at $-50\,℃$. The resistance of a PT100 sensor at a given temperature can be described by the Callendar-van-Dusen (CvD) equation [36]:

$$R(T) = R_0 \left(1 + AT + BT^2 + (T - 100)CT^3\right), \tag{5.3.2}$$

The equation is valid for temperatures between $-200\,℃$ and $661\,℃$. The coefficients are

Table 5.6 | Coefficients of the Callendar-van-Dusen equation [36].

Coefficient	Value
R_0 (Ω)	100.0
A ($℃^{-1}$)	3.911×10^{-3}
B ($℃^{-2}$)	-5.782×10^{-7}
C ($℃^{-4}$)	-1.083×10^{-11}

given in Fig. 5.6. Setting $C = 0$ reduces the temperature range to $0 - 660\,℃$, which was fine for this purpose. Solving Eq. (5.3.1) together with Eq. (5.3.2) for the temperature gives

$$T(U) = -\frac{A}{2B} - \sqrt{\left(\frac{A}{2B}\right)^2 - \frac{1}{B}\left(1 - \frac{I_{\text{out}}R_{-50} + U}{I_{\text{out}}R_0}\right)}. \tag{5.3.3}$$

The output current I_{out} in Eq. (5.3.1), can be determined by

$$I_{\text{out}} = \frac{\Delta U}{R_{100} - R_{-50}} = \frac{10\,\text{V}}{138.5\,\Omega - 80.6\,\Omega} = 173\,\text{mA}.$$

5.3.3.4. Calibration of the temperature sensors

Because the output voltage provided by the converts is subject to changes in temperature and possibly uncertainties during the manufacturing and electronics, the output voltage offset and gain can be adjusted (Fig. 5.5). Thus the output voltage is

$$U_{\text{out}} = U_{\text{off}} + aRI_{\text{out}}. \tag{5.3.4}$$

One possible procedure to calibrate the sensors is to use two precisely known temperatures as a standard and adjust the offset voltage, U_{off}, and gain, a, of the converter to give the right reading. These are, for example, the melting and boiling temperature of pure water. However, this procedure is tedious, cumbersome and prone to error: the controllers need to be adjusted many times to approach the right values, a lot of equipment is needed (heater to boil water, ice water, stirrer), temperature gradients exist in the water, especially when boiling, and the cable insulation is affected by the hot water.

A much easier way was to use high-precision resistors as standards. Resistors are commercially available as a low tolerance type. To adjust the converter controllers, 0.1% tolerance resistors were used with the following resistances: $82\,\Omega$, $100\,\Omega$ and $120\,\Omega$ (Vishay Beyschlag, Germany). These corresponded to temperatures of, respectively, $-45.73\,℃$, $0.00\,℃$ and $51.57\,℃$[7]. To calibrate the converters, the PT100 sensors were replaced by the resistors.

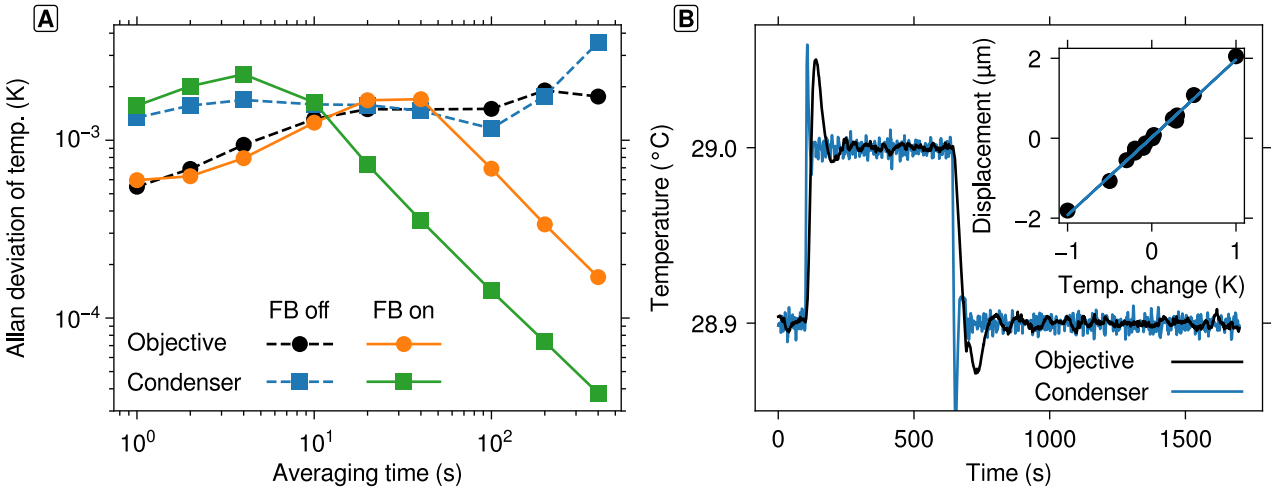

Fig. 5.7 | Temperature feedback performance. (A) Allan deviation-plots of the objective and condenser temperature with feedback and without. Both measurements were done after equilibration of the system. **(B)** Temperature step-response to a change of the setpoint of the objective and the condenser. Inset: Focal plane displacements vs. temperature change.

The lowest resistor was used to adjust the offset voltage such that the measured temperature matched the calculated one. Similarly, the highest resistor was used to adjust the gain of the converter. To check if the resistance-to-temperature conversion worked correctly, the 100 Ω resistor was used. The procedure was repeated until the temperature was correct. This routine should give an error of about 0.3% on the absolute temperature measurement, *i.e.* ≈ 1 K. To keep the systematic error as low as possible one should calibrate when the system is thermally equilibrated, *i.e.* the temperature of the room should be close to the operating temperature.

During experiments, temperature changes are more relevant for the stability and precision of the measurements. These changes can be minimized by using a feedback system.

5.3.3.5. Feedback control

The temperature is monitored by a VI that continuously measures the voltage input and converts the voltage according to Eq. (5.3.3). A previously developed feedback VI then used the measured temperature to calculate a control signal according to a PID-feedback control scheme. After optimizing the PID-parameters using the Ziegler-Nichols-Method [37], the feedback system was used to heat up the objective and the condenser to 29 °C.

The feedback-control of the temperature increased the long-term temperature stability compared to the temperature without active control. The Allan deviation plots (Fig. 5.7A) of the temperatures of the objective and condenser showed—after a long-term equilibration procedure—slopes typical for pink noise for a range between seconds and hundreds of seconds.

[7] The resistances are specified at room temperature. In general the resistance of a resistor is temperature depended. Its dependency is specified by the temperature coefficient. The used metal film resistors have a very low temperature coefficient of $25 \cdot 10^{-}6\,\mathrm{K}^{-1}$. A temperature correction of the resistance was therefore neglected.

The temperatures fluctuated around $1 - 2\,\mathrm{mK}$. With the feedback-control enabled, the temperatures fluctuated at the same level for short times and decreased with averaging times, $\tau > 40\,\mathrm{s}$, for the objective, and $\tau > 4\,\mathrm{s}$, for the condenser. Note that the slope is proportional to τ^{-1}, which corresponds to white or flicker phase noise (regarding the Allan deviation-plot see also Section 6.2.3) [38]. Without feedback control, the equilibration of the instrument would take an immense amount of time worsening experimental conditions.

5.3.4. Temperature setpoint displaces the focal plane axially

Heating the objective leads to an effective change of the position of its focal plane. To determine the focal plane drift of the objective, the setpoint of the temperature feedback was successively changed (Fig. 5.7B). A previously focused sample drifted out of focus. The de-focusing was compensated by a corresponding movement of the stage (Fig. 5.7B, inset). The heating of the objective effectively moved the focal plane by $(1.94 \pm 0.05)\,\mathrm{nm/mK}$. Compared to the preceding optical tweezers setup (Ref. [20]), this relation was twice as large. One reason for this could be material differences between the objectives. Extrapolating these relations results in a displacement of about $15.5\,\mu\mathrm{m}$, if the laser was operated at 100 % of its power.

Part III.

Performance

6. Background

Characterizing the performance of an optical trap is a non-trivial task. "Performance" is on the one hand depending on the stability of individual components and devices, but it also depends to a great extent on the minimization of disturbances caused by drift and external noise. Once minimized, performance is expressed in terms of stability and achievable precision.

6.1. Sources of noise

Stability is a term often used to underline a systems performance. High stability suggests an instrument that could be used for measurements with a minimum of disturbance. In the case of optical tweezers, disturbances are drift and noise.

Drift usually entitles slow changes in the position of an entity, *e.g.* the sample chamber, the focal plane of the objective or the position of the optical trap. Drift is mostly caused by transient temperature changes, as it is the case when the instrument warms up or cools down. For example, the door of the lab was opened and cold air enters the lab, or the laser shutter was opened and lenses and mechanical components warm up due to absorption. These temperature changes lead to thermal expansion or shrinkage of optical or mechanical components. Depending on the point of view, drift can also be thought of as a type of low-frequency noise. In the power spectrum, P, this noise shows up with a scaling $P(f) \propto f^{-2}$.

Noise is a term used for any kind of disturbance, which is mostly stochastic in nature and affect the signals to be measured. In optical tweezers, these signals are usually the position signals of a trapped particle. The bandwidth of these signals typically goes up to tens of kilohertz. Thus, noise sources within this band must be reduced to improve the system's performance.

There are different types of noise. On the one hand there is thermal noise, caused by the Brownian motion of the trapped particle. Thermal noise forms the base and fundamental noise that cannot be overcome for a given experiment. On the other hand there is external noise, which must be minimized to increase the instrument precision. External noise typically falls into one of the following categories:

- **Mechanical noise** usually is low frequency noise ($< 10\,\mathrm{Hz}$), which is transmitted through the building and coupled into the instrument through the floor. It is typically caused by traffic, construction sites, elevators, steps, wind, waves, the user, *etc.*
- **Acoustic noise**, typically in the spectral range of tens of hertz up to a couple of hundred hertz, is transmitted through the air and coupled into the instrument. Acoustic noise is, for example, caused by fans, ventilation, pumps, *etc.* Moreover, convection, *e.g.* caused by heating of air within a laser focus, can lead to fluctuations in the refractive index of air and would, thus, cause changes in the optical path.

- **Electronic noise** is typically characterized by one or more sharp peaks in the power spectrum. Electronic noise can be found in a broad spectral range. A prominent example of electronic noise is ground-loop noise[8], which causes a sharp peak at the power line frequency, *i.e.* 50 Hz (or 60 Hz in parts of the Americas and Asia). Other electronic noise can, for example, be the result of resonances within the electronic circuits.

To enhance the performance of an instrument all sources of external noise must be minimized. In general, mechanical noise is reduced by choosing a location for the instrument with low noise, *e.g.* the basement. Further isolation from vibrational noise is achieved by placing the instrument on floor slabs that are disconnected from the building base plate. Remaining vibration can be reduced by heavy tables and stands, which inherently attenuate vibrations on the table due to their inertia. Furthermore, an optical table made for high stability should be chosen. To isolate the instrument from remaining vibrations an active or passive vibration isolation system should be installed [39–41].

Acoustic noise can effectively be reduced by placing the instrument in a separate closable room. Noisy equipment, such as fans, inside that room and especially on the optical table should be avoided. Moreover, the instrument should be enclosed in an isolating case. Usage of acoustic foam isolates to an extent from both, temperature changes and acoustic noise.

Electrical noise, especially ground loops must be avoided by following a star-like ground connection scheme and placing power supplies far away from data acquisition devices. Following this scheme does not guarantee a full reduction of power line noise, since electronic devices at times inherently show ground loop problems.

However, identifying the types of noise and their sources is often non-trivial. Power spectral density plots of, for example, position signals of a trapped microsphere, stage monitor signals, *etc.*, can help with the identification of the types of noise. Each type typically has a characteristic frequency band. To judge whether a disturbance and to which extent external noise compromises the precision of the instrument, Allan deviation plots help in pointing out the time scale and magnitude of it. For example, a slow drift of a few tens of nanometers in the trap z-position might disturb long term experiments, but will not have a tremendous effect on experiments where the interaction of, *e.g.* proteins, is taking place within milliseconds. Nonetheless, the reduction of noise is the important task to enhance the overall precision of the instrument.

6.2. Resolution vs. precision

The terms resolution and precision are at times used interchangeably in contexts that aim to describe the performance of an instrument [34, 42]. However, there is an important but subtle difference between the two terms. It is advisable to distinguish the two terms and use it with care to avoid confusion and misunderstanding.

[8] Ground-loop noise emerges if electric components or devices, which are powered by the main power line, are connected to the main ground via more than one connection. The different connections to ground form a conductive loop. A voltage and, thus, a current is induced by EM-fields created by transformers at the power line frequency. Ground-loops can be avoided by referencing a circuit to ground, only once.

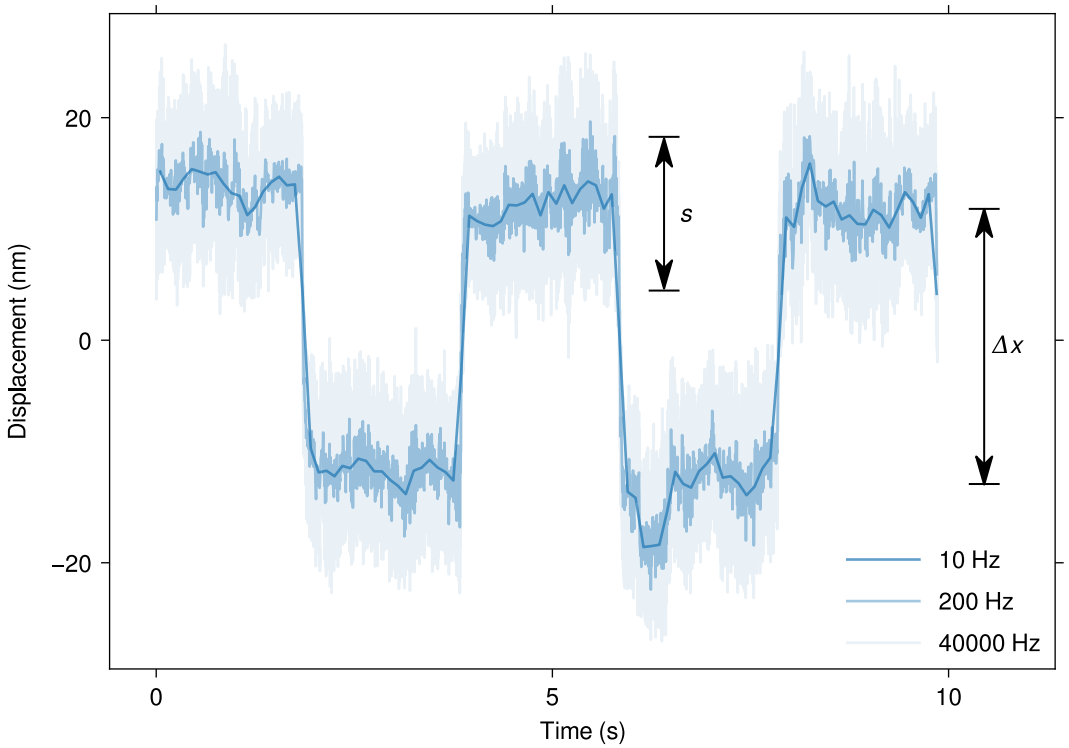

Fig. 6.1 | Resolution of steps with respect to the SNR. The displacement of an immobilized mircosphere from the trap center is plotted against time. The particle was displaced by $\Delta x = 25\,\text{nm}$ using the piezo translation stage. The displacement was recorded at 40 kHz and then down sampled by block averaging to 200 Hz, and 10 Hz. The quality of resolving this step size depends on the noise associated with the signal. Depending on the amount of averaging the resolution of the 25 nm steps changes from a SNR of 5.1 at 40 kHz to 6.2 and 11.9 at 200 Hz and 10 Hz, respectively.

6.2.1. Resolution

Resolution describes the smallest change in a quantity being measured that causes a perceptible change [43]. Thus, it describes the ability to distinguish two measurements from each other. The distinguishability is a rather vague definition, because it needs some kind of minimal measure, *i.e.* a minimal difference between two quantities, to state their distinctness. This minimal difference is a somewhat arbitrary choice. Often, resolution is specified by one quantity, *e.g.* 10 nm. However, the quantity itself does not give any information about the confidence of the distinctness, nor does it provide information about the level of noise underlying the data.

Providing the signal-to-noise ratio (SNR) or the underlying variance of the signal, additionally, puts the value into a more meaningful context. In this context, the SNR is the ratio between the minimal resolvable step and the underlying noise. The noise of the data is the standard deviation, $\bar{s}$, of the data points, x_i, before and after a step in the signal [14]. Consequently,

$$\bar{s} = \sqrt{s^2_{\text{before}} + s^2_{\text{after}}}, \tag{6.2.1}$$

where $s = \sum_i (x_i - \bar{x})^2/(n-1)$ is the sample standard deviation, s^2 is the sample variance and $\bar{x} = \sum_i x_i/n$ is the sample mean.

Thus, a resolution of 10 nm with $SNR = 1$ intuitively has less confidence in the measured difference than a SNR that corresponded to the Rose criterion[9], *i.e.* $SNR = 5$. Hence, a 10 nm resolution with a $SNR = 5$, would imply a noise level of only 2 nm as opposed to 10 nm for a SNR of unity. In Fig. 6.1, 25 nm steps of a microsphere are shown. The quality of the step resolution increases upon averaging, because the standard deviation on the plateaus decrease. Thus, averaging effectively decreases the bandwidth of the signal. This can only be compensated by increasing the measurement time, *i.e.* measuring for longer periods of time, which has limitations in practice that will be discussed in Section 6.2.3. The standard deviation of the data signal within one plateau, s, is related to the precision that is associated with the measured data points.

6.2.2. Precision

Precision describes the certainty of a measured quantity [43]. Therefore, precision is inversely related to the error bar of a quantity . In contrast to resolution, precision[10] is not related to another measurement, it is related to the statistical variation of the measured quantity, *e.g.* the mean position, and, therefore, the confidence of that value. It can be described by the experimental standard deviation of the mean (SDM)[11]:

$$s_{\bar{x}} = s/\sqrt{n}. \tag{6.2.2}$$

Equation (6.2.2) estimates the standard deviation of an averaged quantity, and, thus, the precision. However, it could also be determined experimentally by measuring a set of sample means, $\bar{x}_i$, and determining their standard deviation, because the definition of the SDM is

$$s_{\bar{x}} = \sqrt{\mathrm{var}(\bar{x}_i)} = \sqrt{\langle (\bar{x}_i - \langle < \bar{x}_i \rangle)^2 \rangle}. \tag{6.2.3}$$

6.2.3. Highest achievable precision

Precision is a function of time. Naively, one could think it can be increased to an arbitrary magnitude, since $s_{\bar{x}}$ (Eq. (6.2.2)) decreases with $\sqrt{n}$: increasing the number of measurements should therefore increase the precision accordingly. In practice, however, this is not the case,

[9] A SNR of 5 was proposed by Albert Rose and is also known as the Rose criterion [44]. The Rose criterion asks for a SNR of 5, to reduce the number of false-positive events to practical zero. This can be seen if one considers a normally distributed random process. The probability to measure a value that lies more than 5 standard deviations away from the mean is about $\approx 6 \cdot 10^{-7}$.

[10] Additionally, precision must not be confused with accuracy. In contrast to the statistical variation, accuracy describes systematic errors. The *Guide to the expression of uncertainty and measurement (GUM)* states: "accuracy of measurement: closeness of the agreement between the result of a measurement and a true value of the measurand" [45].

[11] Further, the *GUM* notes that the "experimental standard deviation of the mean is sometimes incorrectly called standard error of the mean" (SEM) [45]. However, it does not give a particular reason for the distinction. An explanation could be that the SDM is related to the sample standard deviation, s, and the SEM is related to the population standard deviation, σ, which is usually unknown.

because measurements are subject to different types of noise and drift (as discussed above). Both disturbances compromise the measurement at different timescales and, thus, limit the achievable precision. Hence, there should be an optimum timescale, *i.e.* averaging time, at which averaging a signal reduces the error bar the most, resulting in the highest achievable precision.

The precision for an averaging time, τ, can be determined by the Allan deviation (ADEV). The ADEV can be calculated from a time-dependent signal, $x(t)$, of length t_{msr}. It is defined as the square-root of the Allan variance, $AVAR$:

$$\begin{aligned} ADEV(\tau) &= \sqrt{AVAR(\tau)} \\ &= \sqrt{\frac{1}{2}\langle(\bar{x}_{\tau,i+1} - \bar{x}_{\tau,i})^2\rangle}. \end{aligned} \tag{6.2.4}$$

A signal, sampled at sampling frequency f_{sample}, is separated into sets of equal length, τ. The mean of the signal of the i-th window is

$$\bar{x}_{\tau,i} = \frac{1}{n}\sum_{j=1}^{n} x_{n(i-1)+j}$$

and contains $n = \tau f_{\mathrm{sample}}$ data points. For a particular τ there is a set of $m = \lfloor t_{\mathrm{msr}}/\tau \rfloor = \lfloor N/n \rfloor$ non-overlapping windows. Here, $\lfloor\cdot\rfloor$ refers to the *floor*-function.

To make more use of the information in the data and increase the confidence in the estimates, the overlapping Allan deviation is commonly used and has become a standard to investigate frequency stability [38]. Instead of moving the adjacent window by n data points, it is moved by only one data point, leading to a number of $m = N - n + 1$ windows. All calculations in this thesis were done using the overlapping scheme.

The ADEV for a particular time, τ, estimates the mean distance between adjacent means and, therefore, gives an estimate of the experimental SDM of an averaged time series. Determining the SDM for a particular averaging time could also be done using Eq. (6.2.3), but, in practice, is prone to overestimate the SDM for a single measurement. This overestimate arises because the SDM also includes the covariance between the adjacent windows. The ADEV accounts for this covariance, which can be seen by expanding Eq. (6.2.4) and using $\langle\bar{x}^2_{\tau,i}\rangle = \langle\bar{x}^2_{\tau,i+1}\rangle = \langle\bar{x}^2_{\tau}\rangle$:

$$ADEV(\tau) = \sqrt{\langle\bar{x}^2_{\tau}\rangle - \langle\bar{x}_{\tau,i+1}\bar{x}_{\tau,i}\rangle}. \tag{6.2.5}$$

The ADEV can also be used to identify different types of noise. The ADEV is commonly log-log-plotted with respect to the averaging time. The slopes of such plots gives information about the dominant noise within a range of time scales [38, 46].

To compare how the Allan deviation performs with respect to different types of noise and drift, the following signals were simulated[12]: (i) pure white noise, (ii) low-pass filtered white noise resulting in a Lorentzian-shaped PSD, (iii) pink-noise ($\propto f^{-1}$) and (iv) linear drift which was superimposed onto the low-pass filtered data (ii) (Fig. 6.2A). Their power spectra and Allan deviations are plotted in Fig. 6.2B and C, respectively. For comparison, also the SDM is plotted using Eq. (6.2.3).

[12]The simulated signals were done for a trapped bead in water. The microsphere diameter was set to $d = 590\,\mathrm{nm}$ and the temperature to $29\,^{\circ}\mathrm{C}$, which resulted in a drag coefficient of about $4.5\,\mathrm{nN\,s/m}$. The trap stiffness was set to $\kappa = 0.03\,\mathrm{pN/nm}$, which resulted in a corner frequency of $\approx 1\,\mathrm{kHz}$.

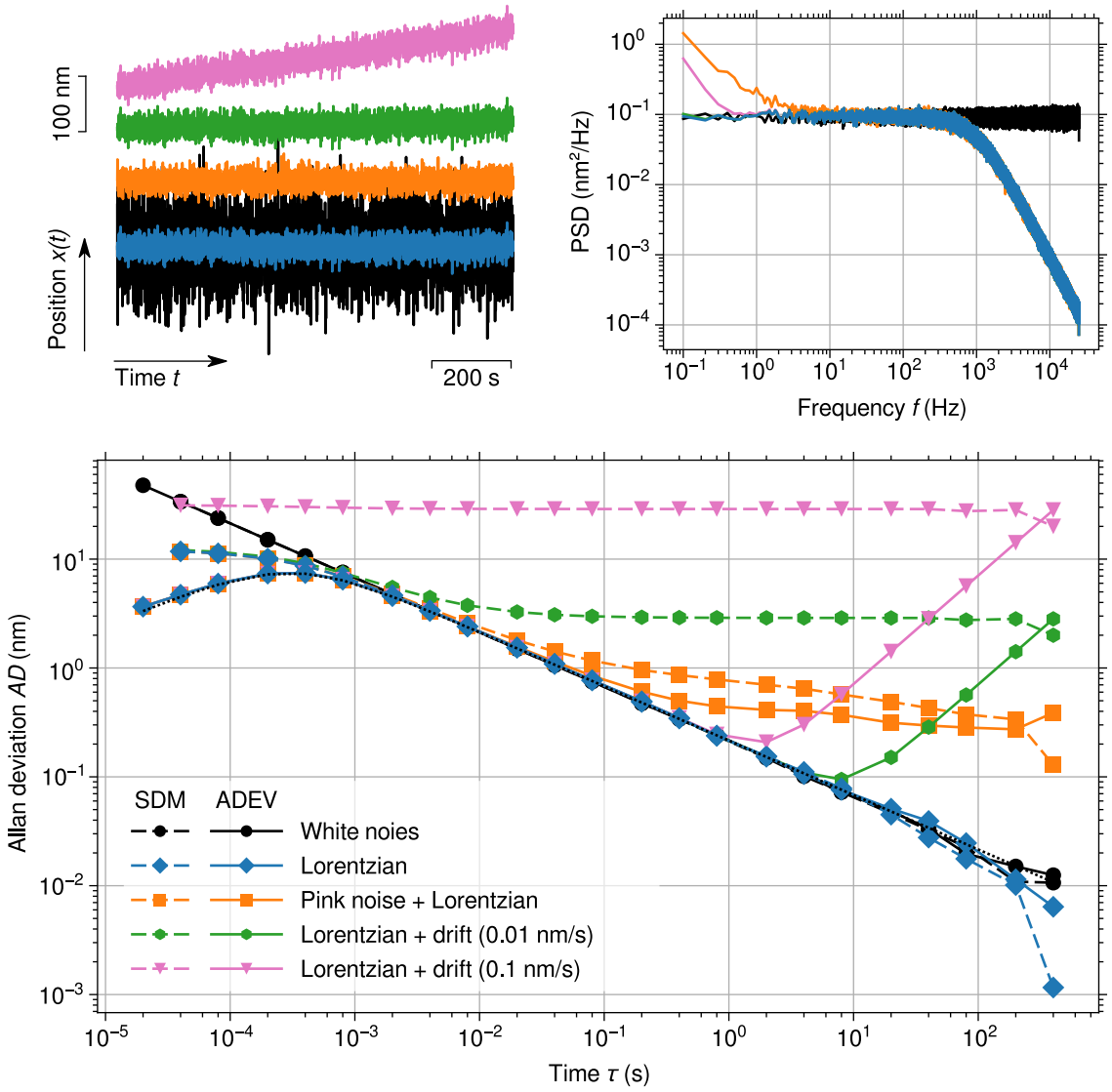

Fig. 6.2 | Noise and drift compromise precision. (A) Monte Carlo simulations of pure white noise (black lines) and position signals a trapped microsphere without any external noise (blue lines) and signals that are subject to pink noise (orange) and drift of 0.01 nm/s (green) and 0.1 nm/s (magenta). **(B)** Power spectra of the signals shown in (A). **(C)** Allan deviation and SDM vs. τ of the time traces shown in (A). Also plotted is the theoretical ADEV of a damped harmonic oscillator (Eq. (6.2.6)) (black dotted line) for the given parameters.

Purely random, *i.e.* independent, data shows white noise (black lines). Its power-spectrum (Fig. 6.2B) shows the characteristic independence of frequency, f. The ADEV of white noise decreases with $\tau^{-1/2}$. As well does the SDM, because the data is uncorrelated. White noise can efficiently be averaged over all time scales.

The position signal of a particle that is subject to Brownian motion and trapped in a harmonic well shows a Lorentzian-shaped power spectral density[13]. A Lorentzian is characterized by its cut-off- (or corner-) frequency, f_c. Physically the corner frequency characterizes the response time, $\tau_c = 1/f_c = 2\pi\gamma/\kappa$ of the particle, which depends on the particle's drag,

γ, within the fluid and the strength of the optical trap, κ. For short timescales the particle's response to a fluctuation is independent of the optical trap. Thus the particle shows typical Brownian motion (Brown noise), which is characterized by $P(f) \propto f^{-2}$ and $ADEV \propto \tau^{1/2}$ (blue lines in Fig. 6.2). For long timescales $t \gg \tau_c$ the trap restricts Brownian motion; the positions are independent of each other, which is reflected in the constant plateau in the PSD for $f \ll f_c$. The ADEV of such a signal is analytically given by (black dotted line in Fig. 6.2) [47, 48]:

$$ADEV(\tau) = \sqrt{\frac{2\mathrm{k_B}T\gamma}{\kappa^2\tau}\left(1 + 2\frac{\gamma}{\kappa\tau}e^{-\frac{\kappa\tau}{\gamma}} - \frac{1}{2}\frac{\gamma}{\kappa\tau}e^{-\frac{2\kappa\tau}{\gamma}} - \frac{3}{2}\frac{\gamma}{\kappa\tau}\right)}. \tag{6.2.6}$$

The ADEV shows the typical decrease proportional to $\tau^{-1/2}$ for $\tau \gg \tau_c$. This region is also referred to as the thermal limit. One can also deduce the thermal limit from Eq. (6.2.6) for $\tau \gg \gamma/\kappa$ the ADEV becomes

$$ADEV_{\mathrm{thermal}}(\tau) = \sqrt{\frac{2\mathrm{k_B}T\gamma}{\kappa^2\tau}}. \tag{6.2.7}$$

The maximum is at $\tau_{\max} = 1.89 \times \gamma/\kappa$ [47]. For $\tau < \tau_{\max}$, averaging increases the ADEV, since one is only measuring Brownian motion at these time scales. Here, adjacent data points are correlated. Thus, sampling a position signal at a sampling frequency higher than $1/\tau_{\max}$ is, therefore, not beneficial. Therefore, a choice of $\Delta t = 2\tau_c = 2\gamma/\kappa$ as a time limit to consider data points as uncorrelated is reasonable (comp. Section 3.1.1. in Ref. [49]).

Pink noise sets an upper limit to the achievable precision. Typical position measurements on real setups experience pink noise, which shows a $= 1/f$ dependence in the power spectrum at low frequencies. In ADEV-plots, pink noise appears as a constant ($\propto \tau^0$). The simulated signal (orange lines) therefore reaches a global minimum at about 1 s.

Drift causes an increase in ADEV at long timescales. Drift was simulated with 0.01 nm/s (green lines) and 0.1 nm/s (magenta lines). The slow drift was not identifiable in the PSD-plots, because the signal is dominated by the noise at the lowest frequency $f = 0.1$ Hz. However, both drifts show up in the ADEV plots. Because drift constantly changes the mean and the variance of an averaged signal at increasing τ, the ADEV shows drift as being proportional to τ. Drift superimposes on the $\tau^{-1/2}$ decrease of the ADEV at the thermal limit and, therefore creates a minimum. In experiments, the magnitude of pink noise is fixed, therefore, the minimum depends on the response time of the trapped microsphere and is proportional to $\sqrt{\gamma}/\kappa$, as one can see from Eq. (6.2.7).

In conclusion, one can determine the achievable precision of a measurand by the ADEV. It intuitively gives information about possible sources of noise and the optimum averaging time. One could utilize this information to design experiments according to this optimum averaging time. For example, one could adjust the stepping rate of a molecular motor by changing the concentration of ATP and, therefore, would be able to down-sample the position signal of the motor by averaging. Doing so would decrease the SD of the averaged signal and, thus, increase the step-resolution.

[13] However, a PSD with a frequency resolution of $\Delta f = 1$ mHz would also identify the linear drift. Though, for an averaged PSD with $N = 100$ (comp. Eq. (8.4.5)), 10^5 s ≈ 28 h would be needed.

7. Results

7.1. Vibration isolation

Reduction of mechanical noise is necessary to achieve high-precision measurements. As stated in Chapter 3, the instrument is build on an optical table that is mounted on an active vibration isolation system (VarioBasic-60, Accurion, Germany), which intends to reduce the mechanical vibrations on the table and, therefore, decrease position fluctuations of the whole setup.

Mechanical vibration can be measured as acceleration. Although vibrations are displacements in a narrower sense, measuring vibration in terms of acceleration does serve to interpret the data as a normalized force. Vibrational forces are in a wider sense the cause for vibrating parts, such as lenses, sample holders, *etc*. In a very simplistic approach, the actual displacement of one part of mass m_{part} can be calculated from its particular acceleration $a = a_{\mathrm{msr}} m_{\mathrm{s}}/m_{\mathrm{part}}$, where a_{msr} is the measured acceleration, m_{s} is the mass of the measurement device, which is specified as 0.49 kg [50]. Integration over time would then lead to the displacement. However, to compare the influence of mechanical noise reduction, the pure acceleration measurement is sufficient.

The active vibration isolation system reduced the mechanical noise on the optical table. Because the instrument is located in a laboratory space in the basement of the building (2^{nd}floor underground), and is, furthermore, isolated from external mechanical vibrations by special contructional means, such as a de-coupled base plate, vibration isolation foam, *etc*. (presented in Hermsdorf *et al*., 2018 [41]), the overall vibration level can be considered to be already low, compared to normal lab conditions.

The installed—but not operational—vibration isolation system increased level of low frequency amplitudes. This was due to resonances occurring in the range of (3–12) Hz. However, when active, the vibration isolation system amended these and reduced vibrations upto ≈ 30 Hz (Fig. 7.1A). The ADEV plots also show increased vibrations for timescales larger than 10 ms, when comparing the floor signals with the deactivated vibration isolation system data (Fig. 7.1B). However, when the vibration isolation system was in operation, the overall acceleration could be reduced by one order of magnitude. The power spectra show decreased acceleration up to about 20 Hz.

7.2. Stability of the trapping laser

The trapping laser is one of the key parts of an optical tweezers setup. In addition to the mechanical stability of an optical tweezers setup (see Section 6.1), the stability of a trap also depends on the stability of the trapping laser. Laser stability can be characterized by the pointing stability.

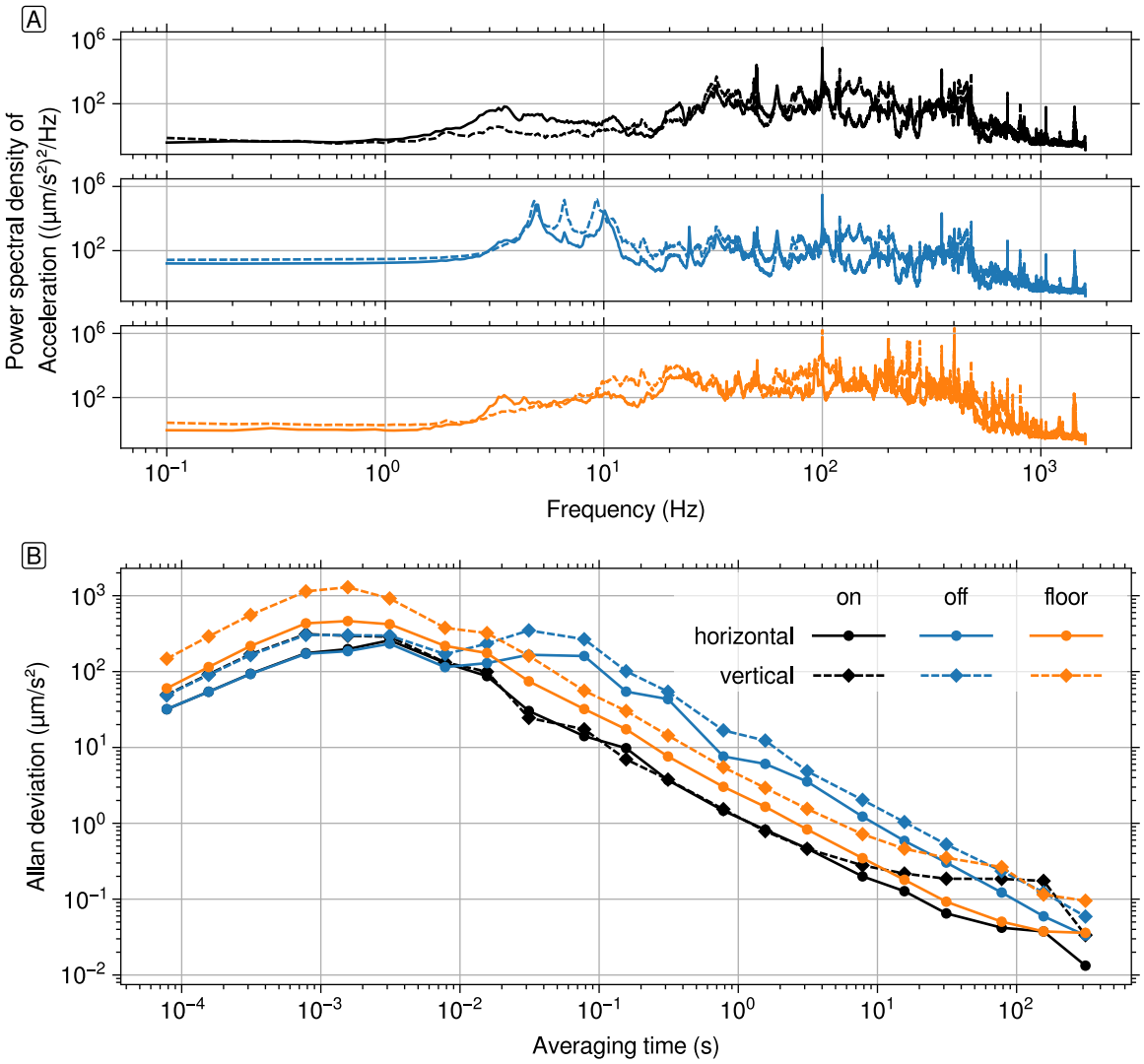

Fig. 7.1 | Reduction of mechanical noise by an active vibration isolation system. (A) Power spectral density of the acceleration vs. frequency. Acceleration measurements comparing the vibrational noise on the floor of the isolated room (bottom), and on the optical table with the active VI system switched off (middle) and on (top). The VI system increases the noise. Mechanical resonances occur in the range of (3–12) Hz. **(B)** Allan deviation plot of the acceleration. The VI system reduces the total mechanical noise by on order of magnitude, compared to the measurements where the system was switched off.

The pointing stability can be measured with a position sensitive device, such as a quadrant photodiode (QPD). The laser is—after sufficient attenuation via a silver mirror ($T \approx 0.2\%$) — pointed on a QPD without passing any additional optics. The QPD measures the position and the power of the laser over time. After calibration of the QPD[14], the position is related to the distance between the laser and the QPD. Thus, the pointing stability is measured in radians.

[14]The QPD was calibrated by mounting it on a xy-translation stage. Defined turns of the stage's metric

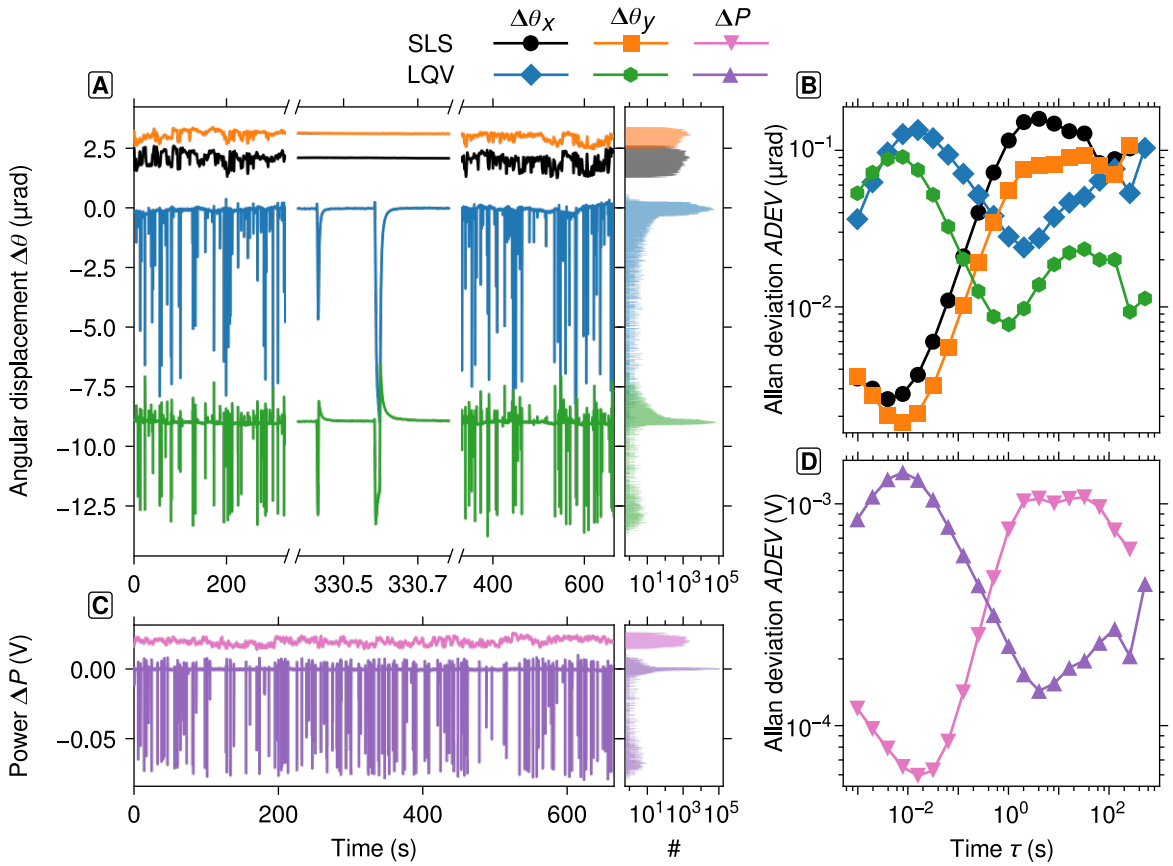

Fig. 7.2 | Pointing and power stability measurements of two trapping lasers. Compared were a Smart Laser Systems Nd:VO_4 1064 nm (SLS) and a Laser Quantum Ventus (LQV) 1064 nm laser. **(A)** Angular displacements in x- and y-axis vs. time (left) and their histograms (right). **(B)** Allan deviation plot of the angular displacements of both lasers in the x- and y-axis. **(C)** Power fluctuations around the mean power vs. time. **(D)** Allan deviation plot of the laser power of both lasers. The data in shown in (A) and (C) is shifted vertically for clarity.

Two lasers were compared with respect to their pointing and power stability (see Fig. 7.2). A diode-pumped solid state laser (Smart Laser Systems, Germany), SLS Nd:YVO_4, with 3 W output at 1064 nm and a solid state laser (Laser Quantum, England), LQ Ventus 1064, with 5 W output. Both lasers were allowed to equilibrate for more than 10 hours in an isolated room at ambient temperature. The angular displacement signal, $\Delta\theta(t)$ was acquired at 1 kHz for a period of about 650 s (Fig. 7.2A). The SLS laser showed fluctuations with a narrow distribution around the mean position, compared to the LQV laser. The total standard deviations in the x- and y-axis, respectively, were 0.29 µrad and 0.20 µrad for the SLS laser and 0.20 µrad and 0.13 µrad for the LQV laser.

Although both lasers showed comparable pointing stabilities in both axes, the LQV laser showed sharp spikes with amplitudes of up to 35× the standard deviation. The QPD sum-

screws with a defined pitch then translated the QPD and, thus, the laser position on it. The measured positions of the laser center (in volts) were then related to the respective translations. The slope of the correlation between the two quantities then gave the calibration factor.

signal is a measure of laser power (though uncalibrated). The power fluctuations of both lasers showed equal standard deviations of 0.29 mW. Although, both lasers nominally performed similarly stable, the LQV showed spikes with high amplitudes (Fig. 7.2B). The Allan deviation plots of the angular displacements and power deviations show at what timescales these fluctuations occurred (Fig. 7.2B, D). Whereas the SLS laser was generally more stable at timescales $\tau \ll 1\,\mathrm{s}$ (*e.g.* $ADEV_y \approx 2 \times 10^{-3}$ µrad at $\tau = 10\,\mathrm{ms}$), the LQV laser reached $ADEV_y \approx 10^{-2}\,\mu\mathrm{rad}$ at $\tau = 1\,\mathrm{s}$ in the y-axis, which had slightly less variations than the x-axis. For averaging times $\tau > 1\,\mathrm{s}$, the LQV laser reached almost one order of magnitude smaller Allan deviations than the SLS laser. The Allan deviation of the power fluctuations showed similar behavior.

Fluctuations of the laser position adds up to the position noise of a trapped particle. Considering the optical design of the trapping laser, the measured fluctuations are transferred into the sample by a factor $k = f_{\mathrm{Obj}}/(M_1 M_3) = 0.27\,\mathrm{mm}$, where $f_{\mathrm{Obj}} = 3.33\,\mathrm{mm}$ is the focal length of the objective, $M_1 = 7$ is the magnification of the 3-lens-telescope, and $M_3 = \frac{140\,\mathrm{mm}}{80\,\mathrm{mm}} = 1.75$. Hence, the position fluctuations of the lasers would correspond to $\Delta x = \Delta\theta \times k < 1\,\text{Å}$. This lies below the achievable precisions discussed in Section 7.3, below. In practice, however, the fluctuations could be larger, due to a longer optical path length. The pointing stability measurements were done with a distance of $\approx 0.5\,\mathrm{m}$ between the laser and the QPD. The actual optical path length is about 1.1 m, which could result in larger fluctuations due to convection of air.

7.3. Stability of the optical trap

To determine the performance of the optical trap, a polystyrene microsphere with a diameter of 590 nm was trapped, calibrated by active PSD analysis and its displacement within the trap was recorded for about 20 min (Fig. 7.3, inset). The calculated ADEV (solid lines in Fig. 7.3) showed a transient characteristic for a damped harmonic oscillator that is subject to drift (see Section 6.2.3). The ADEV of all three axes decreased proportional to $\tau^{-1/2}$ up to $\tau \approx 0.6\,\mathrm{s}$ where it reached a mean precision of about 2 Å in the x- and y- and about 4 Å in the z-axis. For longer averaging times the ADEV showed a gradient proportional to τ, which is typical for drift. From Eq. (6.2.7) one can see that the ADEV is inversely proportional to the trap stiffness. Thus, a stronger trap can push the achievable precision further down below 1 Å, but will result in a proportionally smaller displacement, keeping the achievable SNR constant:

$$SNR = \frac{x}{\Delta x} = \frac{F}{\sqrt{\frac{2k_B T\gamma}{\tau}}}. \tag{7.3.1}$$

The only way of increasing the SNR would, hence, be, to decrease the drag coefficient—either by the use of smaller sized microspheres or by a less viscous medium—or to increase the averaging time τ, which would, in turn, make a reduction of the drift and pink-noise necessary.

The thermal limit for force measurements is independent of the trap stiffness, as one can see when multiplying Eq. (6.2.7) by κ. The calibration of the trapped microsphere yielded trap stiffnesses of $\{\kappa_x, \kappa_y, \kappa_z\} = \{0.05, 0.06, 0.02\}\,\mathrm{pN/nm}$, which, corresponds to an

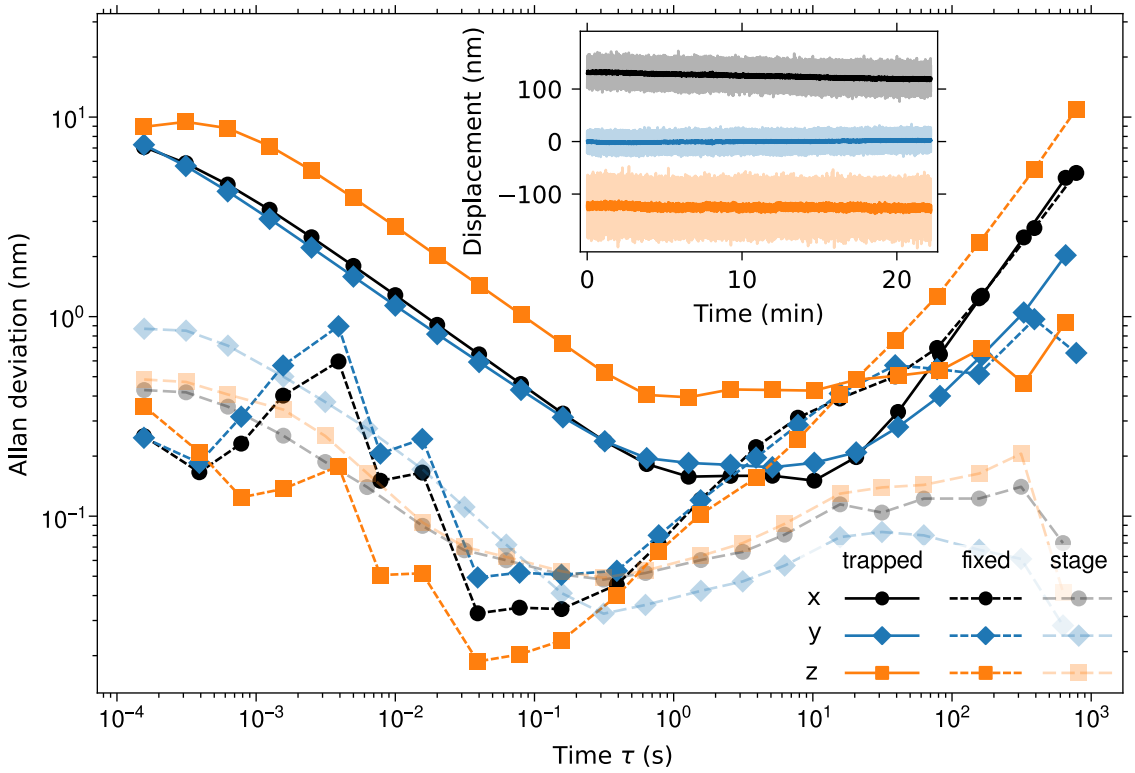

Fig. 7.3 | Stability of the optical trap. Allan deviation vs. averaging time for a trapped microsphere in bulk (solid lines), a fixed microsphere on a sample chamber surface aligned in the center of the trap (short-dashed lines) and the monitor signals of the piezo sample stage (long-dashed lines). Inset: Displacement signal of the trapped microsphere.

achievable precision of force measurements of less than 25 fN. From Fig. 7.3 one can also deduce the mean force drift from the slope of the ADEV for long averaging times. The force drifted with less than 10 fN s^{-1} in all three axes.

To test how precise measurements can be, when performing surface-based assays a microsphere was fixed on the sample surface. The ADEV-plots (short-dashed lines in Fig. 7.3) show a minimum at averaging times around 0.1 s. For times larger than 0.2 s drift of about 0.7 Å s^{-1} was compromising the precision. The peaks in the ADEV for $\tau \lesssim 20$ ms are due to resonances. Because these peaks did not show up in the recorded stage signal (long-dashed lines in Fig. 7.3), these resonances might result from the sample holder. Also, drift cannot be seen in the stage signal. Therefore, it is possibly caused by temperature changes that cause the focal plane to move relative to the sample stage.

7.4. Resolution of the optical tweezers

To test the resolution capabilities of the optical tweezers setup close to the sample surface, a microsphere was fixed on the sample surface and a square signal with a period of 4 s was applied to simulate steps of different sizes. The smallest step size that was tested was 1.5 nm (cyan lines in Fig. 7.4). The displacement signal is associated with considerable noise. To

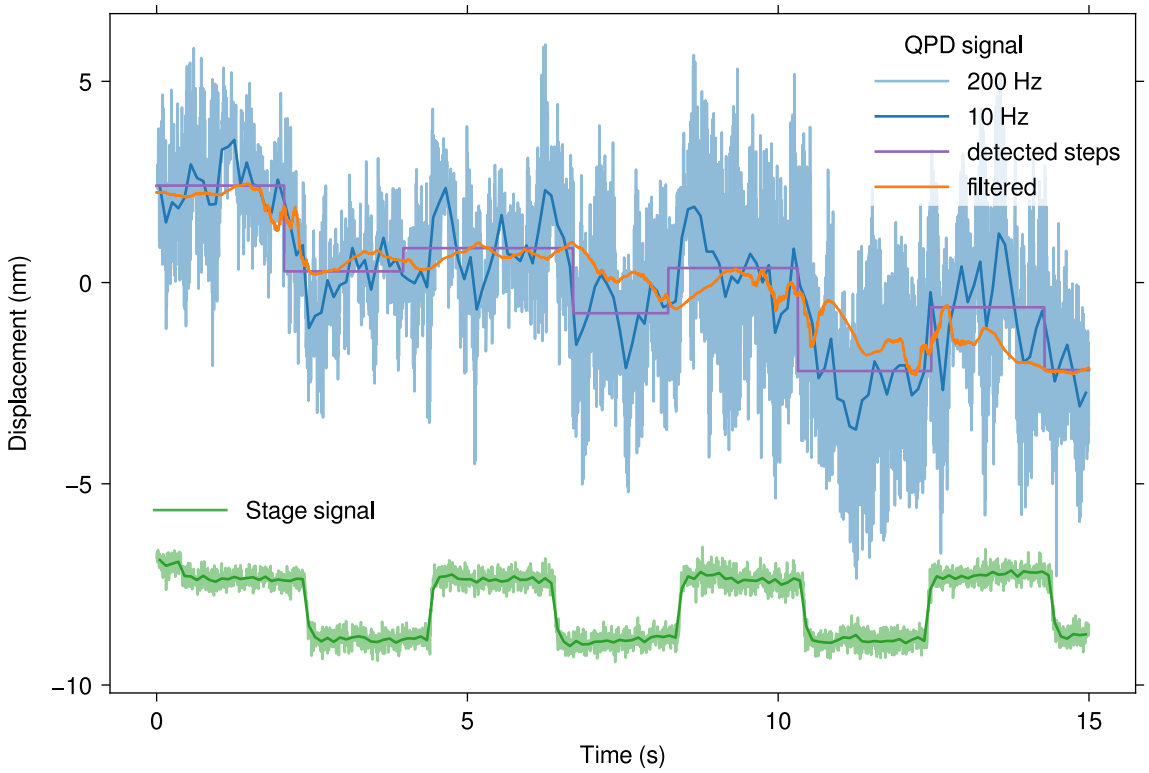

Fig. 7.4 | Resolution of the optical trap. Displacement of a polystyrene microsphere vs. time. Steps of 1.5 nm were simulated by applying a square signal to the sample stage. The signal was acquired with a sampling frequency of 40 kHz and block averaged to 200 Hz (light colored lines) and 10 Hz (full colored lines). The raw signal was analyzed by a step finding algorithm implemented in the PyOTI software package. All 1.5 nm steps could be resolved with SNRs of 5.3.

reveal the underlying steps the signal was fed into a step finding algorithm, implemented in the PyOTIsoftware package [51, 52]. The step finding algorithm utilizes a forward-backward non-linear filtering technique to reduce the noise on the raw signal (orange line in Fig. 7.4) [53]. The filter parameters were set to: filter-time = 1.5 s, minimal-dwell-time = 2.0 s and minimal-step-size = 0.8 nm. All simulated steps could be resolved (magenta line in Fig. 7.4). The mean detected step size was 1.6 nm. The mean standard deviation on the steps was 0.3 nm, which resulted in a mean SNR of 5.3.

The step size is limited by the available bit-depth of the analog output channel that controls the setpoint of the stage position. The total range of one axis is 50 µm. The controller card (NI PXI-6733) has a resolution of 16 bit. Thus, the minimal step size is 1.5 nm. To decrease it further, one could use a voltage divider. This would effectively decrease the available range of the stage and, thus, decrease the minimal accessible length per bit.

Part IV.

Calibration of optical tweezers

8. Précis on the calibration of optical tweezers

8.1. Measuring forces and displacements

In biophysical optical tweezers experiments, functionalized particles are trapped and used to investigate the mechanics of a system of interest, *e.g.* the interaction mechanisms of single motor proteins with their biological counterpart, such as kinesins and microtubules. The interaction of such specimen comprises both, the displacement of the particle and the force acting on it. Both are related to the deflection of the trapping laser. Measuring the deflection of the laser beam, on the one hand, directly measures the force that is acting on the trapped particle. On the other hand, the displacement of the particle itself, which caused the deflection of the laser, is an important physical quantity. Moreover, if the particle is not displaced too far, the response of the optical trap is linear, and the force that is needed to pull the particle out of the trap, can be calculated.

Detection methods typically either measure the force or the displacement. Both methods have their benefits: direct force measurements can be done without repetitive determination of the displacement-to-force conversion factor, but leaves the measurement of the particle displacement behind. Measuring the particle displacement, gives deeper understanding of the process, but requires the calibration of the trap. The following paragraphs give an overview of different methods to calibrate optical tweezers and their potential pitfalls.

8.2. Direct force measurement

When a particle is trapped, its position fluctuates around an equilibrium position, because it is subjected to Brownian motion. If a net force is applied to the particle in addition to the thermal forces, this equilibrium position changes. Because of the interaction with the light, the momentum of the light changes, which leads to a deflection of it (see Chapter 2). Thus, measuring the deflection gives a direct measurement of the rate of change of the momentum of light, which corresponds to the applied force. This method has been presented by Smith and his colleagues in 2003 to directly measure lateral forces [54]. It was further developed and investigated in relation to back-focal-plane interferometry by Farré *et al.* [55, 56]. Thalhammer *et al.* investigated under which situations the method can also be used to measure axial forces [57]. To directly measure the force, the conservation of linear momentum must be fulfilled, *i.e.* all of the light that has changed its momentum must be detected. Practically, this is also one of the pitfalls of the technique, because not all scattering angles can be detected.

Direct force measurements require the use of a high NA condenser and thin sample chambers. To measure the deflection of the laser light, the principle of back-focal-plane interfer-

ometry is followed[15]. The scattered and unscattered light is collected by a condenser lens and relayed on a position sensitive device. To collect most of the forward scattered light, a condenser with high NA (> 1) should be used. To further prevent loss of light, thin sample chambers are necessary or trapping should take place close to the light-collecting condenser lens. However, because trapping efficiency is reduced far away from the sample surface, if oil-immersion objectives are used for trapping, thin flow cells might be preferred. This geometry might reduce the experimental possibilities further, for example cell cultures might require thick flow cells.

Nonetheless, once the light is collected correctly and the diode's center has been aligned with the center of the beam, the output will be the deflection signal, S, in volts. It is related to the force that acts on the trapped particle by:

$$F = -\alpha S, \tag{8.2.1}$$

where alpha is the volt-to-force conversion factor. It only depends on the optical system:

$$\alpha = \frac{R_D}{\Psi f' c}, \tag{8.2.2}$$

where R_D is the (half-) size of the detector, Ψ is the detector efficiency, in volts per watt, f' is the effective focal length of the optical system formed by the condenser and some relay optics, and c is the speed of light. α does not depend on the medium, the particle size, nor height—given that all the light is collected. Therefore, α is to be determined only once and the trap could be used to measure forces acting on trapped probes without repeated calibration[16]. This is especially important in situations where displacement calibration of the microsphere is difficult or even impossible, *e.g.* when trapping is done inside cells [58].

8.3. Indirect force measurement

8.3.1. Measuring the displacement

Particle displacement from its equilibrium position in the trap can be measured by video tracking and back-focal-plane interferometry (BFPI). Once the displacement is known in physical units, a small displacement can be converted into a force, if the trap stiffness is known.

Video tracking records the movement of the trapped particle. Once the camera is calibrated, *i.e.* the pixel-to-length conversion factor is known, the particle displacement is quickly determined. This method usually involves the usage of a separate tracking laser, to make tracking independent of the used trapping laser power. Although video tracking seems appealing at the first sight, the method suffers from its low bandwidth[17]and the measurement of the displacement relative to the trap center is difficult, especially when the trap is moved [16].

[15]Back-focal-plane interferometry should be realized with a position sensitive diode instead of a QPD, to correctly measure the center of mass of the scattered intensity profile [56].

[16]The stated independence of the probe is deduced from the experiments done by Farré *et al.* [56], but further dependence on sample thickness, particle size, shape, and material might be possible.

[17]The current upper limit for video tracking of small particles is at about 10 kHz [59]

Back-focal-plane interferometry uses a position sensitive device, such as a quadrant photo diode (QPD) or a position sensitive diode, to track the displacement of the particle relative to the trap center in the conjugate plane [26]. This method has the advantage of a high bandwidth ($\sim$ 100 kHz), but, in general, requires the calibration of the device for every trapped particle. In the picture of BFPI, Eq. (8.2.1) becomes

$$F = \kappa\beta S, \tag{8.3.1}$$

where the measured displacement signal, S, is now converted via the detector sensitivity or displacement sensitivity, β, to a physical displacement. The trap stiffness, κ, converts the displacement into a force. Here, the trap is modeled as a harmonic potential, which holds only in a small region around the trap center. This method is related to the direct force measurement via $\alpha = \kappa\beta$. Although, as stated above, this equation only holds if all of the light is collected. Otherwise κ and β differ in general and will depend on the sample and the trapped particle. In the case that video tracking is used, the displacement sensitivity is known and only the trap stiffness needs to be determined.

However, in BFPI, the experimenter is left with the task of determining both calibration factors, κ and β. Different approaches exist to find these factors, separately.

8.3.2. Determining the displacement sensitivity

The detector response can be calibrated by scanning through a microsphere that was fixed on the sample surface. This approach has the disadvantage that a particle must be brought to the surface and needs to be able to stick to the surface. An experiment could not be performed with a calibrated microsphere. Furthermore, it is difficult to completely immobilize a particle on the surface. Calibrations of an ensemble of stuck microspheres were done for better statistics. The pitfalls of this method are manifold. The particle sizes can differ, depending on the supplier. Also, the displacement sensitivity depends on the height, *i.e.* the distance of the particle to the sample surface. This dependence arises due to aberrations but also changes in the total amount of collected light. In addition, it is difficult to position the microsphere axially in the correct plane, which can lead to large errors. To determine the axial response, the microsphere can also be scanned in the vertical direction while being pushed against the surface. This approach—for non-sticky microspheres at least—results only in half-scans. A fit to the (half-) profile was then used to determine the displacement sensitivity in the axial direction [16].

A method that makes the scanning through a stuck microsphere obsolete, is the power spectrum method. In this method the Brownian motion of the particle in the trap is analyzed and, due to the inferred knowledge of the size, the viscosity, and the temperature, the displacement sensitivity can be deduced from a fit to the power spectrum. Because this method is the base of the most precise calibration method it is discussed in detail below.

8.3.3. Determining the trap stiffness

To find the trap stiffness different techniques can be used. One can calculate the force from basic physical principles (see Chapter 2). However, such approaches are often based on

[17] This region is typically about $\lesssim \lambda/(4n)$, with λ being the wavelength of the trapping laser and n the refractive index of the medium.

various assumptions and depend on uncertain values, such as the microsphere size, height, laser profile, *etc*. Therefore, forces were measured against other known forces, *e.g*. the gravitational force on the particle or the drag force when the medium or the microsphere was moved with a known velocity [60]. Another method uses Boltzmann statistics to determine the shape of the energy potential of the trap [61, 62]. The probability, $P(x)$, of finding the trapped particle at a displacement, x, is proportional to the Boltzmann factor

$$P(x) \propto \exp\left(-\frac{\phi(x)}{k_B T}\right) \tag{8.3.2}$$

Experimentally, a normalized histogram is a measure of $P(x)$. Hence, the potential can be determined by solving for $\phi(x)$. Within a range the potential can be approximated by a harmonic one,$\phi(x) = \kappa x^2/2$, and a fit could determine the trap stiffness. However, one requirement for this and the following method is that the displacement sensitivity is known.

Also the equipartition theorem has been used to deduce the trap stiffness. Here, the variance of the measured displacement signal (= mean squared displacement) is related to the thermal energy of a particle and the trap stiffness by [16, 63]:

$$\langle x^2 \rangle = k_B T/\kappa \tag{8.3.3}$$

This method, practically has a high uncertainty because the variance of the signal, x, could carry a lot of external noise unrelated to the Brownian motion in the trap (see Section 6.1). This extra noise would result in a systematic overestimation of the variance and, thus, the trap stiffness would be underestimated.

To circumvent the overestimation of the (true) variance of the displacement of the trapped particle due to Brownian motion, the variance can be analyzed spectrally. In this sense contributions of external sources of noise can be excluded from the analysis by selecting only the relevant bandwidth. This method, as already mentioned above, is the power spectral density analysis. It has become the state of the art method to calibrate optical traps.

8.4. Power spectral density analysis

8.4.1. Overview

Calibration of optical tweezers can be done by passively observing the Brownian motion of a trapped particle and analyzing the signal's power spectral density (PSD). This method has been described in great detail elsewhere [26, 64–66]. For a deep understanding of the subject, the reader is advised to consult these publications. Nonetheless, the following chapter will give a summary of those. Without applying any additional forces, the method is widely used and referred to as the passive PSD analysis. Applying an additional sinusoidal drag force, is less often used and is referred to as the active PSD analysis. The chapter, first, describes the theoretical power spectrum, which is expected from pure Brownian motion, and, second, describes the experimental one, which is degenerated through detection and digitalization. It, further, summarizes the passive PSD analysis and shows the benefits of the active method.

8.4.2. The theoretical power spectrum

8.4.2.1. The simple PSD for a trapped microsphere

To derive a theoretical description of the power spectral density of the position transient of a particle that is subject Brownian excitation through a surrounding viscous fluid and that is trapped in a harmonic potential, one solves the Langevin equation of motion:

$$m\ddot{x} + \gamma\dot{x} + \kappa x = F_{\text{thermal}}(t), \tag{8.4.1}$$

where $x = x(t)$ is the distance between the particle and the center of the potential, m is the mass of the particle, γ is the drag coefficient, κ the trap stiffness and $F_{\text{thermal}} = \sqrt{2k_BT\gamma}\xi(t)$ is the thermal force, which depends on the thermal energy k_BT and the drag on the sphere. The thermal force is, to a first approximation, an uncorrelated random process (= white noise) represented by the normalized function $\xi(t)$. It has the properties $\langle\xi(t)\rangle = 0$ and $\langle\xi(t_1), \xi(t_2)\rangle = \delta_D(t_1 - t_2)$, where δ_D is Dirac's delta-function. In the simple case where $m/\gamma \ll \kappa/\gamma$, the inertial term in Eq. (8.4.1) can be neglected, resulting in

$$\dot{x} + 2\pi f_c x = \sqrt{2D}\xi(t), \tag{8.4.2}$$

where the Einstein relation,

$$D = k_BT/\gamma, \tag{8.4.3}$$

and $2\pi f_c = \kappa/\gamma$ was used. The square of the Fourier-transform of Eq. (8.4.2) for discrete data points yields the power spectral density of one measurement of length T_{msr}:

$$P_k^{(ex)} = \frac{|\tilde{x}_k|^2}{T_{\text{msr}}} = \frac{D}{\pi^2 T_{\text{msr}}(f_c^2 + f_k^2)}|\tilde{\xi}_k|^2, \tag{8.4.4}$$

where k is an integer number, corresponding to a discrete frequency $f_k = k/T_{\text{msr}}$. Each value, $P_k^{(ex)}$, for each k is an exponentially distributed random variable due to $|\tilde{\xi}_k|^2$ (see Ref. 14 in Nørrelykke & Flyvbjerg, 2010 [66]). Averaging over a set of N power spectra, $P_k^{(ex)}$, yields the average (one-sided) power spectral density

$$P_k = \langle P_k^{(ex)}\rangle_N. \tag{8.4.5}$$

When averaging Eq. (8.4.4), the average PSD, P_k, has the form of a Lorentzian:

$$P_k = \frac{D}{\pi^2(f_c^2 + f_k^2)}. \tag{8.4.6}$$

For a low number of averages, P_k is a Gamma-distributed random variable. As the number of averages increases ($N > 20$), P_k approaches a normal distribution. The standard deviation of an exponentially distributed variable is equal to its expectation value, hence

$$\langle(P_k^{(ex)} - P_k)^2\rangle = P_k. \tag{8.4.7}$$

If N is large, the central limit theorem applies and the standard deviation of each value P_k scales as (comp. Eq. (6.2.2))

$$s_{P_k} = \frac{P_k}{\sqrt{N}}. \tag{8.4.8}$$

The shape of the power spectrum derived for the simple case (Eq. (8.4.6)) with negligible mass of the particle is a Lorentzian. It can be used to find the parameters D and f_c by fitting. However, to achieve high precision, *i.e.* low uncertainties for the two parameters, and hence, the calibration factors β and κ, one needs to consult a more precise model of the power spectrum.

8.4.2.2. The hydrodynamically correct power spectrum

The simple power spectrum derived above neglects three important effects (i) inertia of the sphere, (ii) inertia of the entrained fluid, and (iii) near-surface effects that change the drag. The mass of the sphere was neglected under the assumption that the response time of the trap is much lower than the inertial response of the sphere. In other words the optical trap could not measure the inertial response of the sphere. This is a valid approximation for weak traps (*i.e.* low corner frequency, f_c) in general and valid for polystyrene microspheres, but fails for more dense ones made of materials such as silica or titania.

Inertia of the entrained fluid causes a colored thermal noise. In the derivation of Eq. (8.4.6) it was silently taken for granted that the drag coefficient is a static quantity, *i.e.* it is independent of frequency and thus the particles velocity. This independence is a consequence of Einstein's approximation to Brownian motion. In fact, γ depends on frequency. Stokes derived the friction force on a sphere undergoing oscillatory motion in 1850 [67]. The energy dissipating term is Stokes' drag for oscillatory motion of a sphere [68]:

$$\gamma_0(f) = \gamma_0 \left(1 + (1-i)\frac{R}{\delta(f)} - i\frac{2}{9}\frac{R^2}{\delta(f)^2}\right), \tag{8.4.9}$$

with

$$\gamma_0 = 6\pi\eta R, \tag{8.4.10}$$

being Stokes' drag at constant velocity for a sphere of radius R in a medium with viscosity η. The frequency dependent term $\delta(f)$ in Eq. (8.4.9) a length scale corresponding to the penetration depth of the exponentially decaying velocity field of the entrained fluid surrounding the sphere. The penetration depth is given by [68]

$$\delta(f) = R\sqrt{f_\nu/f}, \tag{8.4.11}$$

where the characteristic frequency $f_\nu = \nu/(\pi R^2)$ depends on the kinematic viscosity ν and the cross-section of the sphere. Hence, the drag on the sphere is caused by a frequency-dependent amount of entrained fluid. Consequently, this causes a frequency-dependent amount of mass and thus inertia being involved. Notably, in the limit $f \to 0$, the penetration depth and hence the involved mass becomes infinite. In general, the inertia of the entrained fluid introduces correlation of the spheres movement, which, according to the fluctuation-dissipation theorem, introduces a "color" to the thermal noise that causes Brownian motion.

The proximity of a plane surface increases the drag coefficient. The simple theory above, considers a sphere that is trapped in the bulk medium, where surface effects are irrelevant. This is usually not the case, the sphere is in the vicinity of the sample chamber surface. As

a consequence of the no-slip boundary condition, where the fluid is at rest at the surface, the closer the particle gets to the surface, the more shear stress is acting on the fluid. Hence, the drag coefficient must dependent on the position of the trapped sphere above the sample chamber surface. This situation was investigated by Faxén [69] for the case when a sphere is moving parallel ($\parallel$) to a plane surface.[18] Brenner derived an exact solution for the perpendicular ($\perp$) case [71]. Approximate formulas have been developed for both corrections [72]:

$$\lambda_{\parallel}(R/h) = \frac{\gamma_{\parallel}(R/h)}{\gamma_0} = \left(1 - \frac{9R}{16h} + \frac{R^3}{8h^3} - \frac{45R^4}{256h^4} - \frac{R^5}{16h^5}\right)^{-1}, \tag{8.4.12}$$

$$\lambda_{\perp}(R/h) = \frac{\gamma_{\perp}(R/h)}{\gamma_0} = \left(1 - \frac{9R}{8h} + \frac{R^3}{2h^3} - \frac{57R^4}{100h^4} + \frac{R^5}{5h^5} + \frac{7R^{11}}{200h^{11}} - \frac{R^{12}}{25h^{12}}\right)^{-1}. \tag{8.4.13}$$

where h is the height of the sphere (bead-center–surface distance). Both equations are plotted with respect to height in Fig. 8.1A.

The so-called hydrodynamically correct power spectrum takes these three considerations into account. Its average (comp. Eq. (8.4.6)) has the following shape [65]:

$$P_{\mathrm{T}}^{\mathrm{hydro}}(f) = \frac{D_0\,\mathbb{R}\mathrm{e}(\phi)}{\pi^2\left(\left[f_{c,0} + f\,\mathbb{I}\mathrm{m}(\phi) - f^2/f_{m,0}\right]^2 + \left[f\,\mathbb{R}\mathrm{e}(\phi)\right]^2\right)}, \tag{8.4.14}$$

where $D_0 = k_B T/\gamma_0$ is the particle's diffusion coefficient deep in the medium, $f_{\mathrm{c},0} = \kappa/(2\pi\gamma_0)$ is the corner frequency, $f_{\mathrm{m}^*,0} = \gamma_0/(2\pi m^*)$ is the characteristic frequency describing the inertial response of the sphere and the entrained fluid to the thermal noise. The effective mass is given by $m^* = m_{\mathrm{p}} + \frac{2}{3}\pi R^3 \rho_{\mathrm{fl}}$, with m_{p} being the mass of the sphere and ρ_{fl} the density of the fluid.

The complex function, $\phi = \phi(f, R/h)$, in Eq. (8.4.14) is the frequency-dependent representation of the correction of the drag near a plane surface (Eq. (8.4.12)). It was given by Berg-Sørensen and Flyvbjerg [64, 68]—unfortunately, without publishing the details—following Lorentz derivation [70] for oscilatory motion of a sphere. The result was later Padé-approximated to [65]:

$$\begin{aligned}\phi(f, R/h) &= \frac{\gamma_{\parallel}(f, R/h)}{\gamma_0} \\ &= \frac{1 + (1-i)\sqrt{\frac{f}{f_\nu}} - i\frac{2}{9}\frac{f}{f_\nu}}{1 - \frac{9}{16}\frac{R}{h}\left(1 - \frac{1-i}{3}\sqrt{\frac{f}{f_\nu}} + i\frac{2}{9}\frac{f}{f_\nu} - \frac{4}{3}\left[1 - \exp\left(-\frac{(1-i)(2h-R)}{R}\sqrt{\frac{f}{f_\nu}}\right)\right]\right)}.\end{aligned} \tag{8.4.15}$$

The nominator of Eq. (8.4.15) is the frequency dependent term of Stokes drag (Eq. (8.4.9)), where $\delta(f)/R = \sqrt{f_\nu/f}$ has been used. The denominator is the frequency-dependent version of Lorentz' first-order approximation to account for Faxén's law.

[18] A first order approximation was derived by Lorentz, earlier in 1907 [70]:

$$\lambda_{\parallel} \approx (1 - 9R/16h)^{-1}.$$

Because Eq. (8.4.12) lacks a second order term, it is valid within 1% for $h > 3R$ [64].

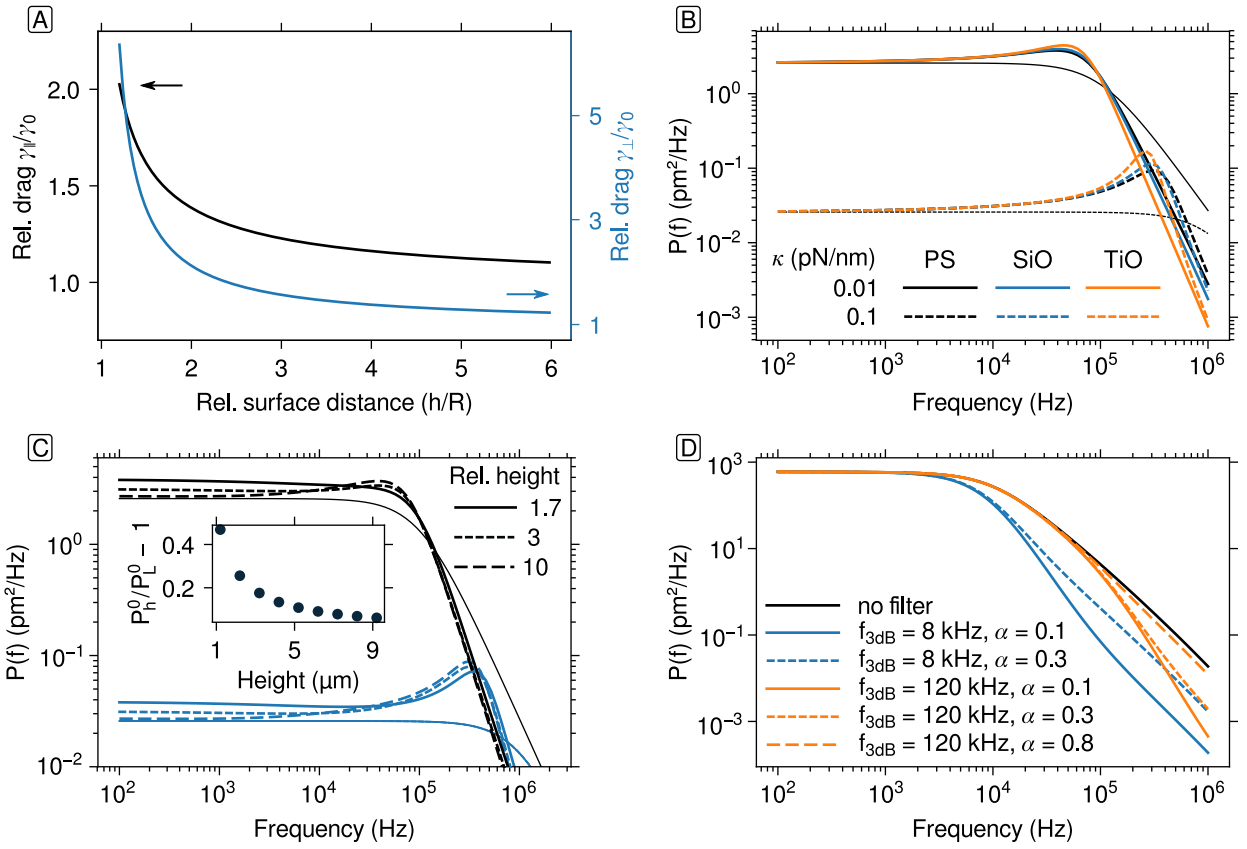

Fig. 8.1 | Hydrodynamics of a sphere close to a plane wall. (A) Relative drag coefficient (Eqs. (8.4.12) and (8.4.13)) vs. relative surface distance. **(B and C)** PSDs according to Eq. (8.4.14) for microspheres with a radius of 1.0 µm with respect to (B) trap stiffnesses of 0.01 pN/nm and 0.1 pN/nm and different materials: polystyrene (PS), silica (SiO_2), and titania (TiO_2). (C) PSDs for different heights of a polystyrene sphere and trap stiffnesses 0.01 pN/nm (black) and 0.1pN/nm (blue). A Lorentzian-shaped PSD (Eq. (8.4.6)) is plotted (thin lines) for comparison. The inset in (B) shows the deviation of the plateau relative to Eq. (8.4.6) vs. height. The PSDs are shown for a trap stiffnesses of 0.1 pN/nm (solid lines in (B) and blue lines in (C)) and 0.01 pN/nm (dashed lines in (B) and black lines in (C)). **(D)** Effect of parasitic low-pass filtering of the detection device for different combinations of the cut-off frequency, $f_{3\,\mathrm{dB}}$, and α (comp. Eq. (8.4.17)).

The hydrodynamically correct PSD (Eq. (8.4.14)) is plotted in Fig. 8.1B, with respect to different materials of a trapped microsphere with $R = 1.0\mu$mand a weak and strong trap. A resonance appears for stronger traps, which increases in quality for denser materials. Figure 8.1C, shows the behavior of Eq. (8.4.14) for a polystyrene microsphere of same radius at different heights and for a weak and a strong trap. The hydrodynamic resonance decreases the closer the microsphere gets to the surface. For a very close miscrophere the resonance disappears. Yet, the power (the area under the peak) is transferred to lower frequencies, which leads to an increasing plateau (Fig. 8.1C, inset). Fitting of the same data with a Lorentzian-shaped PSD (Eq. (8.4.6)) would lead to overestimation of D and therefore an underestimation of the drag. Both plots show the power at frequencies $f > f_c$ decreases

faster than the simple Lorentzian PSD.

Eq. (8.4.14) was successfully fit to optical tweezers data that showed the experimental proof of the colored thermal noise [73, 74]. After these measurements, the hydrodynamically correct power spectrum has also lead to controversy. Its validity was doubted because of the intransparent derivation [75]. The measurements also lead to the formulation of a partial-slip boundary condition for a sphere near a plane surface [76]. The hydrodynamically correct power spectrum was further utilized to measure near surface effects, such as the surface potentials of differently treated surfaces [72].

To date, there is no hydrodynamically correct description of the PSD for axial oscillatory motion of a sphere close to a plane surface. A representation of Eq. (8.4.13) with respect to frequency ought to be derived. Thus, one is left with the simple PSD (Eq. (8.4.6)) for the axial PSD data.

8.4.3. The experimental power spectrum

8.4.3.1. Parasitic filtering of photodiodes

The experimentally acquired position data are in general convolved with the characteristics of the detection and acquisition system. In Fourier-space this results in a multiplication with the detection system response function. The PSD is proportional to the square of the Fourier-transform, hence the detector characteristics, $P_{\mathrm{det}}(f)$, are multiplied with the theoretical power spectrum:

$$P_{\mathrm{exp}} = P_{\mathrm{T}}(f) \times P_{\mathrm{det}}(f). \tag{8.4.16}$$

The detector acts as a low-pass filter [64, 77]. The characteristics of this filter depend on the quantum efficiency of the device for the used trapping laser wavelength and the incident power. The quantum efficiency depends on the ability of the diode material—which often is doped silicon as a semi-conductor material—to absorb incident photons. The absorption depends on the wavelength of the incident light. A lower absorption causes photons to generate an electron-hole pair deeper inside the diode. If photons were absorbed in the depletion zone of the photodiode, the electron-hole pair causes an immediate photo-current, because the distance to the conducting p- and n-layer is short. If the absorption happens deeper in the diode, a generated electron-hole pair needs to diffuse through the n-layer of the diode. This diffusion delays the generation of a photo-current and blurs the detection dynamics and essentially acts as a low-pass filter. The response of the photodiode can, therefore, be described by an immediate response to a fraction of photons that are absorped in the depletion zone, α, and a fraction, $1-\alpha$, which is low-pass filtered. The derivation given by Berg-Sørensen *et al.* in their 2006 paper considers an undefined number of these relaxation modes [77]. However, in the simple case, the power spectral response is described as:

$$P_{\mathrm{det}}(f) = \alpha^2 + \frac{1-\alpha^2}{1+(f/f_{3\,\mathrm{dB}})^2}, \tag{8.4.17}$$

where $f_{3\,\mathrm{dB}}$ is the cut-off frequency of the low-pass filter. Whereas this frequency is independent of the wavelength and temperature, α depends on these parameters.

Nonetheless, photodiodes exist that were optimized for the widely used trapping laser wavelength of 1064 nm. These diodes have a bandwidth, *i.e.* a cut-off frequency, of about 120 kHz. The additional application of a revers bias increases the depletion zone increasing the probability of electron-hole pair generation at this site and thus increasing α. Figure 8.1D shows the impact of different values for *alpha* and $f_{3\,\mathrm{dB}}$ to the shape of the PSD. Standard photo-diodes with a bandwidth of only 8 kHz change the PSD considerably. Accounting for this parasitic filtering when fitting is necessary to prevent underestimation of the corner freqeuncy and the thus the trap stiffness. Using a photo-diode that is optimized for 1064 nm makes the additional modification of the model-PSD unnecessary for sampling frequencies up to ≈ 100 kHz.

8.4.3.2. Aliasing

The conversion of an analogue signal into a digital one, in general, leads to the question of aliasing. A signal that is sampled at a given frequency, f_{sample}, can only be represented by a sum of sine functions with frequencies up to the Nyquist-frequency. This fact is stated in the Nyquist sampling theorem. The Nyquist frequency is half the sampling frequency, $f_{\mathrm{Nuquist}} = f_{\mathrm{sample}}/2$. However, when sampling an analogue signal, it generally consists of fluctuations that can be represented by sine functions of even higher frequencies than the chosen sampling frequency. Because energy is conserved, these high-frequency signals map into the sampled region and appear in the power spectral density as increased high-frequency power. Typically this effect is overcome with delta-sigma conversion or by low-pass filtering the analogue signal prior to sampling. In the case of delta-sigma conversion the analogue signal is sampled at a high frequency and then down-sampled by filtering to the desired sampling frequency. This approach deals well with aliasing; and data acquisition done by this method overcomes aliasing. Without delta-sigma filtering, aliasing will take place and must be considered to be able to fit power spectra.

If an acquired signal is subjected to aliasing, the experimental PSD becomes [64]:

$$P_{\mathrm{exp}}^{\mathrm{aliased}}(f) = \sum_{n=-\infty}^{\infty} P_{\mathrm{exp}}(f + n\Delta f_{\mathrm{sample}}). \tag{8.4.18}$$

In practice, the infinite sum can be sufficiently approximated by considering the first terms with $n \gtrsim 9$.

8.4.4. Calibration of a trapped particle

8.4.4.1. Passive calibration

Least-squares fitting of one of the Eqs. (8.4.6), (8.4.14), (8.4.16) or (8.4.18) to the experimental power spectrum allows to determine the parameters D_{V} and f_{c}, the diffusion coefficient in volts and the corner frequency in hertz, respectively. These parameters are related to the calibration factors, namely the displacement sensitivity, β, and the trap stiffness, κ, by

$$\beta = \sqrt{\frac{D}{D_{\mathrm{V}}}} = \sqrt{\frac{k_B T}{\gamma D_{\mathrm{V}}}} \tag{8.4.19}$$

and

$$\kappa = 2\pi f_c \gamma, \tag{8.4.20}$$

respectively.

Because the diffusion coefficient in Eq. (8.4.19) by is known via the Einstein relation (Eq. (8.4.3)), it can be used to calculate β. However, this approach requires the knowledge of the temperature and the drag coefficient. The temperature can be measured (see Section 5.3.3) and is needed to calculate the drag coefficient from Eq. (8.4.10), whereby the viscosity is also a function that depends nonlinearly on temperature, $\eta = \eta(T)$. By assuming $\gamma = \gamma_0$, one can then calibrate a trapped particle.

However, the Stokes drag is only an approximation to the real drag. Far away from the surface using monodisperse microspheres or microspheres of $R \approx \omega_0$, where ω_0 is the beam waist of the trap [78], this approach works reasonably well for many situations. The interaction of the particle with the sample chamber surface, can be accounted for by correcting Stokes drag with one of Eqs. (8.4.12) and (8.4.13) or even the Oseen-correction for the interaction of two walls [79][19]

$$\lambda_{\mathrm{Oseen}}(h, d_{\mathrm{ch}}, R) = \lambda\left(\frac{R}{h}\right) + \lambda\left(\frac{d_{\mathrm{ch}} - h}{R}\right) - 1, \tag{8.4.21}$$

which implies that the height of the particle above the surface and the separation, d_{ch}, must be known precisely. Otherwise, the uncertainties within the parameters temperature, viscosity, height, and radius could add up to unwanted large values.

This calibration procedure is referred to as the *passive* PSD calibration. However, as outlined above, other calibration methods used a known drag force on the sphere, while the trap or the sample chamber was moved, to determine the trap stiffness. When combining the PSD analysis with this method, one degree of freedom is gained, by directly measuring the displacement sensitivity and, hence, one circumvents the need to calculate the drag coefficient in Eq. (8.4.19).

8.4.4.2. Active PSD analysis

A sinusoidally driven trapped particle allows to measure the displacement sensitivity directly [65]. If the sample stage or the optical trap is driven along one of the lateral axes by a sine function of known amplitude, A, and frequency, f_{drive}, the PSD of a trapped particle will show a sharp peak at that frequency.[20] This peak corresponds to the root mean square (rms) displacement of the trapped particle from the center of the trap due to the drag through the fluid. The spectral power at the driving frequency, measured in V^2, is

$$W_{\mathrm{exp}} = P_{\mathrm{peak}} \Delta f, \tag{8.4.22}$$

where $\Delta f = 1/T_{\mathrm{msr}}$ is the frequency resolution of the experimental PSD. The power within the peak is given by $P_{\mathrm{peak}} = P(f_{\mathrm{drive}}) - P_{\mathrm{thermal}}(f_{\mathrm{drive}})$, where P_{thermal} is the thermal base

[19] This simple correction is only a superposition of both wall effects. However, in reality the interaction of a sphere between two walls is more complicated, because the flow fields are reflected on both walls and, thus, "iteratively" interfere with each other through the so-called backflows. This was investigated in more detail in Refs. [79, 80].

line caused by the Brownian motion of the particle. This base line could, for example, be determined from the fit to the power spectrum.

Furthermore, if the driving amplitude and frequency of the stage are known, the expected rms-amplitude and so the rms-power in the position PSD can be determined analytically by[21]

$$W_{\mathrm{th}} = \frac{A^2}{2(1 + (f_{\mathrm{c}}/f_{\mathrm{drive}})^2)}. \tag{8.4.23}$$

The power W_{th} is given in m^2 and, thus, serves as a ruler to determine the displacement sensitivity [65]:

$$\beta = \sqrt{\frac{W_{\mathrm{th}}}{W_{\mathrm{exp}}}}. \tag{8.4.24}$$

This method determines β directly and one can now solve Eq. (8.4.19) for γ, which leaves the absolute temperature as the only unknown parameter. The error in the absolute temperature is typically small, because an error of 1 K causes only $\approx 0.3\,\%$ error in the calibration. Therefore, the uncertainties on both β and κ are systematically reduced.

8.5. Height-dependent active PSD analysis

The calibration factors β and κ depend on the distance between the trapped particle and the sample-chamber surface, *i.e.* the height. This height-dependence is mainly due to spherical aberrations in the focal point caused by the refraction the laser light at the glass–water interface [81]. To a first-order approximation the height-dependence of β and κ, respectively, is linear:

$$\beta_\xi(h) = m_{\beta,\xi} \cdot h + \beta_{0,\xi} \tag{8.5.1}$$
$$\kappa_\xi(h) = m_{\kappa,\xi} \cdot h + \kappa_{0,\xi}. \tag{8.5.2}$$

In general, this relationship is different for each axis, $\xi = \{x, y, z\}$. Thus, calibrating a trapped particle at different heights allows one to find the height-dependence of β and κ.

The height-dependence of the drag that a trapped particle is exposed to, can further be utilized to determine the true height of the particle, which is an important parameter in experiments that are carried out in close proximity to the surface. Because Eqs. (8.4.19)

[20] The driving frequency should be chosen such that the peak is located at one of the frequency values to avoid leakage, *i.e.* $T_{\mathrm{msr}} f_{\mathrm{drive}} =$ integer. Also, one should measure the amplitude of the sine from the monitor signal of the stage instead of taking the input value A for granted. According to the stage, its control parameters and the chosen driving frequency, the value can deviate significantly from the input amplitude [65]. Further, one must keep in mind that the measured peak corresponds to the root mean square value of the amplitude. Thus: $A = \sqrt{2} A_{\mathrm{rms}}$ for a sine function (comp. Eq. (8.4.23)).

[21] Here, the motion of the trapped particle is modeled by a Lorentzian-shaped PSD. This is a valid approximation for low driving frequencies f_{drive}, where Eqs. (8.4.6) and (8.4.14) do not significantly differ from each other [65].

and (8.5.1) must be equal at every height, one can arrange the equation for the uncorrected displacement sensitivity of the passive PSD calibration,

$$\beta_\xi^{\mathrm{pc}}(h) = \sqrt{\frac{D_0}{D_\mathrm{V}}} = \beta_\xi(h)\,\sqrt{\lambda(h)} = (m_{\beta,\xi}\cdot h + \beta_{0,\xi})\,\sqrt{\lambda(h)}, \tag{8.5.3}$$

where Stokes drag γ_0 (Eq. (8.4.10)) is naively used to calculate the diffusion coefficient D_0 according to Eq. (8.4.3). The correction to the Stokes drag (either of Eqs. (8.4.12) and (8.4.13)) is used such that $\gamma = \gamma_0\lambda$ and $D = D_0/\lambda$. Similarly, one can rearrange Eqs. (8.4.20) and (8.5.2) to find the uncorrected trap stiffness

$$\kappa_\xi^{\mathrm{pc}}(h) = 2\pi f_\mathrm{c}\gamma_0 = \frac{\kappa_\xi(h)}{\lambda(h)} = \frac{m_{\kappa,\xi}\cdot h + \kappa_{0,\xi}}{\lambda(h)}. \tag{8.5.4}$$

Hence, fitting the Eqs. (8.5.3) and (8.5.4) with the position of the surface as an additional fitting parameter, such that $h = \delta(h' - h_0)$, results in the true position of the sample surface. Here, δ is the focal shift of the trap position due to the refraction of the laser light at the glass–water interface [82].

Active PSD calibration, allows to either determine the radius of the particle or the viscosity of the medium. By directly measuring the displacement sensitivity and rearranging Eq. (8.4.19), one can calculate the drag by

$$\gamma_\mathrm{ex} = k_B T/(\beta^2 D_\mathrm{V}). \tag{8.5.5}$$

Hence the measurement of β reduces the number of assumption to the experiment and opens another degree of freedom to determine either the radius of the particle, if the viscosity is known, or vice versa by using an additional fitting parameter, c, that accounts for the correction in one of them relative to the specified radius of the manufacturer or assumed viscosity

$$\frac{\gamma_\mathrm{ex}(h)}{\gamma_0} = c_\eta \cdot c_R \cdot \lambda(h, c_R \cdot R)\,. \tag{8.5.6}$$

Here, $\lambda(h, c_R R)$ corresponds to the direction in which the particle was actively driven. Also, it is important to realize that only one of the parameters, either c_η or c_R, can be a fitting parameter, because of their direct correlation in Eq. (8.5.6).

It should further be emphasized, that all of the Eqs. (8.5.3), (8.5.4) and (8.5.6) hold information about the relative drag $\lambda(h, R)$. Thus, a fit of these functions to the experimental values for $\beta_\xi^{\mathrm{pc}}, \kappa_\xi^{\mathrm{pc}}$ and γ/γ_0 should be done globally, such that h_0 and $c_{\eta/R}$ are minimized according to the whole data set.

9. PyOTC – A framework to calibrate optical tweezers

Although, the above mentioned calibration procedures may appear simple on first sight, the underlying details of the fitting procedure requires knowledge about the physical models and might hinder experimenters to do precise measurements. A calibration software that takes care of most of the details of the calibration process can ease the handling of optical tweezers, could make the analysis more transparent to the community, and could further facilitate a standard that would increase the reliability of published results.

There is calibration software that focuses on the calibration of optical tweezers, but none of these packages inherently uses the active calibration approach nor handles the height-dependent calibration. The software package *tweezercalib* is implemented in *MatLab* (MathWorks Inc.) and provides power spectral density analysis based on a Lorentzian or the hydrodynamically correct PSD [83–85]. Another software, TweezPal, is a Microsoft® Windows®-based standalone calibration software that provides calibration via the Boltzmann-statistics approach [86]. Both software packages lack height-dependent and active PSD analysis. Moreover, they can only be used in conjunction with proprietary software (MatLab and MS Windows) that obligates to pay for software licenses.

PyOTC is an open source Python-based Optical Tweezers Calibration package. It provides the means for fast and easy, height-dependent passive and active PSD analysis. It is publicly available and licensed under the Apache 2.0 open source license. Furthermore, it can be adapted, further developed, and maintained by a whole community. The precise calibration routines—when carried out well—will lead to more reliable data and could, further, lead to an acknowledged standard within the community. The package integrates well with the cross-platform, open source and web-server-based programming and analysis platform Jupyter.

PyOTC is part of the Python Optical Tweezers Investigation and Calibration (PyOTIC) software, which consists two independent Python packages. Whereas the software presented here is focusing on the calibration of optical tweezers data, the second part, the Python Optical Tweezers investigation (PyOTI) package, provides sophisticated means to handle highly time-resolved and large datasets of optical tweezers experiments. PyOTI was developed by Tobias Jachowski. The joint software can be accessed via GitHub.[22]

[22] Both software packages are accessible online via the software development platform GitHub: https://github.com/cellular-nanoscience/pyotic

9.1. Features

PyOTC offers the following features:

1. Generation of PSDs from time series data
2. Load PSDs from data files
3. Generation of random time series data according to model function
4. Implementation of physical formulas for the drag and its corrections in the static and dynamic representation.
5. Manage individual power spectral density data, *i.e.* for one axis or particular experimental condition, plotting, masking, *etc.*
6. Manage PSD measurements, consisting of individual PSDs and additional experimental information, such as particle size, material and density, medium viscosity and density, temperature, measurement height, *etc.*
7. Manage PSD fitting:
   - Functions to account for detector response and aliasing
   - Manage fitting of PSDs, with corrections, and calculation of calibration factors and their uncertainties.
   - fitting of user-defined models
   - Inverse least-squares fitting with bias correction
   - Goodness of fit via reduced χ^2
8. Compatibility for different physical units
9. Generation of height calibration data from time series measurement (provided and pre-processed by a PyOTI-motion object)
10. Generation of height calibration data provided by individual PSD measurments at different heights
11. Manage height-dependent fitting and determination of particle height (h_0), radius or viscosity correction factors (c_R, c_η), and height-dependent displacement sensitivity and trap stiffness
12. Focal shift determination from oscillations on the QPD-sum signal

9.2. PyOTC workflow

This section should give a short overview of some of the functions used in a certain context when calibrating optical tweezers data. A more elaborate overview and example code can be found in the PyOTC documentation[23]. The functions presented here assume a working Python 3.4 (and higher) interpreter and an installed version of PyOTIC. The simple installation procedure can be found in the online documentation.

9.2.1. PSD generation from time-series data

Raw time-series data can be converted to a PSD via the function `pyotc.gen_PSD_from_time_series(x, fs, N_win)`, where the position data is given in the array `x`, `fs` is the sampling frequency and `N_win` is the number of windows the array `x` is split up. PSDs of each window are calculated and averaged afterward. To calculate the PSD Welch's algorithm [87] is used, but without the application of a window function. The function's output is a PSD-object. Optionally, the function can also calculate the experimental standard deviation of the mean power at each frequency by providing `cal_errors=True` in the function call.

9.2.2. Manage PSDs

Single PSD-objects hold the frequency, PSD-data and error arrays. They also provide masking-functionality, which can be used to ignore certain values at a specified frequency or frequency range. This feature is useful to exclude electronic, pink or mechanical noise (see Section 6.1). If the errors, *i.e.* the standard deviation for each PSD-value was not provided when the object was initialized, the theoretically expected error is calculated from Eq. (8.4.8). Furthermore, PSD-objects provide simple plotting of the PSD data in a double-logarithmic diagram.

Because, calibration is usually done in more than one axis, the PSDMeasurement-object can handle many PSD-objects. The single PSD-objects are also associated with defined experimental conditions, such as the temperature, (expected) particle size, height above the sample surface, particle material density, medium density and viscosity, *etc*. The experimental condition is set via an ExpSetting-object, which is used to initiate the PSDMeasurement-object. Once initiated the PSDMeasurement-object is associated with the respective PSD-objects. The following code example shows the initiation of a PSDMeasurement-object `pm`:

```
es = pyotc.ExpSetting(temp=29.0, radius=0.295, height=2.0,
                      temp_unit='degC', radius_unit='um',
                      height_unit='um')
pm = pyotc.PSDMeasurment(exp_setting=es)
for name, data in zip(['psdX', 'psdY', 'psdZ'],
                      [dataX, dataY, dataZ]):
    p = gen_PSD_from_time_series(x=data, fs=102400, N_win=40)
    pm.add_psd(name, p)
```

[23] https://pyotic.readthedocs.io/en/stable/#pyotc-usage

The PSDMeasurement-class provides methods to calculate Stokes drag coefficient and the corrected drag at the given height. For example:

```
pm.get_stokes_drag(unit='nN*s/m')
>> 8.4084459477162419
```

uses the provided microsphere size, medium viscosity (or the temperature to calculate the viscosity of water), to calculate Stokes drag coefficient form Eq. (8.4.10). One can also determine the corrected drag coefficient by:

```
# drag of a sphere close to one plane wall
pm.get_corrected_drag(mode=1, drag_unit='nN*s/m')
>> 9.7706681613066113
# drag of a sphere between two plane walls
pm.get_corrected_drag(mode=2, distance=100,
                      distance_unit='um', drag_unit='nN*s/m')
>> 9.7948688577145369
```

The method `get_corrected_drag(...)` uses either Eqs. (8.4.12) and (8.4.13) (`mode=1`) or Eq. (8.4.21) (`mode=2`) to correct the drag coefficient.

The PSDMeasurement-class can also be used to store information about an active PSD calibration. Here, the excited or driven axis, `ex_axis`, the frequency, `ex_freq`, and the stage amplitude, `ex_amplitude`, and the measured power in the PSD, `ex_power`, must be specified. Optionally, one can also specify the uncertainty of the latter quantities:

```
pm.set_ac_params(ex_axis='psdX', ex_freq=8.0,
                 ex_amplitude=0.139, ex_amplitude_err=0.003,
                 amplitude_unit='nm',
                 ex_power=3.878, ex_power_err=0.162,
                 power_unit='mV**2')
```

After the values for active calibration are set the PSDMeasurement-object also "knows" that it holds information about an active PSD calibration:

```
pm.active_calibration
>> True
```

Furthermore, the PSD data can be stored to files (`pm.save()`) and also load (`pm.load(directory, data_file)`) the PSDMeasurement-object from these files. The files created are, respectively, a TAB-delimited data file and a "parameter"-file in a common config-file format, which holds information about the experimental settings.

9.2.3. Fitting and calibration

Once a PSDMeasurement-object is initialized, a calibration is done via an PSDFit-object, which is initialized by:

```
pf = pyotc.PSDFit(pm)
```

The initialization already uses the PSD-data provided by the PSDMeasurement-object and calculates an analytical solution for the least-squares minimization of a Lorentzian [64, 66].

The analytical solution is typically not accurate for experimental PSDs, because it assumes a Lorentzian-shaped PSD and the PSD data is unweighted. The solution yields the parameters D_V and f_c, which are then taken as initial guess values for the least-squares fit. The initialization can also be done within a given frequency range and without the values at defined frequencies by providing the arguments `bounds` and `f_exclude` (see below).

After initialization, one should choose the fit function according to the Lorentzian-shaped or the hydrodynamically correct PSD (Eqs. (8.4.6) and (8.4.14)) and set up the detection, *i.e.* account for low-pass filtering or aliasing according to Section 8.4.3.

In the example below, a parameterized low-pass filtering is set for the x- and y-axis, *i.e.* the cut-off frequency $f_{3\,\mathrm{dB}}$ and α is setup as parameters for the fitting routine. Furthermore, aliasing of the model function is considered. The fit for the z-axis is setup to use Eq. (8.4.6) without considering any low-pass filtering.

```
# setup hydrod.  correct PSD fit for x and y axis
# with parameterized low-pass filtering
pf.setup_fit(names=['psdX', 'psdY'], model='hydro',
             lp_filter=True, lp_fixed=False,
             f3dB=8000, alpha=0.3,
             aliasing=True, f_sample=102400)
# setup Lorentzian fit for x and y axis
# with parameterized low-pass filtering
pf.setup_fit(names=['z'], model='lorentzian')
```

Once the fit is setup, one can use the `pf.fit_psd()` and `pf.fit_psds()` routine to run the fitting procedure. To fit within a defined range of frequencies—which is done to exclude sources of noise—one can also define the ranges via the argument `bounds` and exclude values at defined frequencies via the argument `f_exclude`.

```
# only fit within these ranges
bounds = {'x': (16, 15e3), 'y': (16, 15e3), 'z': (20, 3e3)}
# exclude PSD values because of cross-talk or electronic noise
f_ex = {'x': [8.0, 44800.0], 'y': [8.0,], 'z': [8.0]}

pf.fit_psds(bounds=bounds, f_exclude=f_ex)
```

The results of the fit can be evaluated by the provided fit-report. This can be switched on via the argument `fitreport=True`. The output would be:

```
----------
  'psdX'
----------
Model: Hydr.  PSD, low-pass filtered and aliased
Flags and parameters:
Low pass filter: True  fixed: False
f_3dB = 8000.0      alpha = 0.300
Radius = 2.950e-07 m   height = 2.000e-06 m    T = 302.149 K
   density = 1050.000
density medium = 995.942 kg/m**3   viscosity = 0.001 Pa*s
De-bias factor = 0.998
```

```
[[Fit Statistics]]
    # function evals   = 33
    # data points      = 1874
    # variables        = 4
    chi-square         = 1879.030
    reduced chi-square = 1.005
    Akaike info crit   = 13.024
    Bayesian info crit = 35.167
[[Variables]]
    D:       14.3835231 +/- 0.070562 (0.49%) (init= 6.401546)
    f_c:     2595.16482 +/- 11.15817 (0.43%) (init= 1186.883)
    f3dB:    6907.05859 +/- 58.55895 (0.85%) (init= 8000)
    alpha:   0.32585626 +/- 0.003487 (1.07%) (init= 0.3)
```

To see if the model function fits the data for a given confidence level well, one can call

```
pf.is_outlier(conf_level=0.95)
>> {'psdXx': False, 'psdY': False, 'psdZ': False}
```

The calibration results can be printed via

```
pf.print_results()
>> ============================================================
   Active calibration results
   ------------------------------------------------------------
   'x'
   ------------------------------------------------------------
   Displacement sensitivity: 9.873e-01 +/- 2.095e-02 nm/mV
   Trap stiffness: 6.891e-02 +/- 2.794e-03 pN/nm
   Drag: 4.526e+00 +/- 1.535e-01 nN*s/m
   ------------------------------------------------------------
   'psdY'
   ------------------------------------------------------------
   Displacement sensitivity: 1.023e+00 +/- 2.509e-02 nm/mV
   Trap stiffness: 6.284e-02 +/- 2.700e-03 pN/nm
   Drag: 4.526e+00 +/- 1.535e-01 nN*s/m
   ------------------------------------------------------------
   'psdZ'
   ------------------------------------------------------------
   Displacement sensitivity: 1.691e+01 +/- 4.749e-01 nm/mV
   Trap stiffness: 1.481e-02 +/- 7.804e-04 pN/nm
   Drag: 4.526e+00 +/- 1.535e-01 nN*s/m
   ============================================================
```

or written to the parameter file associated with the PSDMeasurement by calling `pf.write_results_to_file()`.

Figure 9.1 shows a fit to an experimental PSD (middle), calculated from a time-series signal (top). The position-signal of a trapped polystyrene microsphere with a diameter of 590 nm was recorded for 5.0 s and sampled at 40 kHz. The average PSD was calculated from 40 windows. To use active PSD analysis for calibration, the sample stage was driven with a

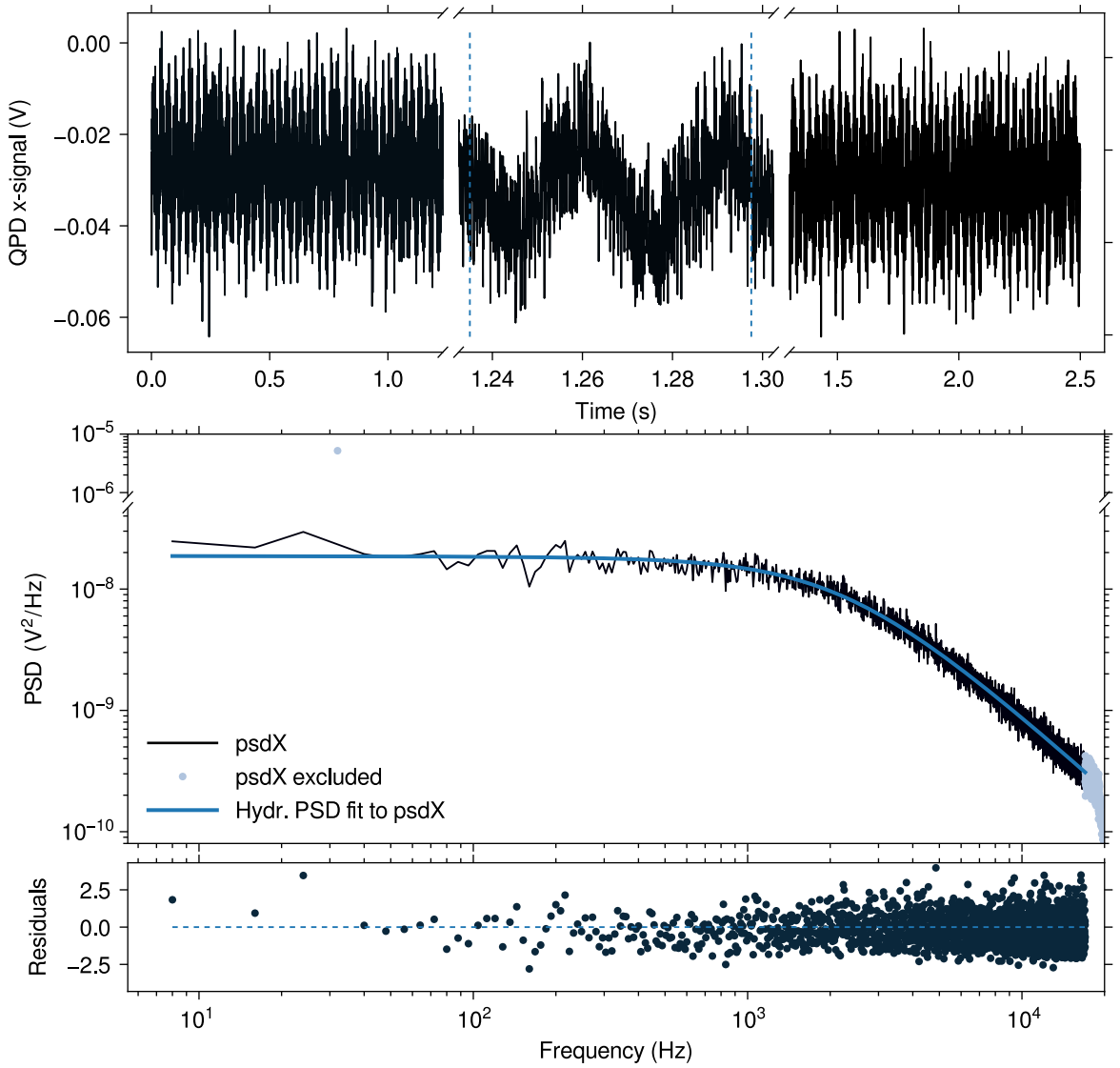

Fig. 9.1 | PSD fit result. The power spectrum (middle) of a position time-trace (top) of a 590 nm polystyrene microsphere, sampled at 40 kHz, is fitted to Eq. (8.4.14). The time trace is separated into 40 windows. To show one of these, the x-axis was broken. The fit was performed qithin the frequency range [8 Hz, 17 kHz] (black data points). The residuals (bottom) are balanced, although low-frequency noise is indicated by the positive residuals at frequencies below 40 Hz.

sine-signal at 32 Hz. The corresponding data point is automatically excluded from the PSD data (circle in Fig. 9.1 (middle)). The data was fitted to the hydrodynamically correct PSD and the height of 2 µm of the microsphere was taken into account. The bottom plot shows the residuals of the fit. The residuals at frequencies below 40 Hz lie above the fit, which can be a sign of low frequency noise, such as pink noise.

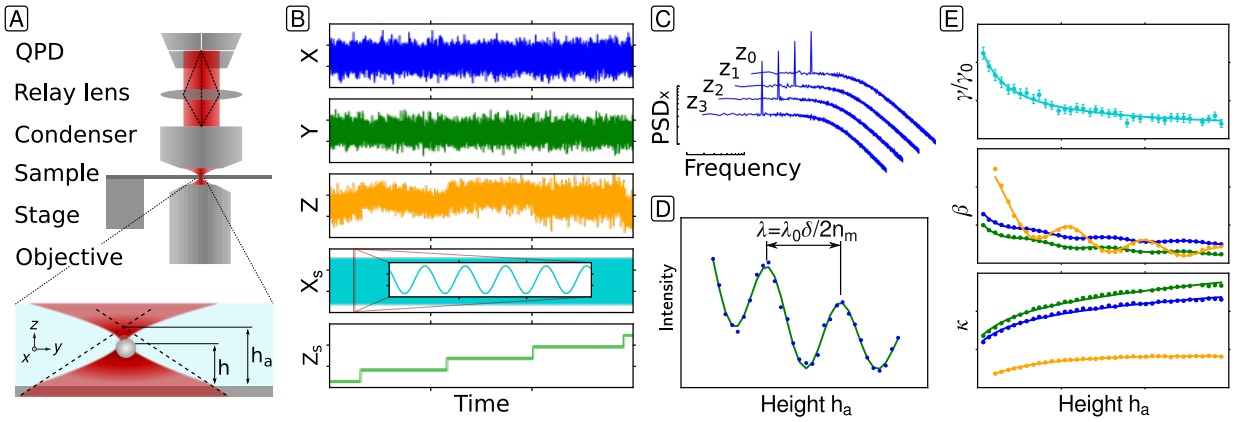

Fig. 9.2 | Height-dependent calibration. (A) Back-focal plane detection design (top) and trapped microsphere (bottom) showing the focal shift resulting in apparent height, h_a, and the true height, h, of the particle above the surface. **(B)** Typical time-series measurement of a height-dependent calibration showing the QPD x-, y-, and z-, and the sine-driven (inset) stage x- and the consecutively changed z-signal. **(C)** PSDs of the QPD x-signal at different stage-heights. **(D)** Sum signal of the QPD vs. stage- (= apparent-) height and a corresponding fit of Eq. (9.2.1) determining the focal shift. **(E)** Results of a height-dependent calibration showing the relative drag, γ/γ_0, determined through Eqs. (8.4.19) and (8.4.24), and the displacement sensitivity, $\beta_{\{x,y,z\}}$, and trap stiffness, $\kappa_{\{x,y,z\}}$, determined via passive PSD analysis and the corresponding global fit (lines) according to Eqs. (8.5.3), (8.5.4) and (8.5.6).

9.2.4. Height-dependent calibration

The HeightCalibration-class manages the PSD measurements and the fitting and evaluation of the height-dependent calibration factors (Eqs. (8.5.1) and (8.5.2)). There are two ways to initialize a HeightCalibration-object. Either PSDMeasurement-objects are generated, the PSD data is loaded from files, as mentioned above, or the object is generated from a set of time-series data associated with different heights (Fig. 9.2A,B). The former method is provided by the HeightCalibration-class:

```
# initialize HC-object
hc = pyotc.HeightCalibration()

# scan directory for PSDMeasurement-files beginning
# with "basename"
hc.get_psd_files('basename', directory=directory);

# generate PSDFit-objects for each height
hc.gen_psd_fits()
```

The time-series method is implemented via the auxiliary class `HeightCalibTime`. The class uses a so-called `motion`-object from the PyOTI package, which holds references to the relevant data in a time-series measurement and detects the steps in the stage z-axis sensor signal. The stage was used to position the trapped microsphere at a given height

(comp. signal z_s in Fig. 9.2B). Once the steps are detected (an example can be found in the example-folder associated with the package) the HeightCalibration-object can be created via

```
# initialize HCT-object from pyoti.motion-object
# and specify the used excitation frequency
hct = pyotc.HeightCalibTime(motion, ex_freq)

# set up experimental conditions (see above)
hct.expset = es

# create HC-object and specify number of averages for PSDs
N_avg = 40
hc = hct.gen_height_calibration(N_avg)
```

Similar to the single PSDFit-object above, the fitting functions need to be setup, *e.g.* via `hc.setup_psd_fits(model='hydro')` and the fitting for all PSDs at all heights is invoked by `hc.fit_psds()`. If the keyword-argument-pair `plot_fits=True` is provided the fit results are also visualized. As discussed above, also the fitting ranges (`bounds`) and frequencies to be ignored (`f_exclude`) can be specified. Each fit and the results can be accessed through `hc.psdfits`. Also, each fit could individually be repeated by calling the method `fit_psds()` with the keyword-arguments `height` or `names`. The results of the fits could be plotted by the method `plot_pc_results()`, which plots the measured drag coefficient and the calibration parameters according to Eqs. (8.4.10), (8.4.19) and (8.4.20).

The data can then be fitted to the height-dependent calibration parameter equations (Eqs. (8.5.3), (8.5.4) and (8.5.6)) by the method `fit_height_data(method={'radius', 'viscosity'})`. When calling the fit-method one needs to specify which of the fit methods, according to Eq. (8.5.6) should be used.

```
hc.ref_ind = 1.326
hc.set_wavelength(1064, unit='nm')
hc.focal_shift = 0.8
hc.fit_height_data(method='radius')
```

Here, the refractive index of water and the used trapping laser wavelength is set. Also the focal shift was set to 0.8. Alternatively, the focal shift can be determined separately (see below). The height-dependent fit uses least-squares fitting to minimize the errors in all datasets. The results can be visualized by calling `plot_results()` (Fig. 9.2E). A successful fit yields the parameters of Eqs. (8.5.1) and (8.5.2), $m_{\beta,\xi}, m_{\kappa,\xi}, \beta_{0,\xi}, \kappa_{0,\xi}$, as well as the actual sample surface height h_0 and the correction factor c_R or c_η, respectively. The results can then be written to a text file for later usage, *e.g.* for calibrating the time-series data investigated with the PyOTI package.

```
hc.write_results_to_file()
```

9.2.5. Determine the focal shift

When trapping is done using oil immersion objectives in a medium with a refractive index that is different from oil, the focal plane is shifted, because of refraction at the sample

surface–medium interface. When trapping in water, the distance between the sample plane and the trap is theoretically reduced by about 80% compared to the distance that a stage has physically moved the sample stage relative to a stationary trap. This focal shift should not be present, if a water immersion objective was used. However, aberrations occur because most objectives are not corrected for the trapping laser wavelength. Practically, the focal shift can differ and should be determined experimentally. PyOTC's HeightCalibration-class also provides a method to measure the focal shift from oscillations in the transmitted intensity of the trapping laser when changing the height of the trap in the sample. The oscillations affect the intensity, which is measured by the QPD-sum signal, and also the displacement sensitivity. Both could be used in principle to determine the focal shift by the method `determine_focal_shift()`:

```
hc.determine_focal_shift(signal=sum-signal,
                         wavelength=1064, ref_index=1.326,
                         report_fs=True, plot_fit=True,
                         wavelength_unit='nm')
```

The method uses the following function to determine the focal shift δ

$$I(h) = I_0 \exp\left[-\frac{(h-h_0)^2}{\tau}\right] \sin\left[\frac{4\pi n_\mathrm{m}}{\lambda_0}\delta(h-h_0)\right] + p_0 + p_1 h + p_2 h^2 + p_3 h^3, \qquad (9.2.1)$$

where n_m is the refractive index of the medium and λ is the trapping laser wavelength. The function is phenomenologically trying to mimick the point-spread-function of the trapping laser (Gaussian) in the z-direction and the polynomial accounts for the intensity gradient along z. Nonetheless, the important fitting parameter is the focal shift, δ which is deduces from the oscillations in the signal (Fig. 9.2D).

10. Conclusion

This chapter gave an overview of the various calibration methods for optical tweezers. Passive and active PSD analysis was recapitulated and the height-dependent calibration was described. The presented theory and calibration procedure was implemented in a python-based calibration software package. The most important features of the software implementation and the typical workflow to calibrate optical tweezers were described.

PyOTC as a part of the joint software PyOTIC, aims to provide a reliable and comprehensible standard to calibrate optical tweezers. Once the software is published and possibly used by a broader user group, it might become an accepted, maintained and further developed calibration software. To this end, there might be the need to develop a graphical user interface to make it even more accessible to other optical tweezers users.

As a side note: Axial active PSD analysis is currently impossible because of a lacking theoretical description of the axial PSD of a sphere near a plane surface. Axially driven microspheres near a plane surface and the resulting resonances in the PSD could possibly be useful to study the validity of the no-slip boundary condition [76], which is a widely used assumption in hydrodynamics. Axial excitation might be useful for such investigations, because the effect of an increasing drag force is more pronounced in the perpendicular case. This might, further, be useful to study these boundary conditions with different combinations of microsphere materials and surface treatments. Axial active PSD analysis is currently not possible, because of the lacking theoretical description of the axial hydrodynamically correct PSD. The missing part is the description of the drag coefficient of an oscillating sphere moving perpendicular to the surface. A road map to develop this theory is to study Stokes' derivation of the drag coefficient for oscillating motion of a sphere [67] and combine it with the theory of Lorentz[70], Faxén [69], and possibly Brenner [71].

Part V.

Interference reflection microscopy

11. Introduction

Optical tweezers combined with various microscopy techniques are a versatile tool for single-molecule force spectroscopy. In surface-based experimental assays, as they are used to study molecular motors, such as kinesins proceeding on microtubules, optical tweezersy are combined with various label-free microscopy contrast methods ranging from bright-field, via differential interference contrast (DIC) [34, 88], or less common, phase-contrast [89] and dark field [90], and Rotating-Coherent-Scattering microscopy (ROCS) [91] to fluorescence including among others epi-, TIRF, confocal, or STED configurations [7, 92–95]. Because fluorescence microscopy requires labeling of proteins, is photo-toxic, and has photobleaching, and brightfield microscopy has low contrast or involves considerable post-processing of the images [96], the technique of choice for visualizing microtubules is often video-enhanced DIC [88, 97]. However, due to the shear axis of the Nomarski prisms, simple DIC implementations are direction-dependent [98] and limit the polarization and power of optical tweezers. Only linearly polarized trapping lasers with the polarization direction aligned with the Nomarski prism's shear axis pass the prims without changing the polarization. Linearly polarized trapping light induces an asymmetry in the force field of the optical trap [99], which may lead to artifacts for 2D and 3D experiments [100, 101], and makes experiments that utilize the transfer of angular momentum of the trapping light to trapped particles difficult [102]. In addition, for near infrared trapping lasers, about 10 % of power is lost per prism. Despite these limitations, DIC is often the technique of choice for microtubule-based optical-tweezers assays.

To circumvent these restrictions the optical tweezers setup was combined with interference reflection microscopy (IRM). IRM provides high, three-dimensional (3D) contrast, can be realized with a simple, cost-efficient optical design, and, in comparison to differential interference contrast (DIC), is orientation independent and does not compromise the polarization state or the power of optical tweezers. Furthermore, since IRM works in reflection, the half-space above the objective is free for other manipulation techniques. IRM was first used by Curtis [103], to measure cell-substrate distances during cell adhesion. These distances were inferred from interference fringes that occur because the back-scattered (or reflected) light of the specimen interferes with the reflected "reference" light from the glass–water interface converting a phase-difference into an amplitude contrast. This contrast changes axially within $\lambda/(4n)$—where λ is the used wavelength for illumination and n is the refractive index of the sample medium—from dark (destructive interference) to light (constructive interference). Morover, the contrast was improved significantly by reducing the amount of unwanted reflected light from other optical elements by crossed polarizers and a so-called "Antiflex" objective (reflection interference contrast microscopy (RICM) [104]). Independent of the implementation, a quantitative analysis of separation distances and optical thicknesses is possible [105] providing 3D information about the sample with exquisite axial precision allowing, for example, ångström precision surface stabilization by tracking immobilized microspheres [106]. Recently, the detection limits of the technique have been pushed further, utilizing

the technical improvements of digital cameras, processing power, and lasers for illumination (interferometric scattering microscopy (iSCAT) [107, 108]) allowing for the detection of single unlabeled molecules sufficiently separated either in space or time [109, 110]. Single microtubules were imaged by IRM in a confocal configuration [111], more recently with high spatiotemporal precision using iSCAT [112], or a solid-state-white-light illumination in an inverted epi-fluorescence microscope [113].

In the following, IRM was used in combination with optical tweezers. By utilizing a high-power LED as a light source, single microtubules could be visualized with a signal-to-noise ratio (SNR) comparable to DIC. To this end, the microtubule contrast was measured and optimized in terms of photon-flux, frame-averaging, and illumination numerical aperture. Furthermore, the 3D profile of an upward bent microtubule was measured, using the optical tweezers and the height-dependent interference patterns. This profile was then used to calibrate the evanescent field of the TIRF microscope. The short coherence length of the LED compared to lasers has the advantage that no speckles and etalon fringes arise, which simplifies image analysis procedures and improves contrast. In general, LED-based IRM is a simple, but powerful microscopy contrast method compatible with many other techniques allowing for high-contrast 3D microscopy. The presented combination can be applied to a wide range of biological systems and allows versatile imaging and force spectroscopy down to single molecules.

12. Materials & methods

12.1. Polymerization of microtubules

Microtubules were polymerized from a 30 µM porcine α/β-tubulin purified according to [114] that contained, 4 mM $MgCl_2$, 1 mM GTP, and 5 % DMSO in BRB80 (80 mM PIPES (1,4-piperazinediethanesulfonic acid, Sigma-Aldrich) pH adjusted to 6.9 using KOH, 1 mM $MgCl_2$, 1 mM EGTA (ethylene glycol-bis(β-aminoethyl ether)-N,N,N',N'-tetraacetic acid , Sigma-Aldrich)). For the fluorescence experiments, 10 % rhodamine-labeled (TAMRA, SE; 5-(and-6)-carboxytetramethylrhodamine, succinimidyl ester (5(6)-TAMRA, SE), Invitrogen, emission peak: 578 nm) tubulin was used. The solution was incubated for 30 min at 37 °C. The polymerized microtubules were then centrifuged and suspended in a 0.1 % taxol–BRB80 solution.

12.2. Microsphere functionalization

Polystyrene (PS) microspheres (diameter = 590 nm, Bangs Laboratories) were functionalized as described in Bugiel *et al.* [115], except the anti-GFP antibody was replaced with a GFP-binding-protein (GBP), which is a 13 kDa GFP binding fragment derived from a llama single chain antibody [116].

A protein solution of a truncated rat kinesin-1 motor protein (his6-rkin430-eGFP) was then mixed with the microsphere solution. The protein solution contained BRB80, 112.5 mM Casein, 1 mM AMPPNP (a non-hydrolyzable analog of ATP), and an oxygen scavenger system (20 mM D-glucose, 20 µg/ml Glucose oxidase, 8 µg/ml, 0.1% β-mercaptoethanol).

12.3. Sample chamber preparation

The sample flow-cells were constructed of Parafilm sandwiched between two cover slips (22 mm × 22 mm, # 1.5, Corning, and 18 mm × 18 mm, # 0, Metzel), which were cleaned and treated with chlorotrimethylsilane vapour under vacuum to generate a hydrophobic surface. The flow chamber was first filled with a solution containing anti-β-tubulin I antibodies (Sigma-Aldrich). During the microtubule bending experiment the concentration of anti-β-tubulin was decreased about 1000×. Non-specific binding was prevented by incubating the flow chamber for 10 min with a 1% solution of pluronic F-127 (Sigma-Aldrich). Afterward, the microtubule solution was flowed in. To bend a microtubule the solution of functionalized microspheres was added after the microtubules bound.

13. Results

13.1. Image processing

13.1.1. Background measurement

Inhomogeneous illumination of the sample is a common problem in microscopy and is accounted for by subtraction of a so-called background image. In IRM, the background strongly depends on the vertical position of the reference plane, *i.e.* the glass–water interface relative to the focal or imaging plane. Therefore, it was necessary to move the reference into the focal plane to measure a background image. To avoid any (static) sample of being considered as background, the sample was laterally moved sufficiently fast while a set of ≈ 400 images at a frame rate of 25 Hz was recorded. A median of this set approximated the static, uneven illumination of the field of view well and was considered as background. This background image was subtracted from the raw IRM images (Fig. 13.1A). After background subtraction, the IRM images showed the interference contrast as a positive or negative signal. Note that the nominal values depend on the bit-depth of the recorded images and should be normalized by this depth if raw signal values need to be compared. All IRM images presented have the background subtracted unless stated otherwise.

13.1.2. Measuring the signal-to-noise ratio

To compare different IRM images it was necessary to use a standard signal-generating sample. Here, the contrast generated by a single isolated microtubule bound to a glass surface was used. One way of measuring a microtubule's signal would certainly be, to use an intensity profile of a line across the microtubule. The difference between the highest and lowest intensity would be the signal. However, this approach is error-prone, because the IRM signal depends on the probe's height above the surface. The latter, in particular, could result in large errors in the signal value.

Here, the signal of a microtubule was extracted from a Gaussian-fit to a median intensity profile calculated along the microtubule-axis. First, a part of a microtubule was cut out, using *Fiji's* segmented-line in combination with the "Straighten" tool [117] (Fig. 13.1B). Then, the median intensity profile along the microtubule-axis was calculated (Fig. 13.1C). The microtubule signal, I_0, was then extracted from a Gaussian-fit ($I(x) = I_0 \exp(-(x - x_0)^2/(2\sigma^2)) + I_{\text{offset}}$) to the median profile. The noise was calculated from a filtered residual image. An image of the IRM signal contains noise, whereby the major intrinsic contribution of noise is shot noise. Other contrast generating content, such as dirt, drift, or fluctuations in illumination intensity add to the total noise. To mainly extract the shot noise, a residual image was calculated by subtracting the Gaussian-fit from every column of a region of interest centered around a microtubule (Fig. 13.1D). A direct calculation of the standard deviation of the intensity distribution of the residual image usually overestimates the perceptual noise

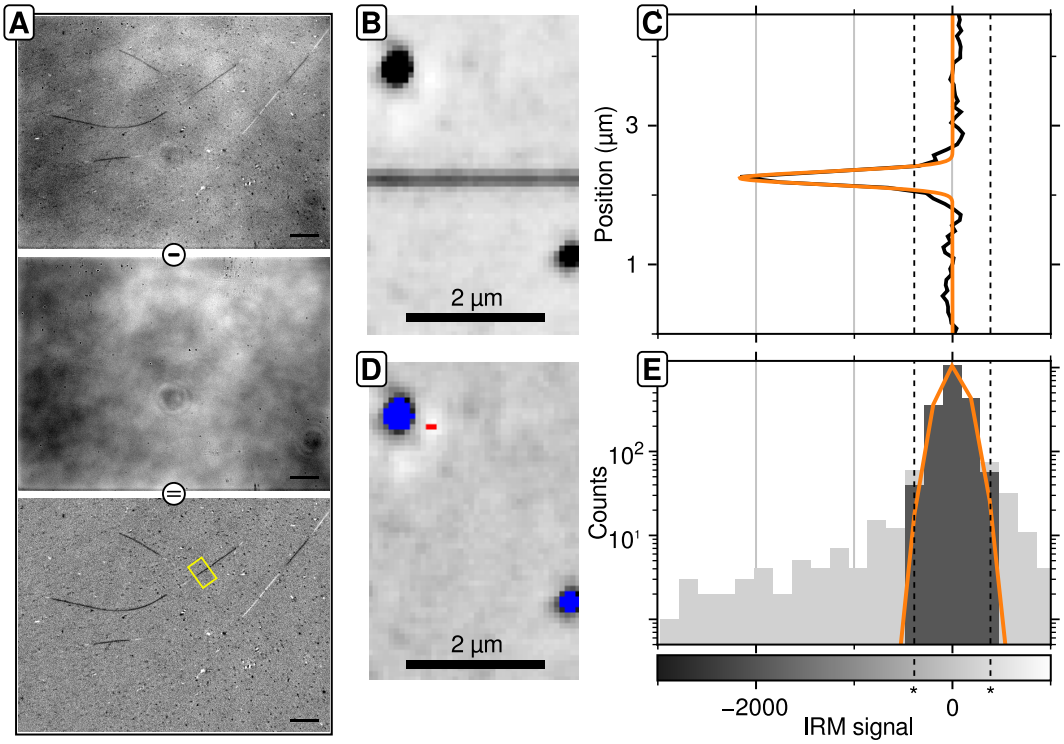

Fig. 13.1 | Background subtraction and SNR measurement of a microtubule. **(A)** Raw (top) and background (middle) IRM image of microtubules on a glass surface. Background subtraction lead to the image of the IRM signal (bottom). **(B)** Region of interest of the microtubule indicated in A. Impurities showed up as black spots. **(C)** Median-intensity profile calculated along the microtubule-axis of B (black) and a Gaussian-fit (orange). **(D)** Residual noise image after subtraction of the Gaussian-fit shown in C from each column of the microtubule-image B. Values that laid above or below the threshold are indicated in red or blue, respectively. **(E)** Histogram of the gray values in D (light gray bars). The image noise was calculated from the gray values within the threshold (dark gray bars) excluding signals from impurities. The threshold (∗) was calculated as ±1.5× the interquartile range around the median gray level.

because dirt or irregularities in the glass surface increase the variance. To minimize the overestimation, a threshold was applied to the noise histogram. The threshold was set at $Q_1 - 1.5\,\mathrm{IQR}$ and $Q_3 + 1.5\,\mathrm{IQR}$, where Q_1 and Q_3 are the first and the third quartile of the intensity distribution and IQR is its interquartile range (Fig. 13.1E). The resulting intensity distribution of the filtered residuals was then fitted to another Gaussian. Its standard deviation was taken as a measure for the noise. The ratio between the signal and the noise was then taken as the measure for the IRM signal quality or SNR.

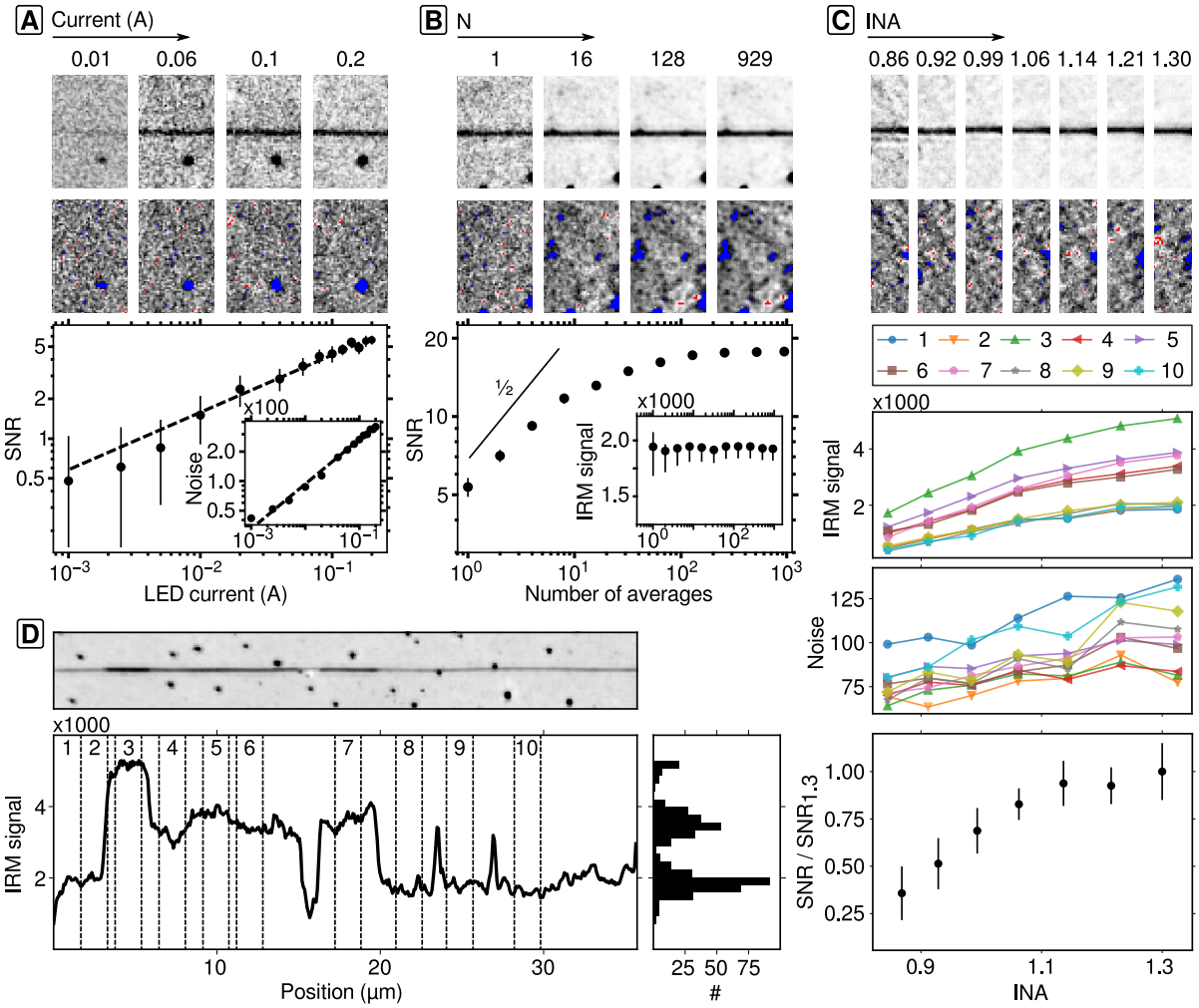

Fig. 13.2 | Optimization of the IRM signal-to-noise ratio. **(A)** Analyzed microtubule images (top) and the image noise (middle) at varying LED currents. The measured SNR is plotted against the applied LED current (bottom). A power-law fit (dashed line) showed near shot-noise limited imaging. Inset: Measured noise vs. LED current. The noise scaled with an exponent 0.46 ± 0.1. **(B)** Analyzed microtubule images (top) and the image noise (middle) for increasing number N of averaged frames. The SNR increases with the number of averaged frames, but reaches a plateau at large N (bottom) as irregularities dominate the noise. The solid line indicates a power-law slope with exponent 0.5. Inset: IRM signal vs. number of averages. The IRM signal of the microtubule was constant with respect to the number of averaged frames. **(C)** Top 2 panels: section 10 images of the microtubule shown in D with increasing INA and the respective image noise. Bottom panels: Legend of sections. Signal of all microtubule-sections (indicated in D) and the corresponding noise is plotted vs. INA. The averaged SNR was normalized by the SNR at INA = 1.3 at the very bottom. **(D)** An averaged image of a microtubule ($N = 50$), its line intensity profile (bottom left) and the corresponding histogram (bottom right). The analyzed microtubule-sections of (C) are indicated (dashed lines).

13.2. Optimizing the signal-to-noise ratio

The SNR of a microtubule increased with the amount of light reaching the camera. To investigate how the signal of a microtubule can be improved, the exposure time was kept constant at 0.04 s and the illumination light was consecutively increased by increasing the LED current until the CCD camera saturated (Fig. 13.2A). The SNR increased in a power-law manner with an exponent 0.44 ± 0.03. This increase approximately follows the theoretical behavior in the shot noise limit with an exponent of 0.5. Deviations may be due to small non-linearities in the LED power–current relationship. In these experiments, the SNR did not saturate. Therefore, the pixel well-depth of our camera was limiting the SNR because higher LED currents saturated the camera. In the shot-noise limit, the SNR improved by averaging consecutive frames.

The SNR of a microtubule increased with the number of averaged frames, but was limited by other contrast-generating irregularities in the sample (Fig. 13.2B). A set of ≈900 images of a single microtubule was recorded at a frame rate of 25 Hz and an LED current of 0.2 A and its SNR as a funtion of the number of averaged frames was measured. In one frame, a single microtubule had a SNR of ≈5.6. Upon averaging, the SNR doubled at $N = 8$ frames (SNR ≈ 11.4), but levelled off to ≈17.2 for $N \geq 128$ frames. The saturation was due to the effective image noise becoming constant because the measured IRM signal of the microtubule was also constant (Fig. 13.2B, bottom, inset). While for a single frame, shot-noise was the dominant noise, the signal of contrast-generating irregularities surpassed the shot-noise for a high number of averages. The increase of the SNR was, therefore, limited by the cleanliness of the sample and the roughness of the glass cover slips. In analogy to the procedure reported for iSCAT imaging [109, 110], the background could possibly be reduced by dynamic background image acquisition and subtraction.

The SNR could be further improved by using a high illumination numerical aperture (INA). By opening and closing the aperture iris, the INA was varied and, thereby, the LED image size in the BFP of the objective. To account for the change in average intensity on the CCD, the LED current was adjusted to a constant mean CCD intensity. One long microtubule was imaged, 50 consecutive frames were averaged, and the signal and the image noise of 10 different microtubule sections was measured (Fig. 13.2C, D). The signal of a microtubule-section and its image noise increased with increasing INA (Fig. 13.2C, middle). The resulting SNR of all microtubule-sections increased up to an INA of 1.14 and levelled off for higher INAs (Fig. 13.2C, bottom). Increasing the illumination angle improved the IRM signal, but also increased the image noise. The increase of the image noise might again have been caused by an increasing visibility of irregularities on the glass surface. However, the increase of the IRM signal was not expected based on theory (comp. Eq. (13.3.1) below). A quantitative comparison of the INA dependence for samples located directly at the glass surface ($h = 0$) or at varying heights did not account well for the increase in the SNR. The measurements might be explained by other effects, *e.g.* by empty-aperture, for which high-order spherical aberrations lead to an effective loss of NA [118]. A non-uniform scattering field of molecules like microtubules, which was recently utilized to improve iScat contrast [119, 120], may have also contributed to the effect even though the imaging NA was unchanged during our experiments.

IRM could distinguish between single and bundled microtubules. Some microtubules (*e.g.* Fig. 13.2D) showed a patchy IRM signal. In IRM, differences in the signal could occur due

to height differences of the specimen or different mass. Changes in height typically occur gradually. Here, the signal changed in a stepwise fashion within the lateral resolution limit. Moreover, the histogram of a line profile along the microtubule in Fig. 13.2D showed a discrete distribution. The discrete peaks suggests that several microtubules were bundled, which is consistent with previous observations [121].

13.3. Quantitative 3D-IRM

To test whether the IRM signal can be used for precise 3D measurements of samples and calibration of the evanescent TIRF field, optical tweezers were used to bend a microtubule upward in a controlled and calibrated fashion (Fig. 13.3A).

To this end, a microsphere that was functionalized to bind microtubules (see Methods Section 12.2) was trapped, attached to a microtubule end, and the microtubule end was pulled upward by displacing the optical trap in 200-nm vertical steps using the deformable mirror (Fig. 4.1). Since the other microtubule end was bound to the glass surface, the microtubule bent with increasing applied force. The increasing vertical position of the microtubule caused a phase change between the reference and scattered field and, therefore, an amplitude change of the IRM signal. To quantify this amplitude change and microtubule deformation, the IRM and TIRF signals were recorded (Fig. 13.3B). Subsequently, the line-intensity profiles along the microtubule were measured and their 3D profiles, $h(x)$ (Fig. 13.3C, E) were determined. The microtubule height, $h(x)$, as a function of lateral position, x, is related to the IRM intensity $I(x)$ according to [105, 122]

$$I(x) = B - D\frac{\sin y}{y}\cos\left(2kh(x)\left[1-\sin^2\left(\frac{\alpha}{2}\right)\right]\right), \tag{13.3.1}$$

where B is the background gray-level intensity, which—after background subtraction—should be close to zero, D is the peak-to-peak interference amplitude, $k = 2\pi n_w/\lambda$ is the wave number with the refractive index of water, n_w, and the illumination wavelength, λ. The parmeter $y = 2kh(x)\sin^2(\alpha/2)$ models the objective's point-spread-function, where $\alpha = \arcsin(INA/n_w)$ is the half angle of the INA cone. The interference amplitude, D, can also be related to the maximum iScat signal by $D = 2srI_{\text{inc}}$, with I_{inc} being the incident intensity, r is the reflectivity given by the refractive index mismatch between the glass–water interface and s is the scattering amplitude [107]. The function $h(x)$ models the microtubule's height with respect to its lateral position x.

The microtubule itself could be modeled as a cantilevered beam of length $L = x_t - x_0$, where $x_t = 0\,\text{nm}$ is the position of the trap and x_0 is the position, at which the microtubule is attached to the surface. The beam equation in the small angle approximation is given by [123]

$$h(x) = A\left(\frac{x_t - x_0}{2}(x-x_0)^2 - \frac{(x-x_0)^3}{6}\right), \tag{13.3.2}$$

where $A = EI/F$ is the shape defining parameter given by the ratio of the flexural rigidity, *i.e.* the product of the elastic modulus E and the geometrical moment of inertia I, and the applied force F, which is provided by the optical trap.

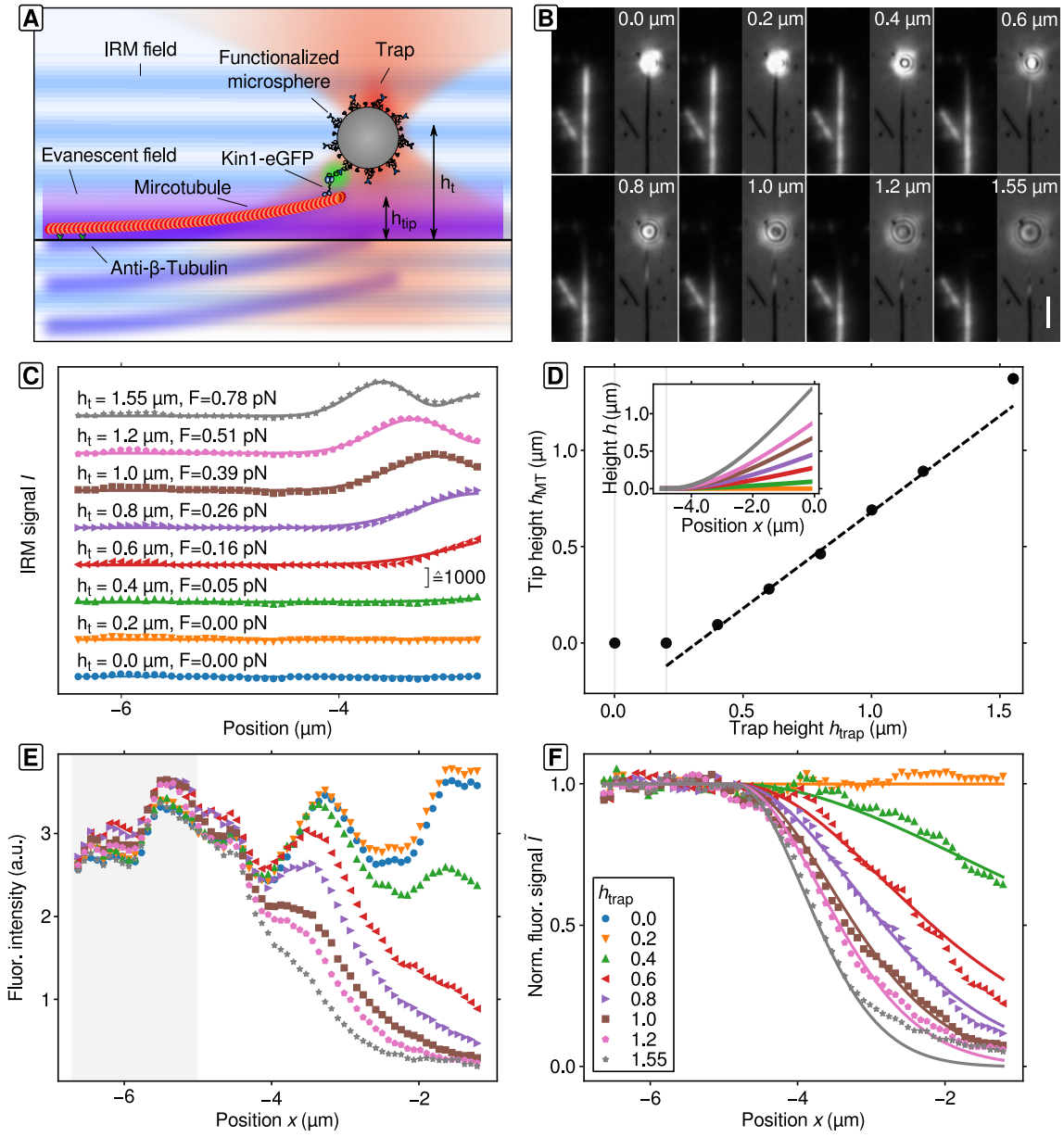

Fig. 13.3 | 3D IRM of bent microtubule. **(A)** Schematic drawing not to scale. A microsphere functionalized with non-motile kinesin-1–GFP motor proteins is trapped and attached to a loose microtubule end, which is pulled upward by the trap. **(B)** TIRF (red channel, left) and IRM images (right) of a bent microtubule and attached microsphere at increasing trap heights. Note that the bright intensity around the microsphere is due to scattering of the illumination light and not due to the trapping laser. The latter is blocked by an infrared filter. Scale bar: 2 µm. **(C)** IRM line profiles along the microtubule shown in B (symbols) and the global fit of Eq. (13.3.1) (solid lines). The trap height and axial force are indicated. For clarity, data points are offset vertically. **(D)** Weighted linear fit (dashed line) to the microtubule tip height h_{MT} (circles) plotted versus the trap height h_{trap} (error bars are SEM, gray lines).

Fig. 13.3. Inset in (D): Calculated microtubule profile vs. height. **(E)** Fluorescence intensity line profiles along the microtubule shown in B for different tip heights. **(F)** Normalized fluorescence intensity line profiles (symbols). Profiles were normalized to the average intensity of the first 20 points and to the line profile at $h_t = 0.0\,\mu m$ (shaded area and blue circles in E, respectively). A global fit (solid lines) of the data to Eq. (13.3.3) determined the depth of the evanescent field.

A global non-linear least-squares fit using Eqs. (13.3.1) and (13.3.2) to the microtubule IRM profiles (Fig. 13.3C) resulted in the height of the microtubule with respect to its lateral position along the microtubule axis. The best fit parameters are listed in Fig. 13.4. Because axial optical tweezers force measurements require significant background correction, which make small-force measurements unreliable in particular for large trap-surface variations [72, 99], the force F that was acting on the microtubule based on its flexural rigidity of $20 \times 10^{-24}\,Nm^2$ [123, 124] was estimated. Equation (13.3.2) allowed to determine the height of the microtubule tip $h_{MT} = h(x_t)$ and the corresponding height-profile of the microtubule (Fig. 13.3D). A linear fit of the microtubule tip height h_{MT} with respect to the height of the trap h_{trap} showed the expected slope of unity and an offset of $(-320 \pm 10)\,nm$. The offset roughly corresponds to the microsphere radius ($\approx$295 nm) plus the linker size ($\approx$35 nm)

Table 13.4 | Bent microtubule fit parameters.

IRM fit		
x_0 (µm)	-4.72 ± 0.02	
D	979 ± 5	
INA	1.15 ± 0.01	
h_t (µm)	A_{h_t} ($\times 10^{-3}\,\mu m^{-2}$)	F (pN)
0.0	0.0 ± 314	0.00 ± 6
0.2	0.0 ± 3347	0.00 ± 66
0.4	2.7 ± 0.4	0.05 ± 0.01
0.6	8.0 ± 0.3	0.16 ± 0.01
0.8	13.2 ± 0.4	0.26 ± 0.01
1.0	19.7 ± 0.6	0.39 ± 0.01
1.2	25.4 ± 0.7	0.51 ± 0.01
1.55	39.0 ± 1.2	0.78 ± 0.02
TIRF fit		
δ (nm)		165 ± 4

Fit parameters of the global fit to the IRM and TIRF intensity profiles. The IRM global fit had $B = 0$, x_0, D, and INA as common parameters for all IRM line profiles and a set of parmeters, A, that corresponded to the force values $F = EI/A$ for each individual line profile. The global fit to all normalized TIRF line profiles had the evanescent field depth δ as common parameter.

[115]. The axial displacement of the microsphere within the trap in the nanometer range was negligible compared to the tip height in the micrometer range (with the maximum force of $F_z \approx 0.8\,\mathrm{pN}$ and a trap stiffness κ_z in the vertical direction of $(0.05 \pm 0.01)\,\mathrm{pN/nm}$, the displacement was $\Delta z = F_z/\kappa_z \approx (16 \pm 4)\,\mathrm{nm}$). The agreement between the IRM-based microtubule tip height and predefined optical trap height confirms that the IRM signal can be used for quantitative 3D measurements.

As a further quantitative control for the accuracy of the IRM-based height profiles, it was tested whether the height profiles were consistent with the exponential decay of the TIRF field. In addition, the profiles could be used to measure the evanescent field depth. The TIRF intensity of the profiles (Fig. 13.3B, E) depend on both the fluorophore labeling density and the fluorophore height above the surface. To account for the inhomogeneous labeling and photo-bleaching, the TIRF intensity profiles were normalized (Fig. 13.3F). The normalized profiles were consistent with an exponentially decreasing TIRF intensity $\tilde{I}$ with increasing distance from the glass–water interface

$$\tilde{I} = \exp(-h(x)/\delta)\,, \tag{13.3.3}$$

where δ is the evanescent field depth. With the known shape of the microtubule, the decay of fluorescence intensity solely depends on the depth of the evanescent field, δ. A global fit of the normalized fluorescence intensity profiles to Eq. (13.3.3) with $h = h(x, x_0, A)$ and the evanescent field depth as common parameter resulted in $\delta = (165 \pm 4)\,\mathrm{nm}$, which is in good agreement with our experimental design. In summary, the microtubule IRM signal quantitatively agreed in 3D with both optical trap and TIRF based height determination.

14. Conclusion

Using LED-based IRM, the 3D profile of a single microtubule could be measured with high contrast and precision. To characterize the quality of the signal, a robust method was developed to measure the SNR of a single microtubule. The presented method accounts for overestimation of the microtubule signal due to contrast generating structures that might lie underneath the microtubule. The method also accounts for overestimation of image noise by avoiding high-contrast signals in the residual image that result from other contrast generating structures.

LED-based IRM was limited by shot noise as the SNR scaled with the available light and was, thus, limited by the electron well-depth of the camera. The SNR of a single microtubule in one frame was about 5.6. This SNR is comparable to the one achieved with DIC (SNR $\approx$ 3.4 [88]). The value is also consistent with recent work using IRM and comparing it to different microscopy techniques [113]. IRM interference fringes gave information about the height of a specimen. Although the quantitative interpretation of the fringes, in general, is a non-trivial task, especially for arbitrary objects [122], in cases where the structure of interest is simple, such as a bent microtubule, it is possible to determine the axial position of an object and thus, the 3D profile with high precision on the order of a few tens of nanometers. This knowledge was used to determine the depth of the evanescent field of the TIRF microscope, thus, providing another method to characterize its excitation field [125].

LED-based IRM is a cheap and simple, high-contrast 3D microscopy method, which can be integrated easily into existing optical setups providing a viable alternative to commonly used microscopy techniques. IRM does not require expensive nor complicated optical elements like lasers or polarizing optics. Especially for single-molecule force spectroscopy using optical tweezers, IRM has considerable advantages compared to DIC microscopy. First, there is no trapping power loss (DIC prisms may reduce the trapping power by up to 10%). Second, whereas the SNR of a microtubule is comparable to the one achieved in DIC [88], IRM outcompetes DIC with its simple optical design, cheap components and its orientation-independent contrast. Third, in contrast to DIC, IRM does not restrict the optical tweezers design to a linearly polarized trapping laser. Therefore, any polarization state like circularly polarized light is possible allowing the use of an optical microprotractor, torsion balance, or torque wrench [102, 126]. Also, because illumination and detection is done via the objective lens, the sample is freely accessible from the top for other manipulation or imaging techniques. Furthermore, if a sufficiently stable power supply and heat sink are used, LED-based illumination provides long-term intensity stability. Moreover, the short coherence length of about 10 µm of an LED[24]prevents etalon fringes, *i.e.* "unwanted" interference effects as they can occur with laser-based techniques, such as iScat and, therefore, allows a larger field of view for imaging. In iScat microscopy, these interference effects can only be circumvented by differential imaging. Here static contrast in an image is continuously subtracted, so only

dynamic changes in contrast are visualized.

LED-based IRM can potentially be improved, in the future. First, one could try to increase the photon flux to increase the signal of a specimen. This could be achieved by the use of a camera with a higher full-well capacity to allow imaging with higher LED intensities. Second, higher frame rates would allow to increase the number of averaged frames, while keeping the effective frame rate constant and, therefore, could improve the contrast by reducing the shot noise.

The detection limit of the presented LED-based IRM is about 5 MDa. To estimate the detection limit of LED-based IRM, one could consider the following: A single microtubule yielded a SNR of about 5 for a single frame of $\approx$ 40 ms exposure time. This signal was generated by a number of tubulin monomers within one diffraction limited spot. Considering the mass of one tubulin monomer, $m_{\mathrm{Tub}} = 50\,\mathrm{kDa}$ and an average density of proteins of $\rho_{\mathrm{prot}} = 1.35 \cdot 10^3\,\mathrm{kg\,m^{-3}}$ [128], the diameter of a monomer is $d_{\mathtt{tub}} \approx 5\,\mathrm{nm}$. The size of the diffraction limited spot of the IRM is $d_{\mathrm{PSF}} = 2 \times 0.61\lambda/NA \approx 400\,\mathrm{nm}$. Assuming a number of 13 protofilaments composing a microtubule, there are about $N_{tub} = 13 \times d_{\mathrm{PSF}}/d_{\mathrm{tub}} \approx 1000$ tubulin monomers within a diffraction limited spot. These correspond to a mass of 50 MDa. By averaging 100 frames the SNR of a microtubule increased to $SNR_{\mathrm{MT},100} = 17$. Extrapolation result in a lower detection limit of $50\,\mathrm{MDa} \times SNR_{\mathrm{min}}/SNR_{\mathrm{MT},100} = 15\,\mathrm{MDa}$, with a minimal SNR of $SNR_{\mathrm{min}} = 5$. In the current stage, the LED was operated at about 200 mA, but could be operated at 2 A. This could push the limit futher by a factor of $\sqrt{10} \approx 3$, which yielded 5 MDa. Thus, the combination of using a higher photon flux and better camera could improve the overall contrast and push the detection limit or the temporal resolution of the microscopy technique further. The latter is especially important to image and track transient processes, such as the movement of microspheres with size below 200 nm. Furthermore, the implementation of dynamic background subtraction could decrease the detection limit, because static sources of noise would not compromise the SNR and, therefore, higher number of averages could be used. Here, the contrast would only be limited by drift.

[24] The coherence length can be calculated by [127]

$$\Delta l_c = \frac{\bar{\lambda}^2}{\Delta\lambda}.$$

It depends on the diode's mean wavelength, $\bar{\lambda} = 450\,\mathrm{nm}$ and the spread of its spectrum, the so called linewidth, $\Delta\lambda = 20\,\mathrm{nm}$.

Part VI.

Closure

15. Conclusion and outlook

Scientific instruments are often one of the basic requisites to interrogate particular fields in science. Optical tweezers opened up a new order of magnitude in terms of force- and displacement-sensitivity with high temporal resolution. Optical traps give "hands" to the experimenter who was formerly condemned to only passively observe without being able to actively manipulate the sample [129]. This statement is especially true when pursuing questions that address the molecular level of scientific interest, such as the interaction of single (bio-)molecules. Moreover, optical tweezers could also be used to probe fundamental concepts in physics [73, 74].

The improvement of optical tweezers in terms of stability pushes the limits, of what is commonly referred to as high-resolution measurements. The combination of optical tweezers with different microscopy techniques widens the field of potential applications, because visualization of a specific specimen or their interaction is facilitated. In this sense, the combination of stable optical tweezers with two-color fluorescence microscopy is a milestone for single-molecule research. One is now capable to precisely position a single molecule, such as DNA, which is bound to a microsphere, using the optical tweezers and localize, on the one hand, the binding of associated labeled molecules. Furthermore, if the binding partner was labeled as well, one can get insights in the interaction kinetics, structure, *etc.* by Förster resonance energy transfer (FRET) [130].

Combining microscopy techniques and optical tweezers usually leads to restrictions in the optical design, which also limits the variety of experiments. For surface-based microtubule assays, the microscopy technique of choice, to date, is DIC microscopy. The achievable contrast, for even diffraction limited samples, such as microtubules, outweighed the restrictions in the optical design of optical tweezers. In DIC microscopy, the Nomarski or Wollaston prisms restrict the polarization to linearly polarized trapping laser light. This restriction leads to an asymmetric optical trap, which may lead to artifacts and makes experiments, where the transfer of angular momentum is utilized, difficult [102].

Custom-built and commercial optical tweezers setups have ambivalent qualities. Custom-build optical tweezers setups can be changed and tweaked to adapt the device to new experimental needs or add and develop new features. They also provide the user with the opportunity to investigate the impact of various parameters to a particular measurement. In contrast to commercially available setups, custom-built ones often lack an easy-to-use user interface. This is because the hardware abstraction is usually low. Furthermore, because custom-built setups have an direct hardware access to the experimenter, malfunction of parts of the instrument are more probable due to the complexity of interconnections between the sub-devices. Commercial instruments are designed for a defined set of experiments, which allows a cost-optimized, maintenance-friendly, and compact design. Because the hardware is fixed, their hardware abstraction is usually high, thus, easy-to-use user interfaces and sophisticated features can be developed. Currently, optical tweezers are commercially available from a few companies: JPK Instruments (Germany), Lumicks (Netherlands), Alahram

(Egypt), Thorlabs, *etc.* However, none of the available instruments provides requisites for high-precision surface-based assays, yet.

The presented design of an optical tweezers setup aimed to provide the means for surface-based single-molecule assays. Its combination with a state-of-the-art, objective-based TIRF microscope allows to visualize fluorescent probes in the vicinity of the sample chamber surface with a high SNR. Furthermore, the combination with LED-based IRM removes the design restrictions of DIC. Moreover, IRM provides high contrast in three dimensions, can be realized with a simple and cost-efficient design, frees the half-space above the objective and complies with the design principles of stable optical tweezers as the method does not involve high heat production at the setup. The presented combination with optical tweezers can be applied to a wide range of biological systems and allows versatile imaging and force spectroscopy. LED-based IRM could potentially be further improved in terms of time-resolution or contrast. Utilizing a faster camera or one with a higher pixel well depth allows to use higher illumination intensities that should further increase the achievable SNR, which may make the visualization of single proteins possible. The design principle of the presented setup will possibly influence the design of future setups and might ease the additional combination with other state-of-the-art microscopy techniques, such as super-resolution microscopy via, for example, STED microscopy.

The shown stability of the optical tweezers is sufficient to measure microsphere-displacements with ångström precision. The achieved temperature stability, by operating the setup in a separate chamber and additional active temperature control of the objective achieves focal plane stabilities for all three axes below the ångström level. This stability is needed in surface-based assays, where a high trap stiffnesses can be achieved. Measurements were likely limited by the stability of the piezo-translation stage. A stiffer stage with a faster response time may provide higher spatial precision.

The measurement of forces and displacements in the vicinity of the sample chamber surface relies on a robust and precise calibration procedure. A height-dependent calibration by active PSD analysis can satisfy these requirements. It provides height-dependent calibration factors and allows for determination of the true height of the microsphere. Yet, its implementation is tedious when done with common data analysis software. Its programmatic implementation can be cumbersome, especially when a reasonable operational freedom is desired. Furthermore, considerable testing of the source code is required to eliminate errors. A freely accessible and transparent solution is provided by the Python Optical Tweezers Calibration package, PyOTC. Because the package is made from free and open source software (FOSS), anybody can use it. This reduces costs for licenses and makes the analysis of optical tweezers data more transparent. To date, PyOTC is a framework solution, which is intended to be used within Jupyter Notebooks and can easily be integrated into (Python) scripts for analysis. Additional features like a comparison to the equipartition theorem or Boltzmann-statistics can be added. Another approach that is currently not implemented is the calibration based on auto-correlations. However, such routines can be implemented with ease using established python packages, such as the `scipy.signal` package. In the future, the package could be the basis for an easy-to-use software solution with a graphical user interface, which would make it even more accessible to a broader range of users.

Contributions

Gero Hermsdorf contributed in the computer aided design of optomechanical parts of the instrument. He also implemented a first version of the TIRF microscope during his Diploma thesis work, which was supervised by the author. Sebastian Rösch helped with the implemetation of the temperature sensors during his Bachelor thesis work, which was supervised by the author. Alexandro Grecco performed the piezo-mirror response measurements and performed the Aligna® laser stabilization measurements during his focus practical module, which was supervised by the author.

Publications

- **LED-based interference-reflection microscopy combined with optical tweezers for quantitative three-dimensional single microtubule imaging**
  Steve Simmert, Mohammad Kazem Abdosamadi, Gero Hermsdorf, Erik Schäffer
  Opt. Express 26, 14499-14513 (2018)

- **Label-free high-speed wide-field imaging of single microtubules using interference reflection microscopy**
  Mohammed Mahamdeh*, Steve Simmert*, Anna Luchniak, Erik Schaeffer, Jonathon Howard
  accepted in J. Microsc. (2018), (BioRxiv: https://doi.org/10.1101/273086)

- **PyOTIC – Effective investigation and calibration of highly time-resolved optical tweezers data**
  Steve Simmert*, Tobias Jachowski*, Erik Schäffer
  in preparation

* Equal contribution by authors

List of Figures and Tables

Abbreviations and notations

$\langle\cdot\rangle$	average
$\lfloor\cdot\rfloor$	floor function, *i.e.* round to nearest lower integer
PyOTC	Python Optical Tweezers Calibration package
PyOTIC	Python Optical Tweezers Investigator and Calibration software
vs.	versus
ADEV	Allan deviation
AVAR	Allan variance
BFP	back focal plane
BFPI	back focal plane interferometry
comp.	compare
DIC	differential interference contrast
EM	electromagnetic
FFP	front focal plane
HWP	half-wave plate
IRM	interference reflection microscopy
LED	light emitting diode
NI	National Instruments
PSD	power spectral density
QPD	Quadrant photo diode
QWP	quarter-wave plate
SDM	standard deviation of the mean
SEM	standard error of the mean

STED	stimulated emission depletion
TIR	total internal reflection
TIRF	total internal reflection fluorescence
var	variance
VI	LabVIEW virtual instrument

Bibliography

1. Kepler, J. *De cometis libelli tres* (Apergeri, Andreæ, 1619).
2. Maxwell, J. C. *A Treatise on Electricity and Magnetism* (Cambridge University Press, 1873).
3. Bartoli, A. Il calorico raggiante e il secondo principio di termodynamica. *Nuovo Cimento* **15,** 196–202 (1884).
4. Lebedev, P. N. Untersuchungen über die Druckkräfte des Lichtes. *Ann. Phys.* **6,** 433–458 (1901).
5. Van de Hulst, H. C. *Light scattering by small particles* (Dover Publications, 1981).
6. Ashkin, A. Acceleration and trapping of particles by radiation pressure. *Phys. Rev. Lett.* **24,** 156–159 (1970).
7. Ashkin, A., Dziedzic, J. M., Bjorkholm, J. E. & Chu, S. Observation of a single-beam gradient force optical trap for dielectric particles. *Opt. Lett.* **11,** 288 (1986).
8. MacDonald, M. P., Spalding, G. C. & Dholakia, K. Microfluidic sorting in an optical lattice. *Nature* **426,** 421–424 (2003).
9. Chen, K. *et al.* Directed transport and location-designated rotation of nanowires using ac electric fields. *Microfluid. Nanofluidics* **16,** 237–246 (2014).
10. Pauzauskie, P. J., Jamshidi, A., Valley, J. K. & Satcher, J. H. Parallel trapping of multiwalled carbon nanotubes with optoelectronic tweezers. *Appl. Phys. Lett.* **95,** 2–4 (2009).
11. Ashkin, A. & Dziedzic, J. Optical trapping and manipulation of viruses and bacteria. *Science* **235,** 1517–1520 (1987).
12. Tadir, Y. *et al.* Micromanipulation of sperm by a laser generated optical trap. *Fertil. Steril.* **52,** 870–873 (1989).
13. Ashkin, A. Forces of a single-beam gradient laser trap on a dielectric sphere in the ray optics regime. *Biophys. J.* **61,** 569–582 (1992).
14. Moffitt, J. R., Chemla, Y. R., Smith, S. B. & Bustamante, C. Recent Advances in Optical Tweezers. *Annu. Rev. Biochem.* **77,** 205–228 (2008).
15. Jannasch, A. *Coated particles as enhanced probes for optical tweezers* Diplomathesis (Technische Universität Dresden, 2008).
16. Neuman, K. C. & Block, S. M. Optical trapping. *Rev. Sci. Instrum.* **75,** 2787–809 (2004).
17. Chaumet, P. C. & Nieto-Vesperinas, M. Time averaged total force on a dipolar sphere in an electromagnetic field. *Opt. Lett.* **25,** 1065–1067 (2003).

18. Nieminen, T. A. *et al.* Optical tweezers computational toolbox. *J. Opt. A* **9** (2007).
19. Waterman, P. The T-matrix revisited. *J. Opt. Soc. Am. A. Opt. Image Sci. Vis.* **24,** 2257–2267 (2007).
20. Mahamdeh, M. *High Resolution Optical Tweezers Optimized for Biological Studies* PhD thesis (Technische Universität Dresden, 2011), 104.
21. Hobbs, P. C. D. *Building Electro-optical systems* 1st ed. (ed Goodman, J. W.) (Wiley-Interscience, 2000).
22. Vanderwerf, D. F. *Applied prismatic and reflective optics* 303 (SPIE Press, Bellingham,Washington, 2010).
23. Huang, Y. *et al.* Three-axis rapid steering of optically propelled micro/nanoparticles. *Rev. Sci. Instrum.* **80,** 1–8 (2009).
24. Smith, W. *Modern optical engineering: The Design of Optical Systems* 4th ed. (ed Soda, T.) (McGraw Hill, 2008).
25. Nikon. *Microscope Objectives for Bioscience* 2016.
26. Gittes, F. & Schmidt, C. F. Interference model for back-focal-plane displacement detection in optical tweezers. *Opt. Lett.* **23,** 7–9 (1998).
27. Pralle, A., Prummer, M., Florin, E.-L., Stelzer, E. & Hörber, J. Three-dimensional high-resolution particle tracking for optical tweezers by forward scattered light. *Microsc. Res. Tech.* **44,** 378–386 (1999).
28. Hermsdorf, G. *Total internal reflection fluorescence combined with optical tweezers to study membrane mechanics* Diploma thesis (Technische Universität Dresden, 2013), 45.
29. *Handbook of biological confocal microscopy* 3rd ed. (ed Pawley, J. B.) (Springer, Boston, MA, 2006).
30. Jiang, C., Kaul, N., Campbell, J. & Meyhofer, E. A novel dual-color bifocal imaging system for single-molecule studies. *Rev. Sci. Instrum.* **88,** 053705 (2017).
31. National Instruments. *NI Dynamic signal acquisition user manual* 2010.
32. Edelstein, A., Amodaj, N., Hoover, K., Vale, R. & Stuurman, N. Computer control of microscopes using µManager. *Curr. Protoc. Mol. Biol.* 1–17 (2010).
33. Zwillinger, D. *CRC Standard Mathematical Tables and Formulae* 31st ed. (Chapman and Hall, 2003).
34. Mahamdeh, M. & Schäffer, E. Optical tweezers with millikelvin precision of temperature-controlled objectives and base-pair resolution. *Opt. Express* **17,** 17190–17199 (2009).
35. Rösch, S. *Application of a temperature feedback in optical tweezers.* Bachelor thesis. Oct. 2014.
36. Deutscher Kalibrierdienst. *DKD-R 5-6 Richtlinie Bestimmung von Thermometerkennlinien Ausgabe* Deutscher Kallibrierdienst, 2008.
37. Ziegler, J. G. & Nichols, N. B. Optimum settings for automatic controllers. *Trans. ASME,* 759–768 (1942).

38. IEEE Standards Coordinating Committee 27 on Time and Frequency. *IEEE Standard Definitions of Physical Quantities for Fundamental Frequency and Time Metrology - Random Instabilities* 2009.
39. Accurion. *Compendium, Priciples of Halcyonics Active Vibration Isolation Technology* tech. rep. (Accurion, 2017).
40. Platus, David L. (Minus K Technology, I. *Negative-stiffness-mechanism vibration isolation systems* tech. rep. (Minus K Technology, Inc., Inglewood, CA, 1999).
41. Hermsdorf, G., Szilagyi, S. A. & Schäffer, E. High performance, passive, low cost steel spring vibration isolation system. *unpublished,* 1–4 (2018).
42. Czerwinski, F., Richardson, A. C. & Oddershede, L. B. Quantifying Noise in Optical Tweezers by Allan Variance. *Opt. Express* **17,** 13255 (2009).
43. Joint Committee For Guides In Metrology. *Vocabulaire international de métrologie* **3,** 104 (2012).
44. Rose, A. *Vision: human and electronic* (ed Wolfe, W. L.) 203 (Plenum Press, 1973).
45. Joint Committee For Guides In Metrology. *Evaluation of measurement data — Guide to the expression of uncertainty in measurement* **September,** 134 (2008).
46. Gibson, G. M., Leach, J., Keen, S., Wright, A. J. & Padgett, M. J. Measuring the accuracy of particle position and force in optical tweezers using high-speed video microscopy. *Opt. Express* **16,** 14561–14570 (2008).
47. Lansdorp, B. M. & Saleh, O. A. Erratum: Power spectrum and Allan variance methods for calibrating single-molecule video-tracking instruments. *Rev. Sci. Instrum.* **83,** 2011–2012 (2012).
48. Lansdorp, B. M. & Saleh, O. A. Power spectrum and Allan variance methods for calibrating single-molecule video-tracking instruments. *Rev. Sci. Instrum.* **83** (2012).
49. Mahamdeh, M., Campos, C. P. & Schäffer, E. Under-filling trapping objectives optimizes the use of the available laser power in optical tweezers. *Opt. Express* **19,** 11759–11768 (2011).
50. The TableStable, L. *Vibration analyser VA-2C* 2017. <http://www.tablestable.com/uploads/ckeditor/VA-2/Manual%20VA-2%20C.pdf>.
51. Smith, D. A. A quantitative method for the detection of edges in noisy time-series. *Philos. Trans. R. Soc. Lond. B.* **353,** 1969–1981 (1998).
52. Simmert, S., Jachowski, T. & Schäffer, E. Python framework to efficiently analyze and calibrate optical tweezers data. *unpublished* (2018).
53. Chung, S. H. & Kennedy, R. A. Forward-backward non-linear filtering technique for extracting small biological signals from noise. *J. Neurosci. Methods* **40,** 71–86 (1991).
54. Smith, S. B., Cui, Y. & Bustamante, C. Optical-trap force transducer that operates by direct measurement of light momentum. *Method. Enzymol.* **361,** 134–162 (2003).
55. Farré, A. & Montes-Usategui, M. A force detection technique for single-beam optical traps based on direct measurement of light momentum changes. *Opt. Express* **18,** 11955–11968 (2010).

56. Farré, A., Marsà, F. & Montes-usategui, M. Optimized back-focal-plane interferometry directly measures forces of optically trapped particles. *Opt. Express* **20,** 12270 (2012).

57. Thalhammer, G., Obmascher, L. & Ritsch-Marte, M. Direct measurement of axial optical forces. *Opt. Express* **23,** 6112–29 (2015).

58. Mas, J. *et al.* Measuring stall forces in vivo with optical tweezers through light momentum changes. *Proc. SPIE* **8097,** 809726–809726–10 (2011).

59. Otto, O. *et al.* Real-time particle tracking at 10,000 fps using optical fiber illumination. *Opt. Express* **18,** 22722 (2010).

60. Felgner, H., Müller, O. & Schliwa, M. Calibration of light forces in optical tweezers. *Appl. Opt.* **34,** 977–982 (1995).

61. Prieve, D., Bike, S. & Frej, N. Brownian motion of a single microscopic sphere in a colloidal force field. *Faraday Discuss. Chem. Soc.* 209–222 (1990).

62. Florin, E.-L., Pralle, a., Stelzer, E. & Hörber, J. Photonic force microscope calibration by thermal noise analysis. *Appl. Phys. A* **66,** S75–S78 (1998).

63. Ghislain, L. P. & Webb, W. W. Scanning-force microscope based on an optical trap. *Opt. Lett.* **18,** 1678–1680 (1993).

64. Berg-Sørensen, K. & Flyvbjerg, H. Power spectrum analysis for optical tweezers. *Rev. Sci. Instrum.* **75,** 594 (2004).

65. Tolić-Nørrelykke, S. F. *et al.* Calibration of optical tweezers with positional detection in the back focal plane. *Rev. Sci. Instrum.* **77,** 103101 (2006).

66. Nørrelykke, S. F. & Flyvbjerg, H. Power spectrum analysis with least-squares fitting: Amplitude bias and its elimination, with application to optical tweezers and atomic force microscope cantilevers. *Rev. Sci. Instrum.* **81,** 075103 (2010).

67. G. Stokes, G. On the Effect of Internal Friction of Fluids on the Motion of Pendulums. *Trans. Cambridge Philos. Soc.* **9.** Reprinted in Mathematical and Physical Papers, Sir George Gabriel Stokes and Sir J. Larmor, Vol. 3, 1880–1905, 8–106 (Nov. 1850).

68. Berg-Sørensen, K. & Flyvbjerg, H. The colour of thermal noise in classical Brownian motion: A feasibility study of direct experimental observation. *New Journal of Physics* **7** (2005).

69. Faxén, H. *Einwirkung der Gefässwände auf den Widerstand gegen die Bewegung einer kleinen Kugel in einer zähen Flüssigkeit* PhD thesis (1921).

70. Lorentz, H. A. *Abhandlungen über Theoretische Physik* (Teubner, B. G., Leipzig, 1907).

71. Brenner, H. The slow motion of a sphere through a viscous fluid towards a plane surface. *Chem. Eng. Sci.* **16,** 242–251 (1961).

72. Schäffer, E., Nørrelykke, S. F. & Howard, J. Surface forces and drag coefficients of microspheres near a plane surface measured with optical tweezers. *Langmuir* **23,** 3654–3665 (2007).

73. Jannasch, A., Mahamdeh, M. & Schäffer, E. Inertial effects of a small brownian particle cause a colored power spectral density of thermal noise. *Phys. Rev. Lett.* **107,** 1–5 (2011).

74. Franosch, T. *et al.* Resonances arising from hydrodynamic memory in Brownian motion. *Nature* **478,** 85–88 (2011).

75. Felderhof, B. U. Spectrum of position fluctuations of a Brownian particle bound in a harmonic trap near a plane wall. *J. Chem. Phys.* **136,** 134–136 (2012).

76. Felderhof, B. U. Hydrodynamic force on a particle oscillating in a viscous fluid near a wall with dynamic partial-slip boundary condition. *Phys. Rev. E* **85,** 1–7 (2012).

77. Berg-Sørensen, K., Peterman, E. J. G., Weber, T., Schmidt, C. F. & Flyvbjerg, H. Power spectrum analysis for optical tweezers. II: Laser wavelength dependence of parasitic filtering, and how to achieve high bandwidth. *Rev. Sci. Instrum.* **77,** 063106 (2006).

78. Montange, R. K., Bull, M. S., Shanblatt, E. R. & Perkins, T. T. Optimizing bead size reduces errors in force measurements in optical traps. *Optics Express* **21,** 39–48 (Jan. 2013).

79. Dufresne, E. R., Altman, D. & Grier, D. G. Brownian dynamics of a sphere between parallel walls. *Europhys. Lett.* **53,** 264–270 (2001).

80. Lobry, L. & Ostrowsky, N. Diffusion of Brownian particles trapped between two walls: Theory and dynamic-light-scattering measurements. *Phys. Rev. B* **53,** 12050–12056 (1996).

81. Vermeulen, K. C., Wuite, G. J. L., Stienen, G. J. M. & Schmidt, C. F. Optical trap stiffness in the presence and absence of spherical aberrations. *Appl. Opt.* **45,** 1812–1819 (2006).

82. Neuman, K. C., Abbondanzieri, E. A. & Block, S. M. Measurement of the effective focal shift in an optical trap. *Opt. Lett.* **30,** 1318 (June 2005).

83. Tolić-Nørrelykke, I. M., Berg-Sørensen, K. & Flyvbjerg, H. MatLab program for precision calibration of optical tweezers. *Comput. Phys. Commun.* **159,** 225–240 (2004).

84. Hansen, P. M., Tolić-Nørrelykke, I. M., Flyvbjerg, H. & Berg-Sørensen, K. tweezercalib 2.0: Faster version of MatLab package for precise calibration of optical tweezers. *Comput. Phys. Commun.* **174,** 518–520 (2006).

85. Hansen, P. M., Tolic-Nørrelykke, I. M., Flyvbjerg, H. & Berg-Sørensen, K. tweezercalib 2.1: Faster version of MatLab package for precise calibration of optical tweezers. *Comput. Phys. Commun.* **175,** 572–573 (2006).

86. Osterman, N. TweezPal – Optical tweezers analysis and calibration software. *Comput. Phys. Commun.* **181,** 1911–1916 (2010).

87. Welch, P. The use of fast Fourier transform for the estimation of power spectra: A method based on time averaging over short, modified periodograms. *IEEE Trans. Audio Electroacoust.* **15,** 70–73 (June 1967).

88. Bormuth, V., Howard, J. & Schäffer, E. LED illumination for video-enhanced DIC imaging of single microtubules. *Journal of Microscopy* **226,** 1–5 (2007).

89. Kong, L., Zhang, P., Setlow, P. & Li, Y.-q. Characterization of Bacterial Spore Germination Using Integrated Phase Contrast Microscopy, Raman Spectroscopy, and Optical Tweezers. *Anal. Chem.* **82,** 3840–3847 (2010).

90. Fedosov, I. Particle image velocimetry for visualizing laser-induced motion of nanoparticles. *SPIE Newsroom,* 8–10 (2007).

91. Koch, M. D. & Rohrbach, A. Label-free Imaging and Bending Analysis of Microtubules by ROCS Microscopy and Optical Trapping. *Biophysical Journal* **114,** 168–177 (2018).

92. Lang, M. J., Fordyce, P. M. & Block, S. M. Combined optical trapping and single-molecule fluorescence. *J. Biol.* **2,** 6 (2003).

93. Comstock, M. J., Ha, T. & Chemla, Y. R. Ultrahigh-resolution optical trap with single-fluorophore sensitivity. *Nat. Methods* **8,** 335–340 (2011).

94. Visscher, K., Brakenhoff, G. J. & Krol, J. J. Micromanipulation by "multiple" optical traps created by a single fast scanning trap integrated with the bilateral confocal scanning laser microscope. *Cytometry* **14,** 105–114 (1993).

95. Heller, I. *et al.* STED nanoscopy combined with optical tweezers reveals protein dynamics on densely covered DNA. *Nat. Methods* **10,** 910–916 (2013).

96. Gutiérrez-Medina, B. & Block, S. M. Visualizing individual microtubules by bright field microscopy. *Am. J. Phys.* **78,** 1152 (2010).

97. Walker, R. A. *et al.* Dynamic instability of individual microtubules analyzed by video light microscopy: rate constants and transition frequencies. *J. Cell Biol.* **107,** 1437–1448 (1988).

98. Shribak, M. & Inoué, S. Orientation-independent differential interference contrast microscopy. *Appl. Opt.* **45,** 460–469 (2006).

99. Bormuth, V. *et al.* Optical trapping of coated microspheres. *Opt. Express* **16,** 13831–13844 (2008).

100. Bugiel, M., Jannasch, A. & Schäffer, E. Implementation and Tuning of an Optical Tweezers Force-Clamp Feedback System. *Methods Mol. Biol.* **1486,** 109–136 (2017).

101. Bugiel, M., Mitra, A., Girardo, S., Diez, S. & Schäffer, E. Measuring Microtubule Supertwist and Defects by Three-Dimensional-Force-Clamp Tracking of Single Kinesin-1 Motors. *Nano Lett.* **18,** 1290–1295 (2018).

102. Ramaiya, A., Roy, B., Bugiel, M. & Schäffer, E. Kinesin rotates unidirectionally and generates torque while walking on microtubules. *Proc. Natl. Acad. Sci. U. S. A.* **114,** 10894–10899 (2017).

103. Curtis, A. S. G. A Study by Interference Reflection Microscopy. *J. Cell Biol.* **20,** 199–215 (1964).

104. Ploem, J. S. in *Mononuclear Phagocytes In Immunity Infection Pathology* (ed Van Furth, R.) 405–421 (Blackwell Scientific, London, 1975).

105. Rädler, J. & Sackmann, E. Imaging optical thicknesses and separation distances of phospholipid vesicles at solid surfaces. *J. Phys. II* **3,** 727–748 (1993).

106. Kim, K. & Saleh, O. a. Stabilizing method for reflection interference contrast microscopy. *Appl. Opt.* **47,** 2070–2075 (2008).

107. Jacobsen, V., Stoller, P., Brunner, C., Vogel, V. & Sandoghdar, V. Interferometric optical detection and tracking of very small gold nanoparticles at a water-glass interface. *Opt. Express* **14,** 405–14 (2006).

108. Ortega-Arroyo, J. & Kukura, P. Interferometric scattering microscopy (iSCAT): new frontiers in ultrafast and ultrasensitive optical microscopy. *Phys. Chem. Chem. Phys.* **14,** 15625 (2012).

109. Ortega Arroyo, J. *et al.* Label-free, all-optical detection, imaging, and tracking of a single protein. *Nano Lett.* **14,** 2065–2070 (2014).

110. Piliarik, M. & Sandoghdar, V. Direct optical sensing of single unlabelled proteins and super-resolution imaging of their binding sites. *Nat. Commun.* **5,** 1–8 (2014).

111. Amos, L. & Amos, W. The bending of sliding microtubules imaged by confocal light microscopy and negative stain electron microscopy. *J. Cell Sci. Suppl.* **14,** 95–101 (1991).

112. Andrecka, J., Ortega Arroyo, J., Lewis, K., Cross, R. A. & Kukura, P. Label-free Imaging of Microtubules with Sub-nm Precision Using Interferometric Scattering Microscopy. *Biophys. J.* **110,** 214–217 (Jan. 2016).

113. Mahamdeh, M., Simmert, S., Luchniak, A., Schaeffer, E. & Howard, J. Label-free high-speed wide-field imaging of single microtubules using interference reflection microscopy. *bioRxiv.* doi:10.1101/273086. <https://www.biorxiv.org/content/early/2018/03/06/273086> (Mar. 2018).

114. Castoldi, M. & Popov, A. V. Purification of brain tubulin through two cycles of polymerization–depolymerization in a high-molarity buffer. *Protein Expression and Purification* **32,** 83–88 (2003).

115. Bugiel, M. *et al.* Versatile microsphere attachment of GFP-labeled proteins with preserved functionality Microsphere preparation. *J. Biol. Methods* **2,** 1–12 (2015).

116. Rothbauer, U. *et al.* A Versatile Nanotrap for Biochemical and Functional Studies with Fluorescent Fusion Proteins. *Mol. Cell. Proteomics,* 282–289 (2008).

117. Schindelin, J. *et al.* Fiji: an open-source platform for biological-image analysis. *Nat. Methods* **9,** 676–682 (2012).

118. Juškaitis, R. in *Handb. Biol. Confocal Microsc.* (ed Pawley, J. B.) 239–250 (Springer US, Boston, MA, 2006).

119. Lee, K. *et al.* A planar dielectric antenna for directional single-photon emission and near-unity collection efficiency. *Nat. Photonics* **5** (2011).

120. Liebel, M., Hugall, J. T. & van Hulst, N. F. Ultrasensitive label-free nanosensing and high-speed tracking of single proteins. *Nano Letters,* 1277–1281 (2017).

121. Oldenbourg, R., Salmon, E. & Tran, P. Birefringence of Single and Bundled Microtubules. *Biophys. J.* **74,** 645–654 (1998).

122. Limozin, L. & Sengupta, K. Quantitative Reflection Interference Contrast Microscopy (RICM) in Soft Matter and Cell Adhesion. *ChemPhysChem* **10,** 2752–2768 (2009).

123. Howard, J. *Mechanics of Motor Proteins and the Cytoskeleton* (Sinauer Associates, Inc, 2001).

124. Gittes, F., Mickey, B., Nettleton, J. & Howard, J. Flexural rigidity of microtubules and actin filaments measured from thermal fluctuations in shape. *J. Cell Biol.* **120,** 923–934 (1993).

125. Gell, C., Berndt, M., Enderlein, J. & Diez, S. TIRF microscopy evanescent field calibration using tilted fluorescent microtubules. *Journal of Microscopy* **234,** 38–46 (2009).

126. La Porta, A. & Wang, M. D. Optical torque wrench: Angular trapping, rotation, and torque detection of quartz microparticles. *Phys. Rev. Lett.* **92,** 9–12 (2004).

127. Hecht, E. *Optics* 4th Editio (ed Black, A.) (Addison Wesley, 2002).

128. Fischer, H., Polikarpov, I. & Craievich, A. F. Average protein density is a molecular-weight-dependent function. *Protein Sci* **13,** 2825–2828 (Oct. 2004).

129. Ha, T. Probing Nature's Nanomachines One Molecule at a Time. *Biophysical Journal* **110,** 1004–1007 (Mar. 2016).

130. Mameren, J. v., Wuite, G. J. & Heller, I. in *Methods in Molecular Biology - Single Molecule Analysis* (ed Peterman, E. J. G.) 3–23 (Springer, 2018).

Acknowledgments

A great deal of this work was achieved with the support and help of other people that shall be mentioned here.

Thank you, Erik, for giving me the chance to pursue this project and for the freedom during the years to work on various topics. Thank you for your patience an time when answering and discussing my questions. I appreciate your enthusiasm, detailed questioning and perfectionism. Thank you for your supervision and being a fair boss!

Thank you, Tobi, for your support, commitment and time to help and discuss problems with respect to Linux-, Python- and LabVIEW-programming. It was a great experience to develop software in a (small) team with you. I highly appreciate our discussions about science, politics and the future. You were one of the anchor points that helped to ultimately finish this project. I thank you for pointing me to Hagen Rether. Thank you, Gero, for your contributions to design, construct and assemble Gleipnir. I appreciate and admire your down-to-earth way of looking at things. Thanks as well for sharing the love for hot Indian food. Thank you, Kazem, for your help with the microtubule bending assay! I appreciate the scientific and non-scientific discussions with you. Diving into various subjects was always fun! I didn't know that there's so much to know about sand! Thanks, Avin, for the good food, your lateral thinking, your philosophical sidetracks regarding life and science. Thanks so much for the invitation to India. It was awesome and an honor to attend your wedding! Thanks, Suman, for the awesome food! I will always remember who loves to eat eggs more than I do. Thanks, Tine and Mayank, for the discussions, the biological input, the feedback and the laughs we had. Micha, thank you for your help in the lab and sharing of knowledge and wine. Thanks, Anita, for your help in with the single-molecule Kip3-stepping assay. Maria, thank you for the wolves!

I further thank Mohammed Mohammdeh, for sharing his knowledge and aspects of building stable optical tweezers and for his consideration in the comparative IRM study; Ty for comments on the IRM paper; Valentina for the gooood sicilian cusine, Mehrbod, for his help tackling the molecular biophysics seminars and Swathi, Elisa, Maya, Moritz and Kevin it was fun having youse around!

This work would not have been possible without the constant support of Miriam, my wife. Danke für deine Unterstützung, deine Liebe und deinen Antrieb.

Für den Zuspruch und Interesse an meiner Arbeit danke ich Mario, Oli, Fabian, Manuel und Sven[†].

Software

A major fraction of this thesis was created by the use of free and open source software. The following (incomplete) list of software and tools were very useful and their developers shall be acknowledged! Debian Linux, Inkscape, LaTeX, Emacs, Fiji, Git, SVN, Python, Jupyter, numpy, scipy, matplotlib, lmfit.

Sodann fällt es [...] doch für die gemachten Pläne zu kurz aus; da deren Ausführung immer sehr viel mehr Zeit erfordert, als angenommen war: ferner sind solche, wie alle menschlichen Dinge, dem Mißlingen, den Hindernissen so vielfach ausgesetzt, daß sie sehr selten zum Ziele gebracht werden. Endlich, wenn zuletzt auch alles erreicht wird, so waren die Umwandlungen, welche die Zeit an uns selbst hevorbringt, außer Acht und Rechnung gelassen; also nicht bedacht worden, daß weder zum Leisten, noch zum Genießen, unsere Fähigkeiten das ganze Leben hindurch vorhalten. Daher kommt es, daß wir oft auf Dinge hinarbeiten, welche, wenn endlich erlangt, uns nicht mehr angemessen sind; wie auch, daß wir mit den Vorarbeiten zu einem Werke die Jahre hinbringen, welche derweilen unvermerkt uns die Kräfte zur Ausführung desselben rauben. So geschieht es denn oft, daß der mit so langer Mühe und vieler Gefahr erworbene Reichtum uns nicht mehr genießbar ist [...]

— Arthur Schopenhauer
Aphorismen zur Lebensweisheit